UiT
THE ARCTIC UNIVERSITY OF NORWAY

FACULTY OF SCIENCE AND TECHNOLOGY

Department of Geology

The nature of the gas-hydrate/free gas transition zone at the base of the hydrate-stability zone from high-resolution 3D seismic data

—

Kirsti Bjørnøy

EOM-3901 Master thesis in Energy, Climate and Environment

January 2015

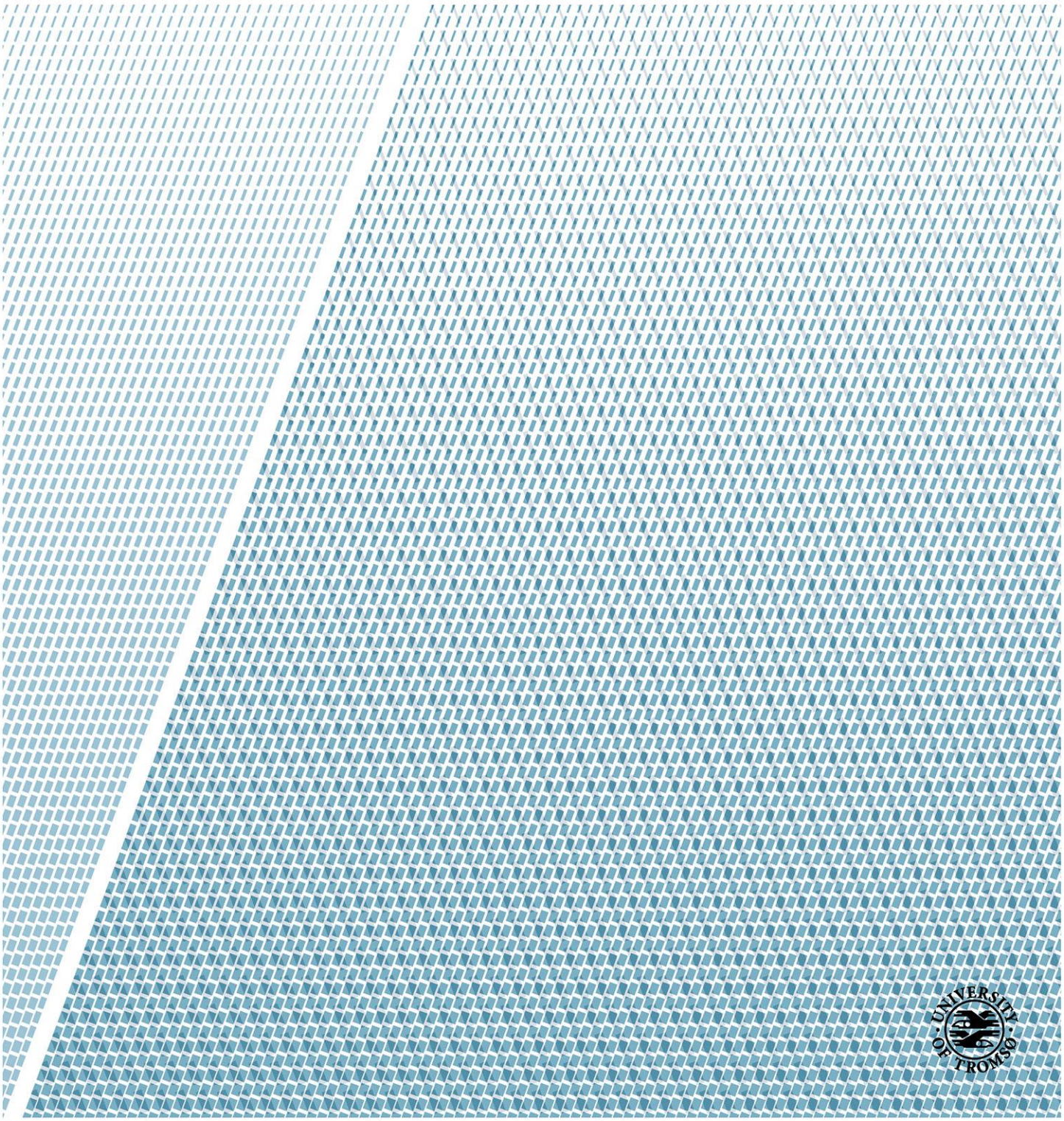

Abstract

Geophysical evidence of a prominent BSR at Vestnesa Ridge and north to the northern flank of the Storegga slide escarpment infer that gas hydrates are ubiquitous within these regions. A wide range of fluid flow structures have previously been discovered from these regions, as well as gas seepage activity from pockmarks on the eastern segment of Vestnesa Ridge.

This paper focuses on high-resolution 3D seismic interpretation and attribute analysis of amplitude anomalies in relation to the BSR and underlying free gas zone (FGZ), as well as BSR characteristics in relation to fluid flow structures. The study is carried out for three high-resolution 3D seismic datasets, two from Vestnesa Ridge and one located north to the northern flank of the Storegga Slide area on the mid-Norwegian margin.

Pull-up and push-down effects of the BSR are frequently associated with chimney structures and are interpreted to reflect the occurrence of gas hydrate and free gas, respectively. However, these features are most likely a combination of several factors i.e. deformational processes, warm fluids ascending from larger depths. The extent and distribution of these effects and features show remarkable differences when comparing each dataset.

As the BSR is formed by the termination of individual gas-charged horizons, the alternating high and low amplitude values are interpreted to result from varying free gas saturations trapped in beds of alternating sediment properties. As each investigated horizon show highest amplitude values against the BSR boundary, it is suggested to be partly affected by interference from thin gas-charged beds that pinch out against the GHSZ. Conspicuously lateral amplitude patterns observed along enhanced reflections are as well addressed to constructive and destructive interference between layers of varying gas saturations. The seismic characterization of the FGZ below the BGHSZ suggest that gas migration and accumulation are morphologically controlled by the anticlinal shape of the Vestnesa Ridge. The more complex FGZ geometry at the slope setting north to the northern flank of the Storegga Slide area, suggests that gas migration and accumulation are restricted to preferable strata and controlled by local geology.

Acknowledgements

Nå er jeg klar for å levere masteren. Endelig er dagen her. Endelig.

Men først vil jeg takke dere som har hjulpet meg på veien. Takk til min veileder Stefan Bünz. Det var noen startproblemer og programmer som ikke lot seg gjennomføre. Det er allerede glemt. Samtidig vil jeg vil takke Stefan Bünz og Karin Andreassen for at jeg i sommer fikk muligheten til å delta på forsknings-cruise med R/V Helmer Hanssen. Det var en veldig lærerik og spennende erfaring.

Viktigst av alt, det har vært folkene rundt meg alle disse årene. Energi og Miljø-klassen, folkene på brakka. Spesielt latterkulene med EOM-jentene gjennom alle disse årene. Marianne og Tina, Hong Kong var en fantastisk tid!

Til mine morsomme venner utenfor studiet. Takk for deres tålmodighet og oppmuntrende ord når dagene (så altfor mange) har vært lange på universitetet. Takk til familien min, som alltid er støttende og får humøret mitt på rett kjør. Jeg setter så stor pris på dere!

Sist, men ikke minst. Jørgen. Parallelt med masteren ble vi eiere av et hus, og total-renovering av kjelleren ble ditt masterprosjekt. Uten deg, din støtte og motiverende ord hadde aldri kabalen gått opp. Nå står vi med en ferdig master og en leilighet snart klar for utleie. Håndlangeren din er offisielt tilbake. Tusen takk, kjære.

Kirsti Bjørnøy, Januar 2015

Table of contents

1. Introduction

1.1 Objective

The primary objective of this thesis is to identify and map the base of the hydrate-stability zone (BHSZ) boundary separating hydrate-bearing sediments from gas-charged sediments beneath. A bottom-simulating reflection (BSR) on seismic data marks the base of the hydrate-stability zone (HSZ) in continental margin sediments worldwide. It results from a strong impedance contrast between hydrate-bearing high-velocity and gas-charged low-velocity sediments. The study is carried out on three high-resolution 3D seismic datasets, two from Vestnesa Ridge and one located north of the northern flank of the Storegga Slide area on the mid-Norwegian margin. 3D seismic data with high bandwidth and advanced geophysical interpretation allow a much more detailed investigation of the transition zone from gas hydrates to free gas in continental margin sediments. The thesis will investigate amplitude anomalies in relation to the BSR and the underlying free gas zone (FGZ) as well as closely-spaced lateral variations in the depth of the BHSZ particularly around vertical fluid flow structures. This could lead to a better understanding of gas-trapping mechanisms and the passage of gas through the hydrate-stability zone without the formation of hydrates.

1.2 Structure and outline

To fulfill the described objectives, the paper is structured into 6 chapters:

1. Introduction: Apart from presenting the objectives and structure of the project paper, a scope of the increasing interest in gas hydrate as a resource as well as a potential hazard will be introduced. A short introduction to the study areas are as well presented here.
2. Fundamental theory: Fundamental theory concerning gas hydrates and nature of the bottom-simulating reflector at the base of the hydrate stability zone.
3. Data and methods: An overview of the data and applied methods used in the paper are described here.
4. Results: The seismic observations and modelling results are presented here.
5. Discussion: The observations described in chapter 4 are discussed here.
6. Conclusion: Presents concluding remarks based on results and the discussion chapter.

1.3 Significance of gas hydrates

The increasing interest and importance of gas hydrates arise from a variety of reasons. Gas hydrates are seen as a potential energy resource, as well as recognized for their possible role in global climate change (Kvenvolden, 1993[a]). Gas hydrates are also seen as a hazard to seafloor stability and offshore drilling - and production operations. During the last decades there has been accomplished extensive research to the above mentioned topics with the aim of a greater understanding.

1.3.1 Gas hydrate as a future energy resource

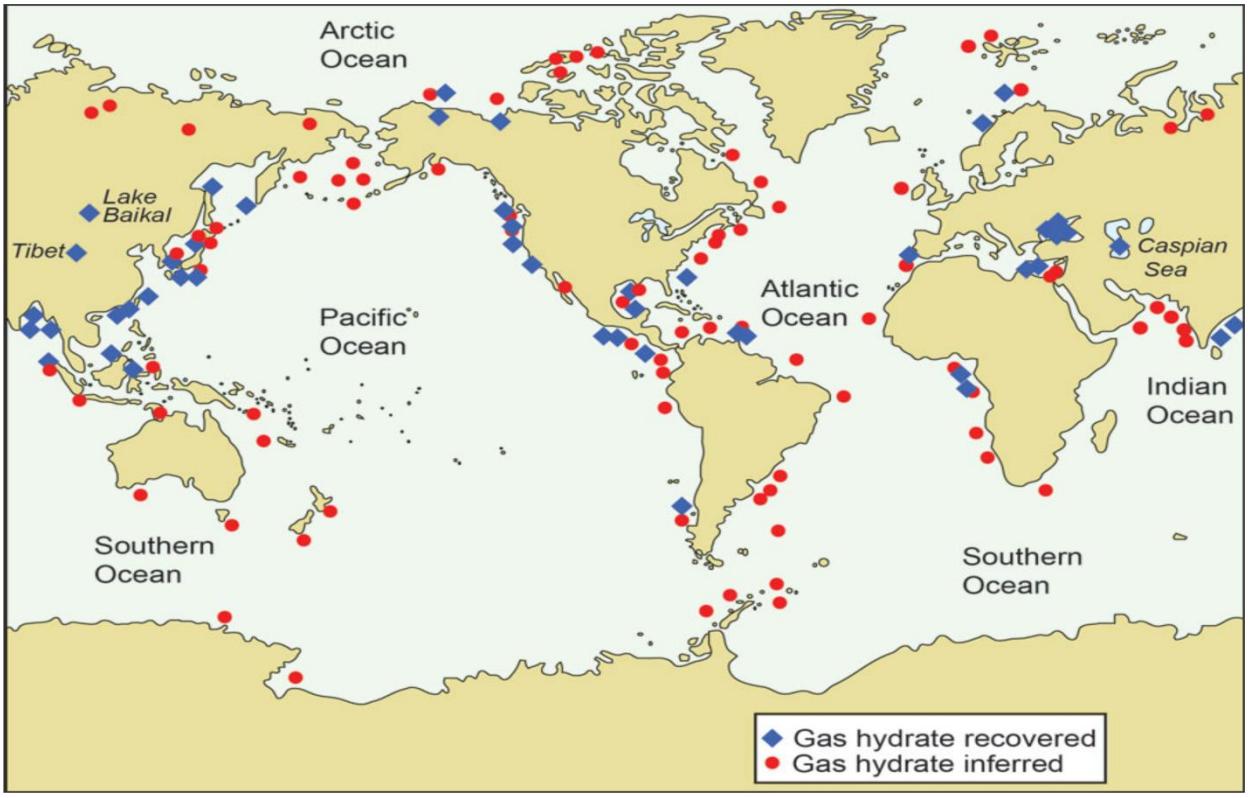

Figure 1-1: Map showing the global distribution of discovered gas-hydrate deposits. Blue diamonds show areas where gas hydrates have been recovered. Red dots represent areas where gas hydrates are inferred from geophysical data (From Ruppel and Noserale, 2012)

In order to meet future energy demands, gas hydrates may serve as an unconvential energy source. Natural gas, hereby methane, is preferential as a fossil fuel source for several reasons. In comparison to oil and coal, natural gas produces significantly less carbon dioxide (CO_2), making it the cleanest fossil fuel (Grozic, 2010). Gas hydrate as a potential energy source is especially attractive due to its vast amount of hydrate methane located at shallow sediment depths, as well as its wide geographical distribution (Kvenvolden, 1999).

Natural gas hydrates occur worldwide in the upper 2000 m of sediments both onshore and offshore in permafrost regions, as well as in deep oceanic settings on outer continental margins (Kvenvolden, 1998, 1999). Figure 1-1 shows the occurrence of known and inferred gas hydrates worldwide, where 97% of natural gas hydrates are located offshore and 3 % onshore. The global distribution makes it accessible to many countries, and may especially be beneficial for nations with an immediate energy demand. Countries that do not exhibit large conventional hydrocarbon resources or alternative energy resources, the energy potential from production of gas from gas hydrate deposits could be of great importance (Kvenvolden, 2000; Collett, 2002; Makogon, 2010). Nations such as India and Japan that traditionally rely heavily on energy imports have implemented large assets into hydrate research and the production from gas hydrate deposits (Collett, 2002). Potential gas hydrate exploitation in their jurisdictional waters could significantly change the global trade picture (Grozic,2010).

During the last three decades several estimates of the global amount of methane in hydrates have been attempted. Milkov (2004) presented a thorough review of the global hydrate estimates and their methodologies. It revealed a trend where the total estimates of hydrated gas have decreased with the increasing knowledge of concentration and distribution of gas hydrates. With the current knowledge about gas hydrates, the estimated hydrate-bound gas reserves both onshore and offshore are over 1.5 $x10^{16}$ m^3. Even if only 17-20% of these resources are produced, it can provide sufficient supply of energy for 200 years (Makogon, 2010). Apparently high uncertainty lies within estimates of the amount of gas hydrates, but even with the lowered estimates over the past decade they still represent significant amounts (Maslin *et al.,* 2010).

However, how to commercially exploit gas hydrate remains an unresolved topic. To gain an economically and safe production from gas hydrate deposits, technical challenges must be overcome and depend heavily on future research. Detection of viable concentrations of gas hydrate requires advanced seismic methods to establish the in-place resources and to estimate the technical recoverability (Collett, 2002; Makogon, 2010). Collett (2002) proposed that the evolution of gas hydrates as a viable energy resource of natural gas will develop much in the same way as for other unconventional energy resources (shale gas, deep gas, tight sands and coal bed methane).

1.3.1 Methane as a greenhouse gas

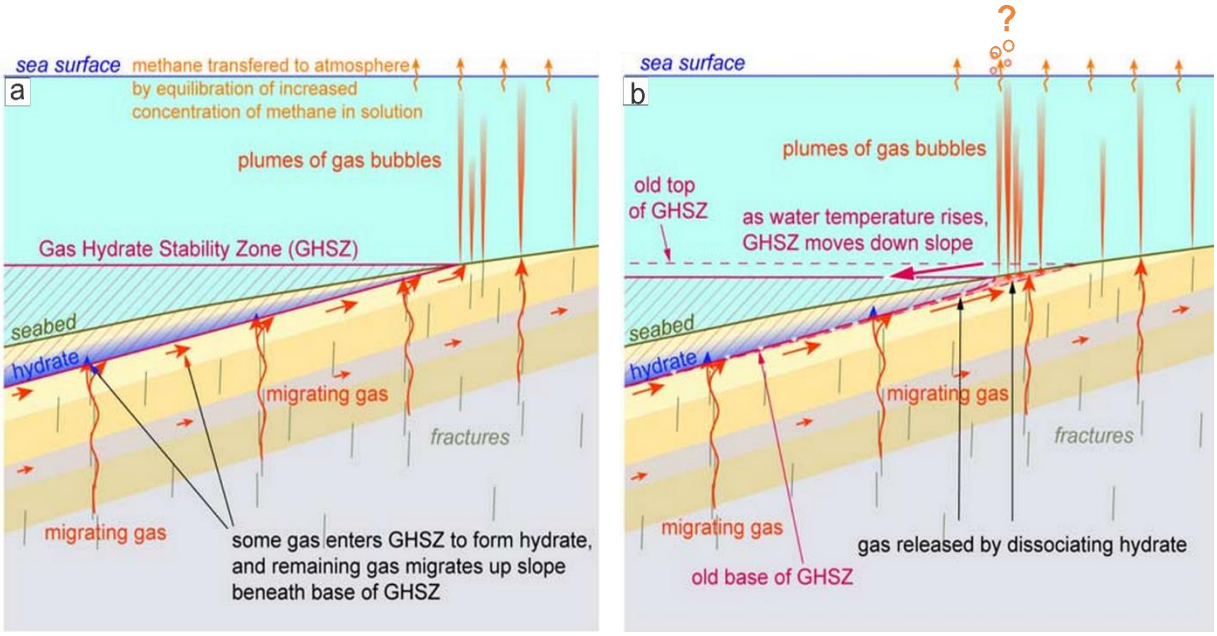

Figure 1-2: (a) Entering the gas hydrate stability zone (GHSZ), the migrating methane gas may form hydrate and consequently reduce the overall permeability at the base of the GHSZ. Resultantly, this may re-route the remaining gas to migrate up slope. Methane gas that escape from the seabed beyond the GHSZ rises as bubbles through the seawater. Most of the methane appears to dissolve in the water. Some dissolved methane will enter the atmosphere by equilibration (b) Rise of ocean temperatures may prompt the GHSZ to contract down slope and cause gas released by dissociating hydrates. Where the GHSZ is removed entirely, all the released gas is free to move to the seabed, guided by local variation in lithology and structure (From Westbrook *et al.*, 2009).

Gas hydrates are also of interest due to their potential role in climate change. Global warming will elevate ocean temperatures and cause a sea-level rise due to melting of polar ice caps and glacial ice. A change in sea level may alter the temperature and pressure regime in oceans and consequently affect the stability of gas hydrates (figure 1-2). As a consequence gas hydrate may depressurize, dissociate into water and methane is further released to the atmosphere. If methane reaches the atmosphere it has a global warming potential 20 times larger than the equivalent weight of carbon dioxide (CO_2) when integrated over 100 years (Kvenvolden, 1993[a], 1999). Hence, a significant flux of methane from oceans and into the atmosphere could further intensify the greenhouse effect.

Documented peaks in the record of atmospheric methane concentration has been argued to result from warming at the end of the last ice age which may have led to destabilization of gas hydrate and release of methane (Nisbet, 1990; Kennett *et al.*, 2003; Maslin *et al.*, 2004). Moreover, the discussion continues of whether current and future global warming may cause similar processes leading to a significant increase in atmospheric methane (Maslin *et al.*, 2010). Kvenvolden (1999, 2000) suggested that for notable amounts of methane to reach the atmosphere it must overcome several obstacles.

The factors limiting the transfer of methane would be the rate of hydrate dissociation, gas migration, trapping in sediments, and amount of gas venting into the water column. He also pointed out that much of the released methane from dissociation of gas hydrate would probably oxidize to carbon dioxide, then dissolve in water and consequently not reach the atmosphere as active methane gas.

Methane stored in gas hydrate deposits in ocean sediments exhibit estimates ranging from 500-10 000 GtC. Archer et al. (2009) predicted that these estimates would more likely lie in the range 1600 to 2000 GtC. In permafrost regions, estimates of the amount of gas hydrates are highly uncertain (approx.400 GtC) (MacDonald, 1990) and no estimates have been made of possible Antarctic reservoirs. An unknown amount of methane may be released if the predicted trend of future climate changes continues (Maslin *et al.,* 2010). Shakhova et al. (2010) presented evidence of increasing methane release from subsea permafrost on the East Siberian Arctic Shelf and further proposed that subsea permafrost would be extremely exposed to regional warming. Gas hydrate deposits situated at the polar continental shelves are regarded as most vulnerable to global climate change (Kvenvolden, 2000). Archer et al. (2009) used state-of –the-art modelling and calculated that 35 to 940 GtC could escape if a global warming of 3°C occurred. However, he pointed out that large uncertainty lies within the assumption of how much methane would be oxidized into the overlying ocean. To successfully evaluate the environmental impact of methane release to the atmosphere, more research is required to quantify the amount of methane stored in gas hydrates deposits and the free gas below, as well as an understanding of their limits of stability (Maslin *et al.*, 2010).

1.3.3 Gas hydrates as a geohazard

The impact of gas hydrate dissociation on slope stability have become an increasingly important issue. Formation of gas hydrates alter the physical properties of host sediments by reducing porosity and permeability and hence increases sediment shear strength (Kvenvolden, 1993[a]). On the contrary, dissociation of gas hydrates freshens the sediments with water and gas, which resultantly contribute to volume expansion. Depending on drainage conditions, the dissociation may cause a significant increase in pore pressure, decrease in effective stress and overall reduced sediment strength (Nixon and Grozic, 2006).

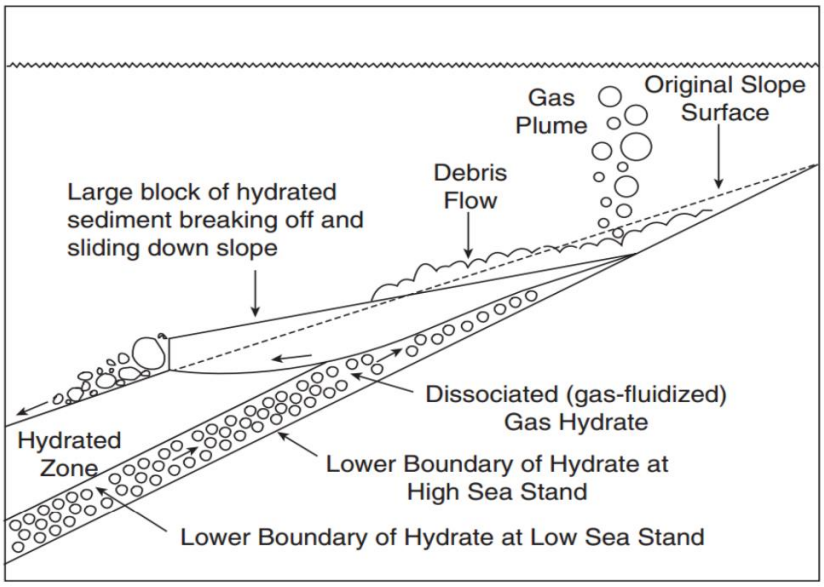

Figure 1-3: A model illustrating mass movement in slope-settings. A large solid block break off and slides along a hydrate-decomposition glide plane (from McIver, 1982).

The link between gas hydrate dissociation and slope failure was first raised by McIver (1982). He postulated that an increase of sedimentation rate or lowering of sea level may cause disturbance of the stability conditions for gas hydrates. If the sea level rises, the hydrostatic pressure increases making gas hydrates to stabilize at greater depths. A lowering of the sea level will in turn reduce the hydrostatic pressure and subsequently gas hydrates become unstable. These factors could initiate dissociation of gas hydrates at the base of the hydrate stability zone, which in turn would cause loss of cementation and gas release – creating weak sedimentary layers. The free gas trapped beneath the remaining gas hydrates would constitute a weak layer of over-pressurized sediments. This could then develop a glide plane, where massive wedges of hydrate cemented sediment could slide downslope (figure1-3) (Grozic, 2010). Recent research suggest that slope failures on continental margins around the world (Kvenvolden, 1993[a], 1999) and along the Norwegian continental margin may have been triggered by dissociation of gas hydrates (Jung and Vogt, 2004; Sultan et al., 2004[a], 2004[b]; Mienert *et al.*, 2005).

Submarine landslides might damage offshore equipment and jeopardize the safety of personnel. Tsunamis can as well be generated, which could impact coastal regions hundreds kilometers away (Locat and Lee, 2002). Additionally, gas hydrates and the underlying zone of free gas serve as a significant drilling hazard in the offshore petroleum industry. Presence of gas hydrates may cause trouble in borehole-wells in terms of gas leakage to the surface, borehole instability and collapsed casings. As offshore exploration-activity move into deeper waters and to higher latitudes in the Arctic, gas hydrate related problems will most likely increase. Areas that could potentially store gas hydrates must therefore be given significant attention prior to drilling (Yakushev and Collett, 1992; Nimblett *et al.*, 2005). If pressure and temperature conditions are within the range of gas hydrate stability, gas hydrates can spontaneously form and clog production equipment and pipelines.

1.4 A short introduction of the study areas

Gas hydrate provinces on the mid-Norwegian (Mienert *et al.*, 1998; Bouriak *et al.*, 2000; Bünz *et al.*, 2003; Hustoft *et al.*, 2007; Plaza-Faverola *et al.*, 2012) and Svalbard Margins (Vogt *et al.*, 1994; Posewang and Mienert, 1999[b]; Vanneste *et al.*, 2005[a]; Smith *et al.*, 2014) are subject to an ongoing extensive research. Widespread BSRs, fluid migration pathways and pockmarks at the seafloor characterize the seismic data within these areas. Both areas represent areas of relatively high seismicity and show occurrence of seepage structures and pockmarks in areas were BSRs are identified on seismic data (Vogt *et al.*, 1999). However, high-resolution 3D seismic data has revealed a pronounced difference in acoustics character between the seepage structures at these different locations (Bünz *et al.*, 2009). The gas hydrate province in the western Svalbard margin differs from the mid-Norwegian margin by having heat flow values on average two to three times higher, inferring a geothermal driven gas hydrate system (Vanneste *et al.*, 2005[a]; Bünz *et al.*, 2008).

1.4.1 Vestnesa Ridge

Vestnesa Ridge represents one of the northernmost gas hydrate provinces. It has its location on the western Svalbard margin in the eastern Fram Strait at ~79°N, north to the Molloy transform fault (MTF) and north to the Knipovich ridge (figure 1-4) (Petersen *et al.*, 2010; Bünz *et al.*, 2012). The Knipovich ridge represents the northernmost extension of the Mid-Atlantic Ridge system and abuts the lower slope of the Svalbard margin at 78.5°N (Thiede and Myhre, 1996; Vanneste *et al.*, 2005[b]). Vestnesa Ridge is a 100 km long submarine sediment drift situated on hot (>115 mW/m^2) and relatively young (< 20 Ma) oceanic crust at the eastern spreading segments of the Molloy Ridge (Engen *et al.*, 2008; Hustoft *et al.*, 2009). The ridge elongates in a SE-NW to EW- bending direction, where the crest of the ridge lies at 1200-1300 m water depth (Bünz *et al.*, 2012).

Sediment thickness increases going from 1 km in the west towards the east where it reaches > 2km (Vogt *et al.*, 1994). The sediment drift is made up of contourite, turbidite and hemipelagic sediments that has been partly reworked by bottom currents (Howe *et al.*, 2008). The stratigraphy are divided into three main sequences; YP1 (oldest), YP2 and YP3 (youngest) (Figure 10 in; Eiken and Hinz, 1993). Section YP1 consist of syn- and post-rift deposits above the oceanic crust (Hustoft *et al.*, 2009), whereas YP2 is characterized by contourites. The YP2/YP3 boundary represent an unconformity and mark the onset of the Plio-Pleistocene glaciations and depositions (Eiken and Hinz, 1993: Hustoft *et al.*, 2009). Sediments covering the crest of the ridge mainly consist of silty turbidites and muddy-silty contourites from late Weichselian to Holocene age (Howe *et al.*, 2008; Hustoft *et al.*, 2009).

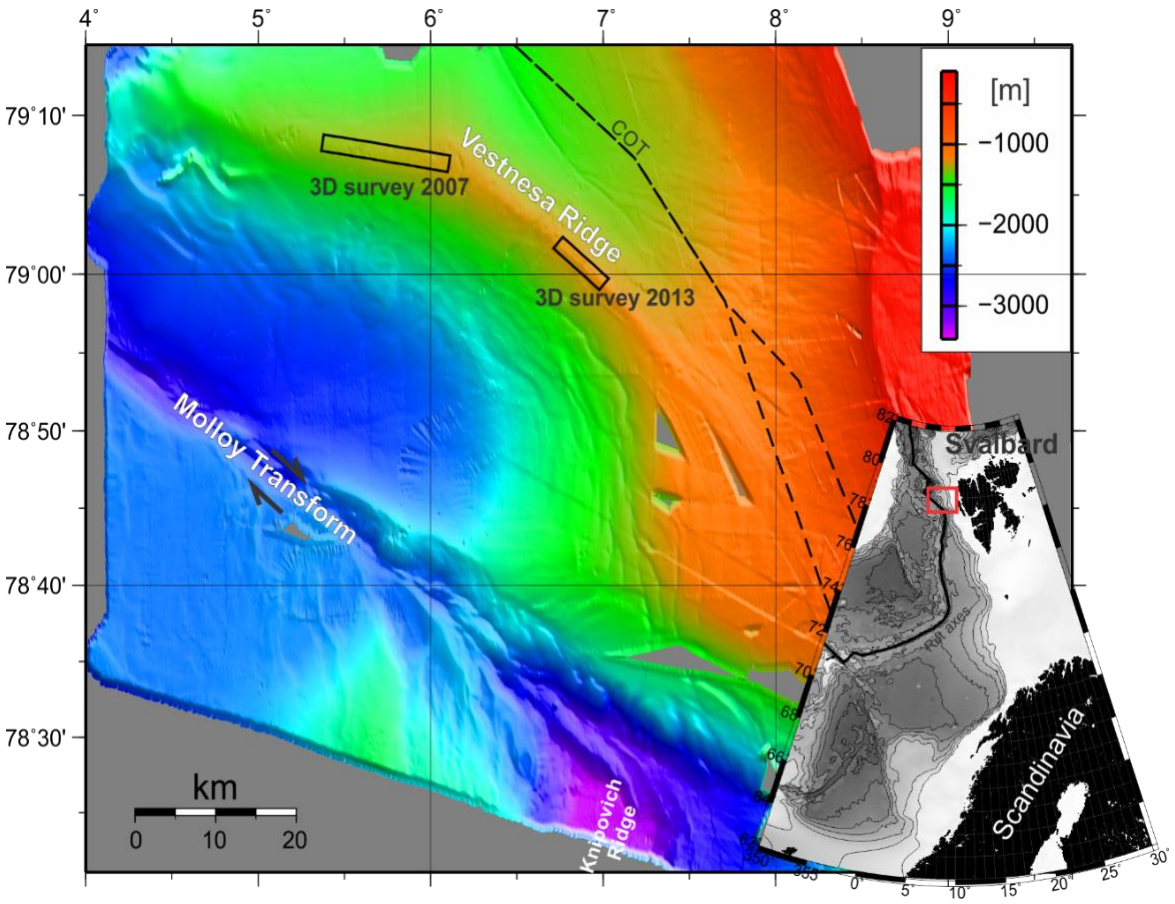

Figure 1-4: Overview map of Vestnesa Ridge, offshore West Svalbard margin. The boxes indicates location of the two 3D seismic surveys used in this thesis; Vestnesa.3D.2007 located on the western segment and Vestnesa.3D.2013 on the eastern segment of the ridge. COT denotes the continent-ocean transition (Engen et al., 2008) (modified from Bünz *et al.*, 2012).

The Fram Strait represents the only gateway for deep-water exchange between the relatively warm and saline Atlantic Ocean and the cold Arctic Ocean (Eiken and Hinz, 1993; Howe *et al.*, 2008; Werner *et al.*, 2011) and is dominated by two main surface currents: the West Spitsbergen Current (WSC) and the East Greenland Current (EGC) (Howe *et al.*, 2008). At high latitude the North Atlantic Current (NAC) branches into the West Spitsbergen Current (WSC) which transports the main flux of warm Atlantic water masses through the eastern Fram Strait and into the Arctic basin. At the western part of the Fram strait, the southward directed East Greenland Current (EGC) carries cold polar water and sea ice along the Greenland continental slope. As a result of these two currents, the western Fram Strait is perennially covered by sea ice, whereas ice conditions varies seasonally in the eastern part (Werner *et al.*, 2011). Variations in intensity of the WSC influences the heat budget and sea ice extent within the Fram Strait (Werner *et al.*, 2011). It is also considered as the governing factor shaping the morphology of the Vestnesa Ridge (Bünz *et al.*, 2012).

1.4.2 Northern flank of the Storegga slide area, mid-Norwegian margin

The mid-Norwegian margin is a known hydrocarbon province (e.g. Ormen Lange gas reservoir) as well as being the location of the Storegga Slide complex. The Storegga slide event occurred ~ 8.2 ka B.P. and is the largest known submarine sediment slide. The run-out distance covered around 800 km and moved a total of 3500 km^3 of sediments (Bryn *et al.*, 2005; Haflidason *et al.*, 2005). The triggering factor has been widely discussed and linked to both earthquakes and slope instabilities due to gas hydrate dissociation, or a combination of these effects (Bugge *et al.*, 1987; Mienert *et al.*, 2003). Through the northeastern flank of the slide scar, a prominent BSR has been detected on seismic data and resultantly the cause of mass-movement has been inferred to be linked to dissociation of gas hydrates (Bugge, 1983; Mienert *et al.*, 1998). The generation of mass-movement in this area has further been related to a tsunami that hit the west coast of Norway, Scotland, Shetland and the Faroes (Bondevik *et al.*, 2003).

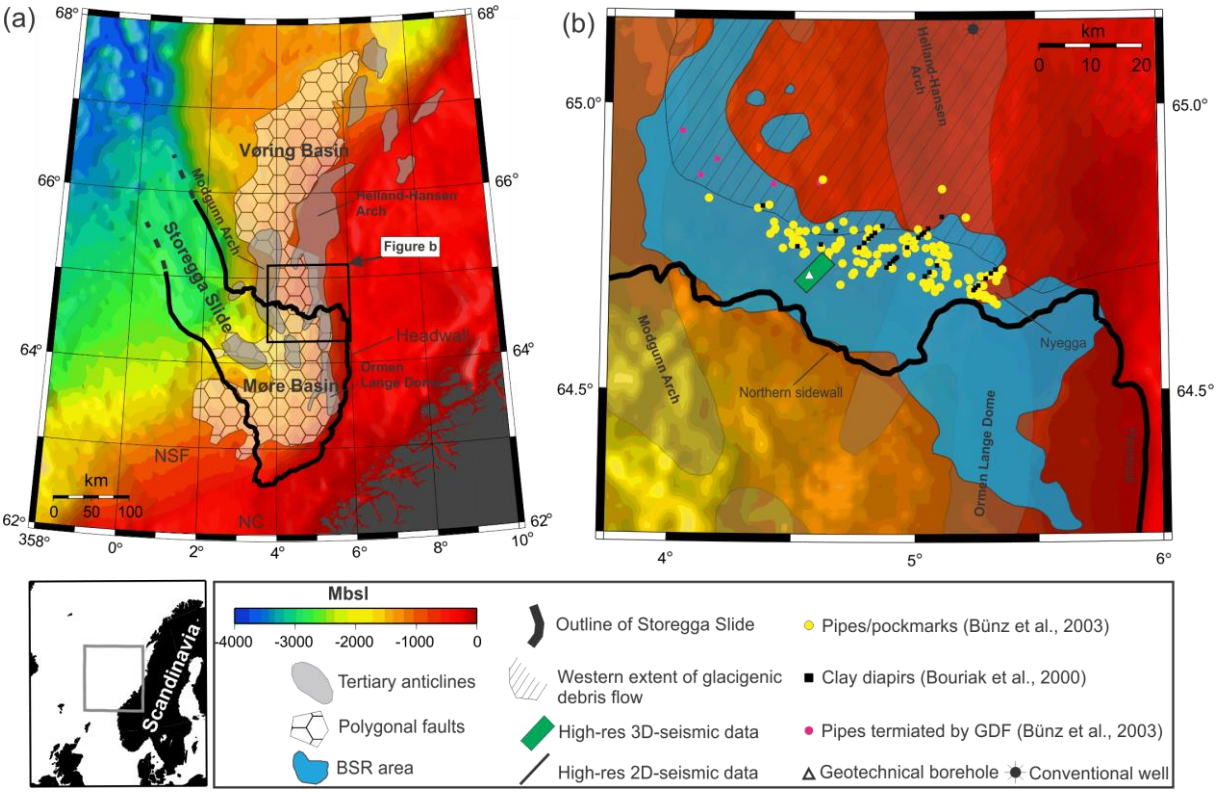

Figure 1-5: (a) Shaded relief map of the mid-Norwegian margin, indicating the study area at the northern flank of the Storegga slide complex. (b) Showing location of the acquired high-resolution 3D seismic dataset (green box) Hydratech.3D north to the northern sidewall (modified from Hustoft *et al.*, 2007).

The study area at the mid-Norwegian margin is located at the transition between the Vøring and Møre Basin - north of the northern Storegga slide escarpment (Bünz *et al.,* 2003) (figure 1-5 b; green box). More precisely, the 3D high-resolution seismic dataset is located north to the northern sidewall of the Storegga Slide. Figure 1-5 show the widespread occurrence of BSR, polygonal fault-network, as well as fluid flow features on the formerly glaciated margin.

The sedimentary successions within the study area are divided into the Brygge, Kai and Naust Formations. The main sedimentary sequences that involve gas hydrate and fluid flow systems are the Kai and the overlying Naust Formation. The Kai Formation consist predominantly of fine-grained hemipelagic oozes from Late Miocene to early Pliocene. Deposits of the Naust Formation comprises debris flow deposits and hemipelagic contouritic sediments formed by Plio-Pleistocene glacial-interglacial cycles (Rokoengen *et al.,* 1996; Hjelstuen *et al.,* 2005). Hjelstuen et al. (2005) presents a detailed review of the stratigraphy of the mid-Norwegian margin, which is only briefly described in this thesis. Occurrence of densely spread polygonal faults exist within the Kai Formation in the Vøre and Møre Basins (Berndt *et al.,* 2003; Hustoft *et al.,* 2007). Several fluid flow structures has been discovered to evolve from the base of the Naust Formation and continuing all the way to the seafloor (Hustoft *et al.,* 2007). The polygonal fault system is suggested to control fluid flow and supply gas-rich fluids to the gas hydrate system (Berndt *et al.,* 2003).

2. Fundamental theory

2.1 Gas hydrates

Gas hydrates are ice-like crystalline compounds arranged in a framework of water molecules that encloses gas molecules of low-molecular weight, preferably methane (Sloan, 1998). With sufficient supply of gas and water, they form naturally and replace pore fluid in sediments within a limited pressure- and temperature region, termed the gas hydrate stability zone (GHSZ) (Hyndman and Davies, 1992). In addition to pressure and temperature conditions, the hydrate stability is affected by various parameters which are presented in the next section (2.2). Occurrence of natural submarine gas hydrates are commonly inferred by the presence of a bottom-simulating reflectors (BRSs) in seismic data, marking the base of the hydrate stability zone (Shipley *et al.*, 1979).

Gas hydrates in sediments may form as cement in the pore space, as a layered structure, as nodules of pure hydrate or in a disseminated form within the pore space (Chand and Minshull, 2003). Pore-filling hydrate reduces the porosity and permeability of the host sediments and efficiently trap upward migrating free gas below the base of the hydrate stability zone (BGHSZ) (Dillon *et al.*, 1980; Hornbach *et al.*, 2004). However, there are large uncertainties to how gas hydrates are distributed within marine sediments (Tréhu *et al.*, 2004). Recent research has revealed a strong relationship between sediment grain size and gas hydrate saturation (Tréhu *et al.*, 2004; Riedel *et al.*, 2009; Lu *et al.*, 2011). Coarse-grained sediments are found to be preferable for pore-filling hydrates, whereas fine-grained sediments (i.e. shale) are suggested prone to fracture-filling hydrates as veins or nodules (Bahk *et al.*, 2011). As the above mentioned hydrate morphologies may affect the physical properties of the host sediment differently (Chand and Minshull, 2003), information on the gas hydrate morphologies are important to develop accurate models to estimate the in situ gas hydrate content from seismic methods (Tréhu *et al.*, 2004).

2.2 Hydrate stability

The occurrence of gas hydrates in nature are mainly controlled by a combination of low temperature and high pressures confined within a zone known as the gas hydrate stability zone (GHSZ). These specific P-T conditions are met globally in continental margins and permafrost regions (Kvenvolden, 1993[a]). Hydrates crystallize within the GHSZ when concentration of dissolved methane exceeds hydrate solubility and is therefore dependent on influx of free gas (Sloan, 1998). The maximum sub-bottom depth for hydrate stability depends on pressure (function of water depth), seafloor temperature and the vertical temperature gradient, where the latter is affected by heat flow and thermal conductivity (Yuan *et al.*, 1998). Apart from P-T conditions, the thickness and location of the hydrate stability zone are affected by the gas chemistry, pore water salinity and availability of sufficient supply of gas (Lerche and Bagirov, 1998; Nixon and Grozic, 2006). Figure 2-1 show a phase boundary diagram demonstrating the gas hydrate stability zone for marine settings.

A BSR commonly marks the base of GHSZ, separating hydrate-bearing sediments above and free gas below. No gas hydrate occur below the GHSZ as the temperature and pressure are not suitable for hydrate stability (Chand and Minshull, 2003). The bottom-simulating behavior has shown a stronger dependency to temperature variations than to variations in pressure (Vanneste *et al.*, 2005[b]). Hence, from the depths of the BSR geothermal heat flow values can be determined by using relationships among the physical properties of marine sediments, providing useful information regarding the distribution of heat flow (Yamano *et al.*, 1982). This method can provide detailed estimates of the lateral variations of heat flow (Vanneste et al., 2005[b]).

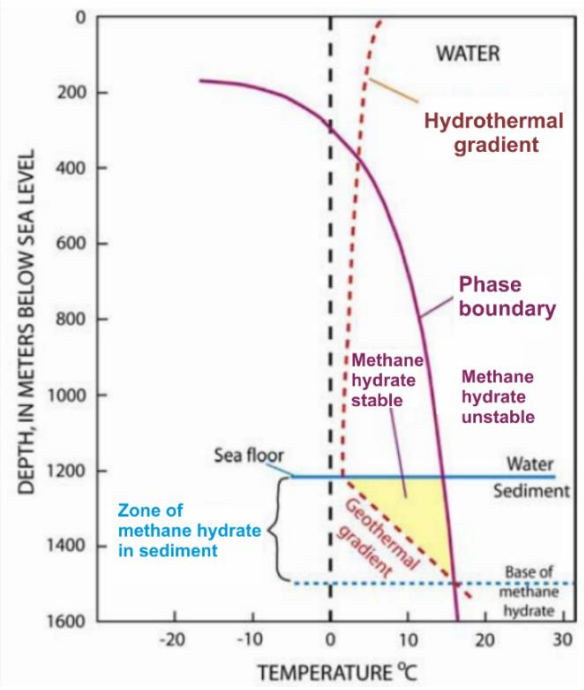

Figure 2-1: Phase diagram of the hydrate stability zone in marine settings (from Sloan *et al.*, 2010)

2.3 Characteristics of the BSR

As previously mentioned, BSRs observed on seismic data are commonly used to indicate the distribution of submarine gas hydrates and generally corresponds to the base of the gas hydrate stability zone (BGHSZ). This phase boundary is believed to mark the transition between sediments containing gas hydrates above and free gas below (MacKay *et al.*, 1994; Bünz and Mienert, 2004; Haacke *et al.*, 2007). However, some deviations might occur because of host sediment properties and chemical compositions of the pore fluid (Chand and Minshull, 2003).

Figure 2-2 illustrate the seismic characteristics of the BSR. Bottom simulating reflectors (BSR) are characterized by broadly mimicking the seafloor topography as well as appearing with a reversed polarity relative to the seafloor reflection (Shipley et al., 1979; Hyndman and Spence, 1992; Pecher et al., 1996). The BSRs reversed polarity event relative to the seafloor reflection is caused by a negative impedance contrast, thus indicating a large decrease in acoustic impedance across the interface (MacKay *et al.*, 1994; Pecher *et al.*, 1996; Bünz and Mienert, 2004; Haacke *et al.*, 2007). Consequently, it generally appears as an event of anomalous strong reflection in seismic data. However, the BSR often appears with variable amplitude and character and the magnitude of the amplitude may range from lower to even higher than that of seafloor (Minshull *et al.*, 1994; Andreassen *et al.*, 1995).

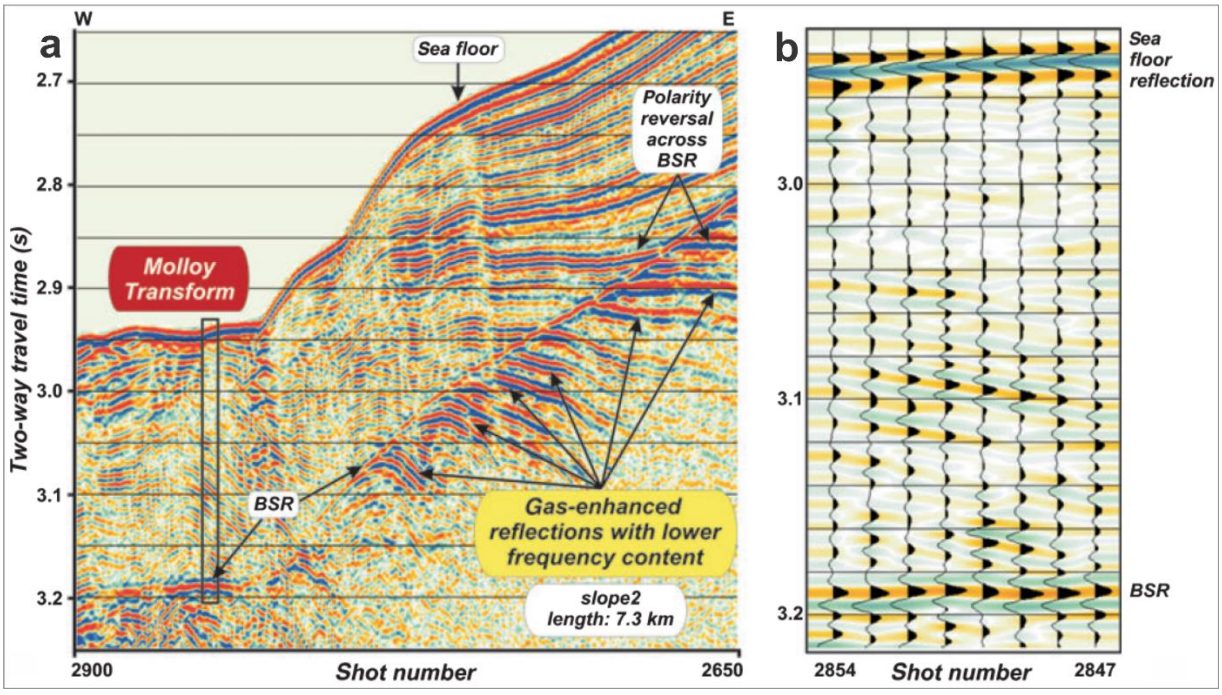

Figure 2-2: Illustrates seismic characteristics of the BSR. (a) The BSR follows the seafloor topography, cross-cutting sedimentary layers and with enhanced reflections below. (b) The BSR is recognized with a polarity reversal compared to the seafloor reflection (from Vanneste *et al.*, 2005[b]).

The BSR occurs at temperature and pressure conditions where gas hydrates are no longer stable, hence following isotherms rather than stratigraphic horizons. This entails that its appearance is commonly recognized by termination of enhanced reflections cross-cutting sedimentary strata. When the BSR parallels primary sedimentary bedding it is not readily apparent and resultantly more difficult to detect on seismic data (Hornbach *et al.*, 2003; Bünz and Mienert, 2004). Whether the BSR appear as a continuous reflection in its own right or as termination of enhanced reflections is a matter of resolution of the data (Wood *et al.*, 2002).

If any of the parameters controlling the hydrate stability zone changes, it follows that the phase boundary shift up- or downwards and consequently changing the location of the BSR (Chand and Minshull, 2003). A displacement of the hydrate phase boundary might leave a seismic expression of a double BSR, one active BSR boundary and one paleo-BSR (Posewang and Mienert, 1999[a]; Foucher *et al.*, 2002; Hornback *et al.*, 2003). Figure 2-3 illustrates how the dynamic and active BSR adjusts to erosional changes, leaving a residual hydrated paleo-BSR above (Hornbach *et al.*, 2003). Observation of BSRs are important for identifying the occurrence of gas hydrates and the underlying free gas. However, it does not provide information regarding the concentration of hydrates or the extent of distribution between the BSR and the seafloor (Westbrook *et al.*, 2008[a]).

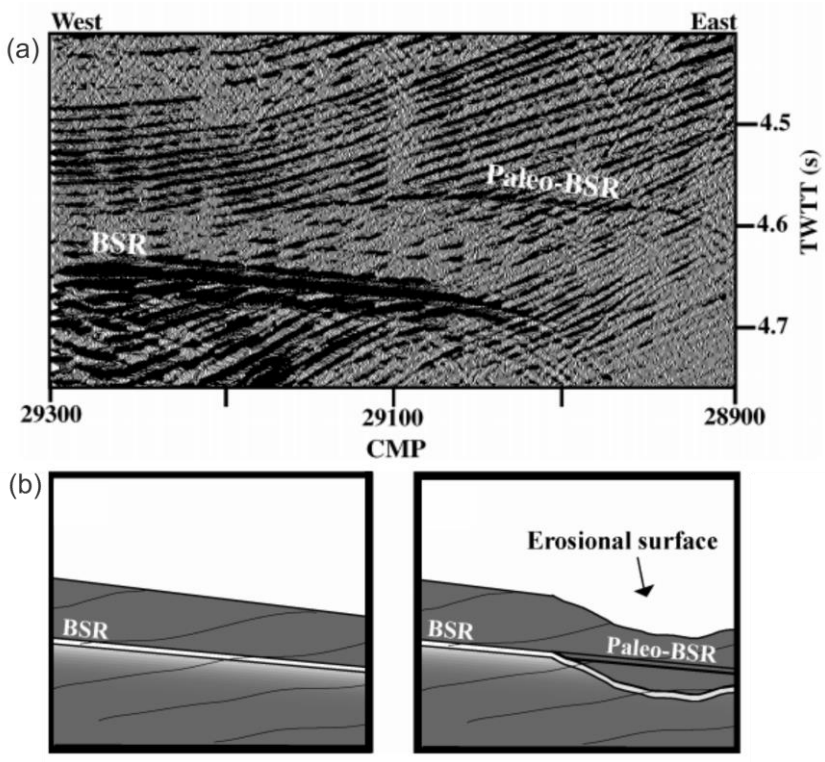

Figure 2-3: (a) True-amplitude variable wiggle trace of a BSR and Paleo-BSR. (b) Cartoon showing the development of a paleo-BSR consisting of hydrate. Figures from Hornbach et al. (2003).

2.4 Elastic properties

Whether the BSR originate from the concentration of free gas below or as a result of the overlying hydrate-bearing sediments has served as a topic for debate (Shipley et al., 1979; Hyndman and Spence, 1992). The origin of the bottom-simulating reflector has been widely discussed and two interfaces have been proposed to explain the nature of the BSR both of which give rise to a strong negative impedance contrast:

1) Either as a result from an impedance contrast between significant amounts of high-velocity hydrate-bearing sediment overlying water-filled sediments with typical velocities (Hyndman and Spence, 1992).
2) Or due to sediments containing small amounts of hydrate overlying low-velocity gas-saturated sediment (Singh *et al.,* 1993; MacKay *et al.,* 1994; Minshull *et al.,* 1994)

Sediments containing only a small quantity of free gas would lower P-wave velocity dramatically, but have little effect on the S-wave velocity. A further increase of gas saturation would only moderately contribute to an additional decrease of P-wave velocity (Domenico, 1976). A substantial amount of pore-filling hydrate will elevate both P- and S-wave velocity compared to sediments containing regular pore-fluids and be able to produce a noticeable reflection on seismic data, thus the BSR may be a composite hydrate/gas reflection (Hornbach et al., 2003). The density will only show a minor decrease with increased concentrations of hydrate and free gas (Andreassen *et al.,* 1995). The high elastic velocities of gas hydrate, both compressional and shear wave velocities has further been confirmed by drilling of gas hydrates, such as the well Mallik 2L-38 in northern Canada and ODP Leg 164 wells at Blake ridge, where they demonstrated the link between gas hydrates saturations and elastic rock properties (Dai *et al.,* 2004).

Several studies have shown that most of the reflection amplitude is associated with a drop in P-wave across the BSR due to the free gas below - and to a lesser extent by the hydrate above (MacKay, 1994; Andreassen *et al.,* 1995; Holbrook *et al.,* 1996; Haacke *et al.,* 2007). However, ocean bottom drilling has proven the existence of hydrate sediments where no BSRs were acoustically identified, as was discovered at Blake Ridge (e.g OPD-164 site 994) (Holbrook, 2001) and Lake Baikal (Vanneste *et al.,* 2001). These studies emphasize that the complex relationship between formation of BSR and its relation to gas hydrate formation are not yet fully understood.

Since the appearance of BSRs on seismic data are only indicative of a gas hydrate-free gas system and does not provide information regarding the distribution or amount of hydrate, further investigation such as velocity modelling and amplitude variation with offset (AVO) analysis are crucial to support seismic indications.

Prior to AVO modeling, the elastic properties of sediments must be obtained. Several attempts to establish properties of hydrate sediments directly from core samples (Kvenvolden and Barnard, 1983; Mackay *et al.*, 1994) have failed due to the instability of hydrate at surface temperatures and pressures. As a result, elastic properties are commonly estimated from seismic data (Hyndman and Spence, 1992; Minshull., et al 1994; Ecker *et al.*, 1998). Numerous seismic investigations have focused on P-wave velocity behavior around the BSR and only incorporating S-wave velocities based on laboratory results (Ecker and Lumley, 2001). As S-waves exhibit a higher sensitivity to concentrations of hydrate compared to P-wave velocities, recent research has pointed out the importance of considering reliable shear wave information to obtain detailed information of elastic parameters (Ecker *et al.*, 1996; Ecker and Lumley, 2001; Petersen *et al.*, 2007). S-wave velocities can be obtained by deploying Ocean bottom seismometers (OBS) (Petersen *et al.*, 2007) or Ocean bottom cable (OBC), allowing S-wave velocities to be determined by analysis of PS-converted waves (Bünz and Mienert, 2004).

Another aspect that influences the physical properties of the hydrate-bearing sediments is the actual effect of the positioning of hydrate in the pore space. Several rockphysic models have been proposed to quantify this effect (Dai *et al.*, 2004). The cementation model from Dvorkin and Nur (1996) treat grains as randomly packed spheres where the gas hydrates cement the grain contacts. This models would strongly reinforce the sediment (Ecker *et al.*, 1998) and consequently predict a large increase in P-wave velocity with hydrate saturation. Other models consider the gas hydrates as a part of the load bearing matrix or as pore-fill (Laird and Morley, 2011).

2.5 Gas hydrate, free gas and fluid flow

Seismic indications of focused fluid flow such as gas chimneys, mud volcanoes, pockmarks and carbonate mounds are frequently observed in relation to gas hydrate systems (Bouriak *et al.*, 2000; Cartwright et al., 2007; Hustoft *et al.*, 2007; Plaza-Faverola *et al.*, 2010). The occurrence of fault zones within gas hydrate regions are regarded as a migration pathway for deeper seated sources and reservoirs (Berndt *et al.*, 2003; Plaza-Faverola *et al.*, 2012) and as a controlling factor for the distribution of the above mentioned fluid flow features (Berndt *et al.*, 2003; Judd and Hovland, 2007; Plaza-Faverola *et al.*, 2015). These migration pathways may act as a significant source of methane into the hydrate system and contribute to the distribution of gas hydrates in the shallow subsurface (Davies and Clarke, 2010; Bünz et al., 2012), as illustrated in figure 2-4. Evidence that free gas migrates through the GHSZ and leaks into the water column has been detected acoustically at gas hydrate provinces at Vestnesa Ridge (Bünz *et al.*, 2012; Smith *et al.*, 2014) and the South Hydrate Ridge (Bangs *et al.*, 2011).

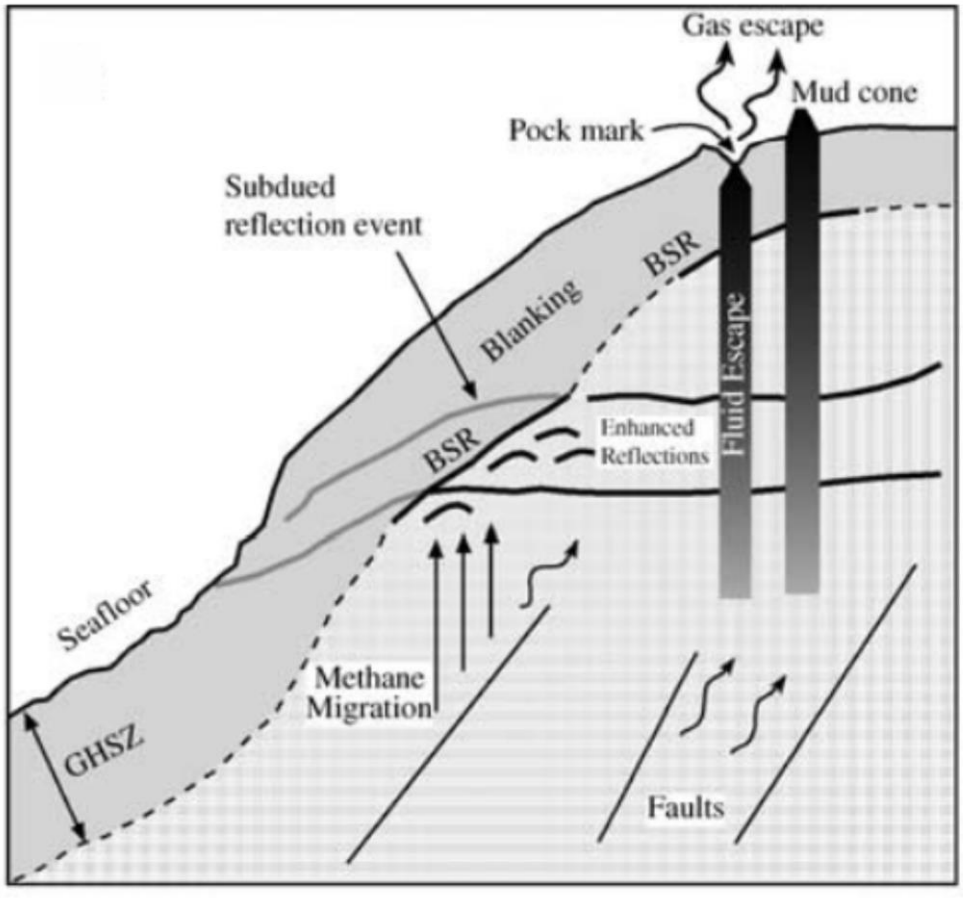

Figure 2-4: Schematic illustration of the gas-hydrate related features along a passive continental margin. major features observed include subdued reflection events within the GHSZ, blanking, enhanced reflection below the BSR, acoustic turbidity, and fluid escape features such as wipe outs, pockmarks and mud volcanoes. Figure from Chand and Minshull (2003).

The formation of a free gas zone (FGZ) beneath the GHSZ are suggested by many authors to sustain the gas hydrate formation (Hornbach *et al.,* 2004; Haacke *et al.,* 2007). Mechanisms of free gas accumulation beneath the hydrate stability zone (GHZS) has been explained to originate from various processes. One explanation originate from hydrate recycling, where gas is generated from hydrate dissociation by the upward shift of the BGHSZ relative to the hydrate-bearing sediments (Paull *et al.,* 1994; Pecher *et al.,* 1996; Haacke *et al.,* 2007). Another explanation is that the FGZs are sourced by dissolved methane in upward moving pore fluids that migrates into the GHSZ. The buoyant fluids migrate upward and laterally along the BGHSZ, where formation of gas hydrate provide a sealing effect and consequently allow further accumulation of free gas below (Vogt et al., 1994).

The accumulation of free gas trapped beneath hydrated sediments are also suggested as a linkage to chimney development, as continued supply of gas may induce a pressure build-up. The overpressured zone may then be released through the formation of new chimneys or by reactivating old fluid pathways (Plaza-Faverola et al., 2011; Bünz et al., 2012).

2.6 Frequency dependence of the BSR

Presence of gas hydrates are commonly inferred by detection of a BSR in seismic data. Different types of reflection seismic data has revealed that BSR appearance differs due to the frequency range and survey geometries used during acquisition (Vanneste *et al.*, 2001; Wood *et al.*, 2002; Chapman *et al.*, 2002). On conventional low-frequency seismic data (10-50 Hz) the BSRs are generally depicted as a laterally continuous high-amplitude reflection with reversed polarity, that often cross-cut the local stratigraphy (Vanneste *et al.*, 2001; Wood *et al.*, 2002). A study by Chapman et al. (2002) reported that even with higher frequency systems, the spatial resolution of the BSR are limited by the conventional survey geometry (source-receiver at the sea surface). Figure 2-5 displays the different BSR characteristics detected from conventional seismic data and seismic data acquired by deep-towed acoustic/geophysics systems (DTAGS).

On high-frequency seismic data, the BSR are no longer expressed as a single reflector, but rather appear as the upper boundary of closely spaced high-amplitude reflections terminating at the BGHSZ. Additionally, amplitude and continuity has been detected to decrease on high- frequency data (Vanneste *et al.*, 2001) (figure 2-5 a). The BSRs reflection coefficient has been observed to decrease with increasing air-gun frequencies (15-175) (Fink and Spence, 1999), and an even larger decrease was observed from DTAGS (250-650 Hz) (Chapman *et al.*, 2002).

The reduced BSR amplitudes observed in high-frequency data can be explained by a vertical velocity gradient that is gentle (less reflective), whereas the strong amplitudes in low-frequency data by a sharper velocity gradient (more reflective) (Wood et al., 2002). Vanneste et al. (2001) explained the reflection-amplitude variations to result from the differences in frequency-controlled horizontal (Fresnel zone) and vertical resolution. A low-frequency source samples a larger sub-surface volume than a high-frequency source. For the larger volume, physical properties that contribute to the reflection strength are averaged out, whereas for the smaller volume sampled by higher frequencies, small-scale lateral variations become more important and may result in a reduction of the reflectivity.

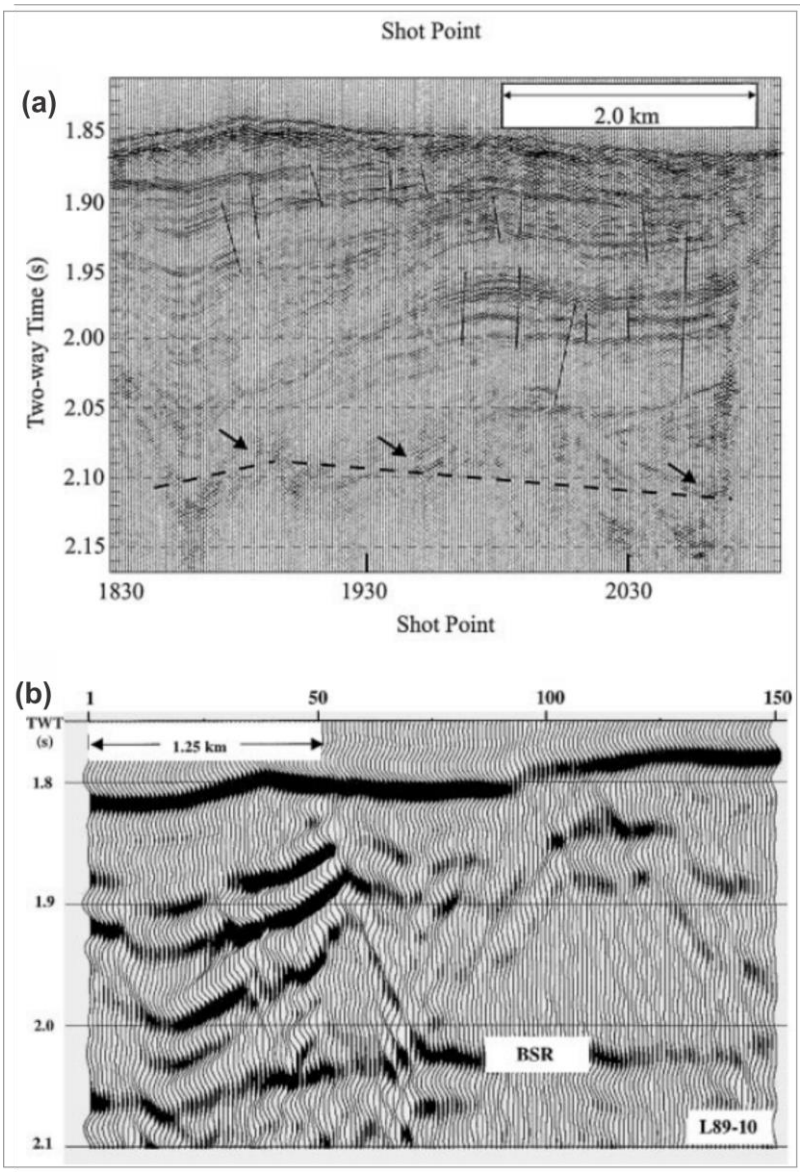

Figure 2-5: Comparison of BSR appearance with low- and high frequency data. (a) deep-towed acoustic/geophysics systems (DTAGS) (b) Conventional low-frequency multichannel (from Chapman *et al.*, 2002).

3. Data and Methods

3.1 High-resolution 3D seismic data

Two datasets from the Vestnesa Ridge in addition to one dataset from the northern flank of the Storegga slide area on the mid-Norwegian margin are used in this study (figure 3-1).

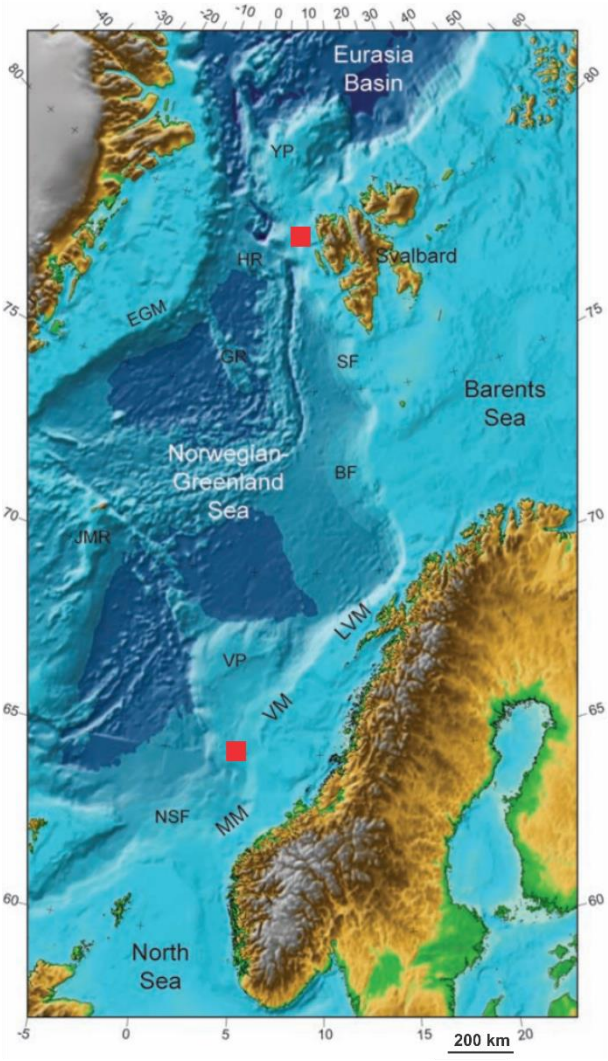

Figure 3-1: Overview of the Norwegian and Svalbard margins. Red squares indicate the regional settings of the study area from Vestnesa Ridge and the northern flank of the Storegga slide area. VM: Vøring Margin, MM: Møre Margin. (Modified from Faleide et al., 2008)

3.1.1 Vestnesa Ridge

The two high-resolution 3D seismic datasets from Vestnesa Ridge were acquired in 2007 (Vestnesa.3D.2007) (Petersen *et al.*, 2010) and 2013 (Vestnesa.3D.2013) (Plaza-Faverola *et al.*, 2015) by using the P-cable system on R/V Helmer Hanssen operated by the University of Tromsø. Vestnesa Ridge is situated offshore NW Svalbard at a water depth of~1200 meters (figure 3-1).

3.1.1.1 High-resolution P-cable system

The P-cable system was developed by Volcanic Basin Petroleum Research in close collaboration with the University if Tromsø, National Oceanography Centre of Southampton (NOCS) and Fugro Survey AS in Oslo (P-Cable, 2015). The aim were to achieve high-resolution surveying of shallow depths. Conventional 3D seismic data are generally restricted to high-resolution imaging of of deeper targets, which are particularly of interest for hydrocarbon exploration. For shallower depths, conventional 3D seismic data does not provide sufficient resolution to image shallow subsurface structures.

The spatial resolution of the P-cable system is improved by at least one order of magnitude, whereas temporal resolution is 3-5 times higher (Petersen *et al.*, 2010). High-resolution P-cable systems allow more accurate imaging of the gas hydrate/free-gas system and fluid flow systems (Bünz *et al.*, 2012). This system would also be beneficial to investigate sites prior to drilling with the aim to reveal possible drilling hazards at shallow sub-bottom depths. A part from being cost-efficient, the P-cable system have the advantage of being easily maneuvered by relatively small research vessels with only the need of a minimum crew onboard (Planke *et al.*, 2010).

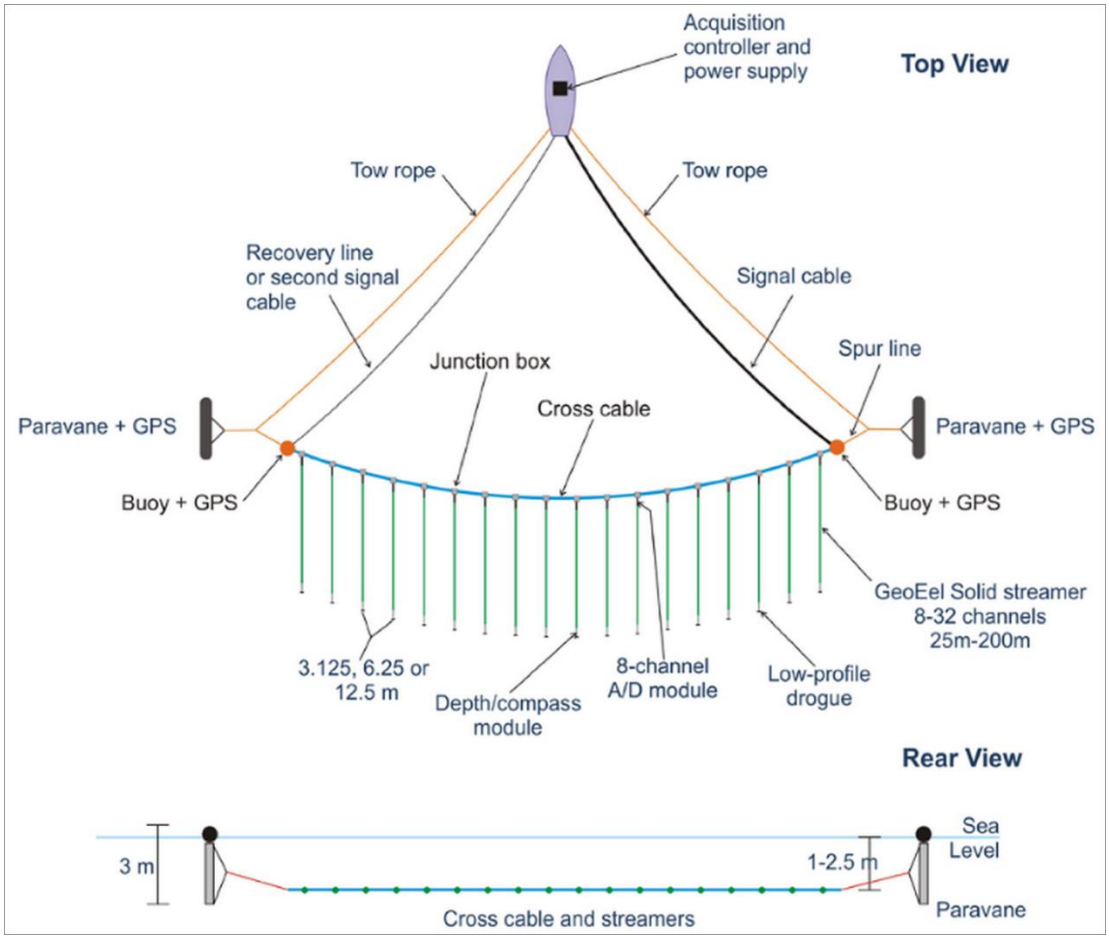

Figure 3-2: Basic layout geometry of the P-cable system (from P-Cable, 2015)

The P-cable system consists of a cross cable towed behind the vessel aligned perpendicular to the steaming direction. Acquisition of the dataset Vestnesa.3D.2007 used an array up to 12 parallel multi-channel streamers with length of 25 m. Each streamer contain eight channels, spaced with an interval of 12.5 m along the cross cable. Due to the curvature of the cross cable, the distance between streamers will range from 6-10 m. The cross cable is attached to two paravane doors, who provide the necessary horizontal lift as well as stretching the cross cable. To assure accurate navigation up to 1 meter, GPS antennas are placed on both the paravane doors and gun float. A GI gun source is towed behind the vessel, providing seismic energy with frequencies from 20-250 Hz (Bünz *et al.*, 2012). Processing details can be viewed in Petersen et al. (2010). A schematic illustration of the P-cable system is shown in figure 3-2.

The dataset from the eastern segment of Vestnesa Ridge, Vestnesa.3D.2013, were acquired using 14 streamers. Each streamer were 25 m long with 8 channels per streamer. The source consisted of a mini-GI gun with a peak frequency of 135 Hz. The migrated stack has lateral resolution of 6.25 m and vertical resolution of ~5 m (Plaza-Faverola *et al.*, 2015). Details of the processing can be found in Plaza-Faverola et al. 2015.

3.1.2 Storegga slide area

The "Hydratech" cruise on the vessel N/O Le Suroît in June 2002 surveyed a limited area north to the northern flank of the Storegga slide on the mid-Norwegian margin (Nouzé et al., 2004) (figure 3-6). The acquired 3D high-resolution dataset (Hydratech.3D) covered an area of ~28 km^2 at 1050-1150 m water depths. With a bin size of ~6 m and dominant frequency of ~80 Hz, the horizontal and vertical resolution were significantly improved compared to conventional industry 3D seismic data (Hustoft *et al.*, 2007).

The seismic layout consisted of two seismic streamers towed behind the vessel with a 25 m separation, each with 24 traces and length of 150 m. Two air gun (mini GI) sources were situated 12.5 m apart (figure 3-3). Differential GPS (DGPS) technology provided accurate positioning of source-receiver (Thomas *et al.*, 2004).

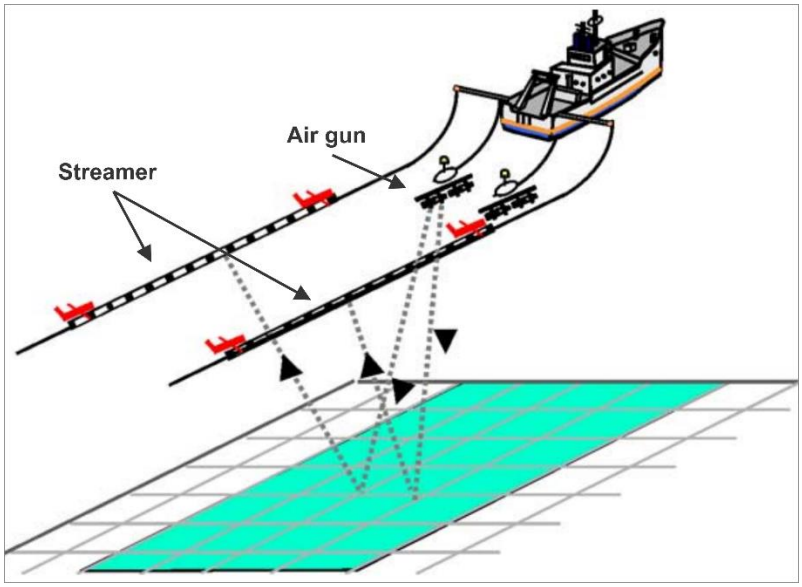

Figure 3-3: A view of the acquisition system for Hydratech.3D (Modified from Thomas *et al.*, 2004)

3.2 Seismic reflections

A seismic reflector represent an interface between two mediums where there is a change in acoustic properties. The acoustic properties of a medium are defined by its acoustic impedance (Z), the product of density (ρ) and velocity (V) (figure 3-4; equation 1). A seismic reflection is generated at an interface between two mediums with sufficient differences in acoustic properties, such as velocity and density. If the change in impedance across a boundary is small, the amount of reflected energy is small. Similarly, for a large impedance contrast, the reflected energy is large and thus produces greater amplitudes. The reflection coefficient is a measure of the strength of a reflection generated at an interface between two mediums (figure 3-4; equation 2). It can be positive or negative, where a positive value reflects an overlying medium (Z_1) with lower acoustic impedance than the medium below (Z_2). The opposite situation will produce a negative reflection coefficient. The latter is typically seen in reflection seismic data when non-gas charged sediments overlie gas charged sediments.

$$Z = \rho V \qquad (1)$$

$$R = \frac{(Z_2 - Z_1)}{(Z_2 + Z_1)} \qquad (2)$$

Figure 3-4: Equation 1 represents a mediums acoustic impedance (Z), which is the product of the density of the medium and the velocity of the seismic wave propagation through the medium. Equation 2 calculates the seismic reflection coefficient (R), which is a measure of the strength of a reflection generated at an interface between two mediums (Andreassen, 2009).

3.3 Seismic resolution

The earth itself acts as a low-pass filter, attenuating higher frequencies more readily than the lower frequencies. Consequently, the longer distances the elastic wave propagates through earth, the more high-frequency energy is lost to attenuation. Surveys with intensions to image targets at great depth is favored by choosing peak frequency at the lower range, as high frequencies are quickly attenuated resulting in no or little reflection to reach the receiver. Thus, the target depth will influence the choice of sources, survey geometry and sampling rates (Bulat, 2005).

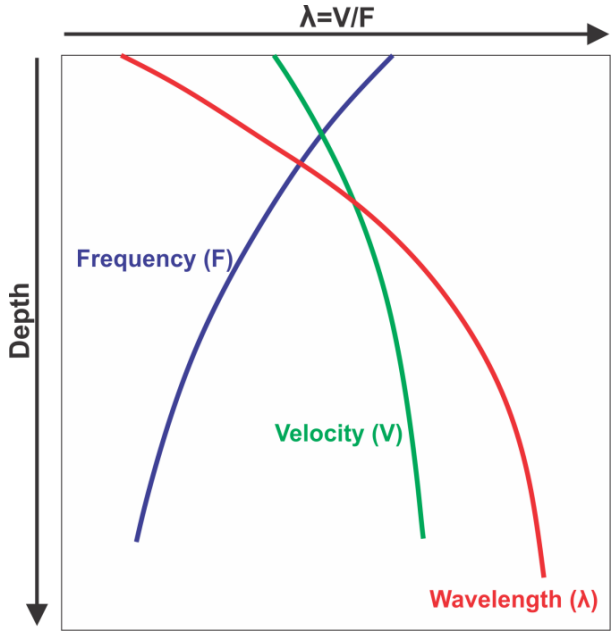

Figure 3-5: The relationship and variation between the parameters determining the seismic resolution. With increasing depth, frequency content decreases, while velocity and wavelength increases. The wavelength increases considerably with depth, resulting in a lower resolution (modified from Brown, 1999).

In seismic data, depth is commonly measured in milliseconds two-way-travel time, representing the time from which the sound wave leaves the source, reaches the reflector and returns to the receiver. Seismic resolution is the ability to distinguish between two objects and comprises both horizontal and vertical aspects. The resolving power of seismic data is determined by the wavelength, which in turn is dependent of the quotient of velocity and peak frequency (Figure 3-5). Seismic velocity increases with depth due to a gradual compaction of sediments. At the same time, attenuation of energy reduces the frequency content. The combined effect causes an increase in wavelength with depth, resulting in poorer resolution (Brown, 1999).

3.3.1 Vertical resolution

Vertical resolution refers to the ability to separate two close seismic events corresponding to different depth levels (Bulat, 2005). Vertical resolution is defined as ¼ of the wavelength (λ), representing the minimum thickness for two interfaces to be discerned in seismic data. If beds are thinner than ¼ of the wavelength (limit of separability), the top and base reflections will still be visible, but the amplitude will gradually deteriorate until the limit of visibility is reached (λ/30) (Brown, 1999).

3.3.2 Horizontal resolution

Horizontal resolution is the minimum distance between two features placed laterally along an interface to be identified as two separate events. On unmigrated data the horizontal resolution is defined as the width of the first Fresnel zone (figure 3-6 b). The seismic wavefront sent out from the source travels in three dimensions and disseminate over a roughly circular area. The Fresnel zone is the part of a reflecting interface covered by the seismic signal at a certain depth (Denham and Sheriff, 1981). Equation 3 and 4 (figure 3-6 b) shows that the Fresnel zone increases with depth due to increasing velocity and lower frequency. Features that surpass the lateral extent of the Fresnel zone will appear as individual events on seismic data. Migration reduces the size of the Fresnel zone, thereby improving the lateral resolution to about ¼ of the wavelength. Differences in migration of 2D and 3D seismic data are visualized in figure 3-6.

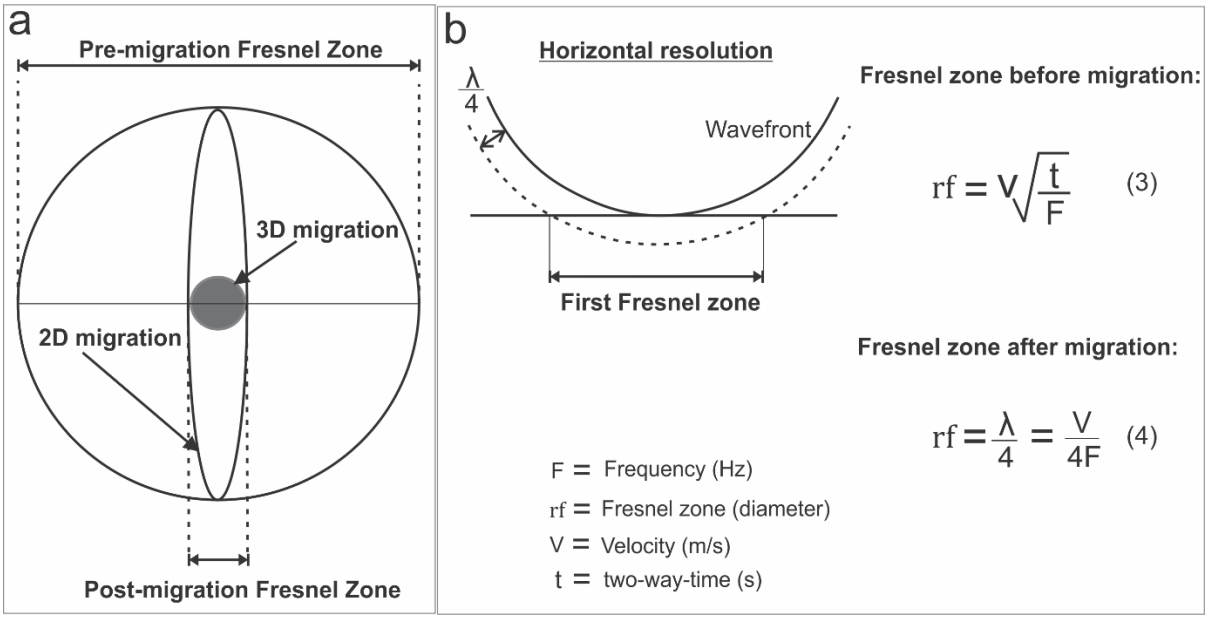

Figure 3-6: (a) The focusing effect of migration in 2D and 3D. The elliptic shape represents the optimal theoretical migration of 2D seismic data, whereas 3D migration collapses the Fresnel Zone to a small circle (modified from Brown, 1999). (b) The first Fresnel zone: the first energy to reach the receiver from a plane reflector is from the point where the reflector is first tangent to the wavefront. The area of the reflector that produces the reflection is limited by the area that the wavefront ¼ wavelength later makes with the reflector (Andreassen *et al.*, 2009). Equation 1 and 2 represent the magnitude of the Fresnel zone before and after migration, respectively (modified from Denham and Sheriff, 1981).

3.3.3 Resolution and interference

Interference is a phenomenon that occurs when the seismic response from closely spaced acoustic-impedance boundaries interfere with each other. Interference can be constructive or destructive as illustrated in figure 3-7. Constructive interference occur where two interfering waves have a displacement in the same direction, causing enhanced reflection amplitudes. Destructive interference is when the two interfering waves have a displacement in the opposite direction, and results in a suppression of the amplitude (Andreassen, 2009).

The top and base of a layer will be resolved as separate events if the time thickness of the layer is equal to or greater than ½ of the seismic wavelet. If the layer is thinner than 1/2 of the wavelength, the two opposite polarity reflections begin to overlap and interfere (figure 3-8). A layer thickness between ½ of the wavelength and down to ¼ of the wavelet, the will result in constructive interference and form a single wavelet of anomalously high amplitude. At ¼ of the wavelet maximum interference occur and this is called the tuning thickness. If a layer is thinner than the tuning thickness, the overlapping reflections will cause destructive interference and a decrease in amplitudes (Andreassen, 2009).

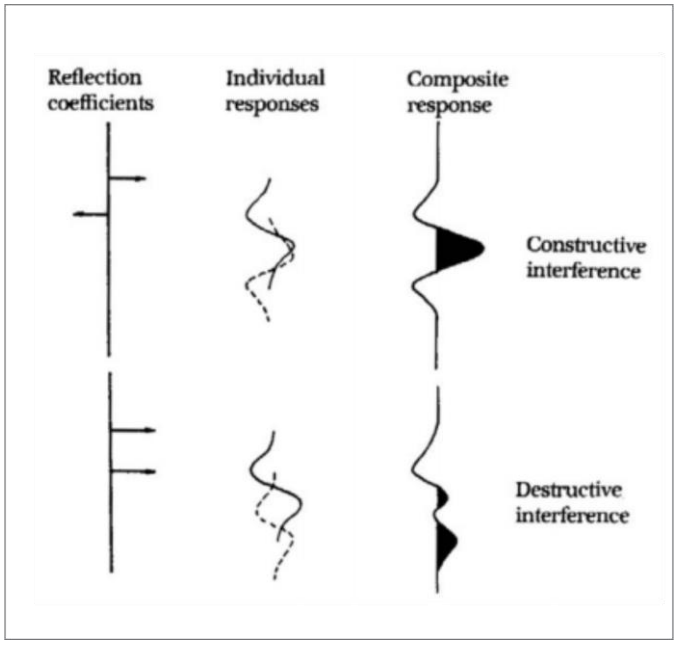

Figure 3-7: Illustrating how constructive and destructive interference affects a minimum-phase normal wavelet (figure from Andreassen, 2009).

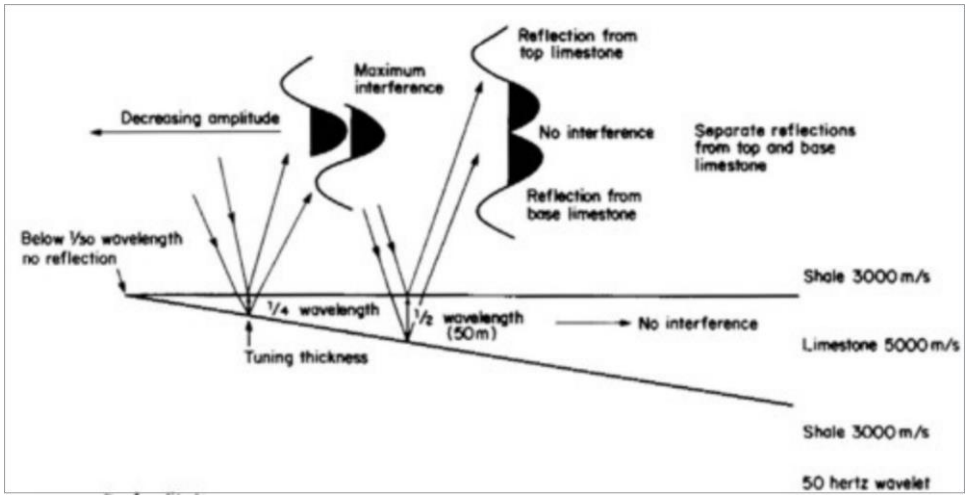

Figure 3-8: Interference effects associated with a high acoustic-impedance wedge encased in lower acoustic impedance shale (figure from Andreassen, 2009).

3.4 Petrel functionalities and tools

Interpretation, attribute analysis and visualization of the gas hydrate/free-gas system was carried out by using the seismic software platform Petrel 2013 developed by Schlumberger. This section is taken from Schlumberger (2011).

3.4.1 Interpretation of 3D seismic data

Horizon interpretation in Petrel provides several different mapping techniques, such as seeded 3D auto tracking, guided auto tracking and manual tracking.

Seeded 3D auto tracking is an efficient technique to perform on reflectors of good quality stretching over a large area. By defining the desired signal feature to peak or through, the points will be tracked outwards from the seedpoints in all directions. It follows extreme amplitude values along the reflector. Areas that deviate from the specified auto tracking parameters are left uninterpreted. If parameters are confined too strictly, it may result in areas that are left uninterpreted. On the contrary, if the selected parameters are too loose it may lead to "miss-picks".

Guided auto tracking follow the extreme amplitude values on a reflector between two points chosen by the interpreter. This type of tracking gives the user a greater control of the how the interpretation develops.

Manual tracking interpolate between the picked seed points chosen by the interpreter. It allows the interpreter to pursue tracking when the reflector appear discontinuous, disturbed or having too low amplitudes to fit the criteria of the auto tracking.

As the seafloor reflector serve as a prominent and continuous reflection in all surveys, horizon interpretation were performed by seeded 3D auto tracking. Mapping of the BSR horizons was carried out by using both guided auto tracking and manual tracking.

3.4.2 Volume attribute maps

Petrel exhibit a large attribute library, but only the attributes used in this paper will be described. Attributes may reveal geological features and relationships that might not be readily apparent in the raw seismic data.

Envelope, also known as reflection strength represents the total energy of the seismic trace. The attribute is phase-independent. High values of reflection strength may indicate gas accumulations or major lithological changes.

Instantaneous frequency is defined as the time derivative of instantaneous phase. The attribute is independent of amplitude and phase information, and represents the mean frequency of the spectrum. It can be useful to detect areas of variable seismic attenuation, as presence of free gas in pore spaces will cause a decrease of frequency.

3.4.3 Surface attribute maps

Surface attributes allows computation of interval attributes relative to a single horizon, between two horizons or within a constant time window.

RMS (root-mean-square) Amplitude calculates the square root of the sum of the squared amplitudes divided by the number of samples within a specified time window. RMS amplitude is often used to visualize hydrocarbon indications in seismic data as well as changes in lithology.

Extract value extract the input seismic value relative to a single horizon and allow the user to create surface attribute maps from seismic volumes created as volume attributes.

4. Results

Interpretations and observations are obtained from three datasets: Vestnesa.3D.2007 , Vestnesa.3D.2013 and Hydratech, and presented in separate sub-chapters. Interpretations are focused around the behavior of the BSR which represent the transition from hydrate bearing sediments to sediments containing free gas within its pore spaces. Striking features observed within the 3D data volumes will be described in relation to the BSR and the underlying free gas zone (FGZ). Seismic attributes are generated to extract information from the high-resolution 3D seismic datasets and to highlight features that are more difficult to detect directly from seismic reflection data.

All figures presented in this chapter are generated in time domain and include a north-arrow (green or black) for orientation purposes.

4.1 Vestnesa.3D.2007

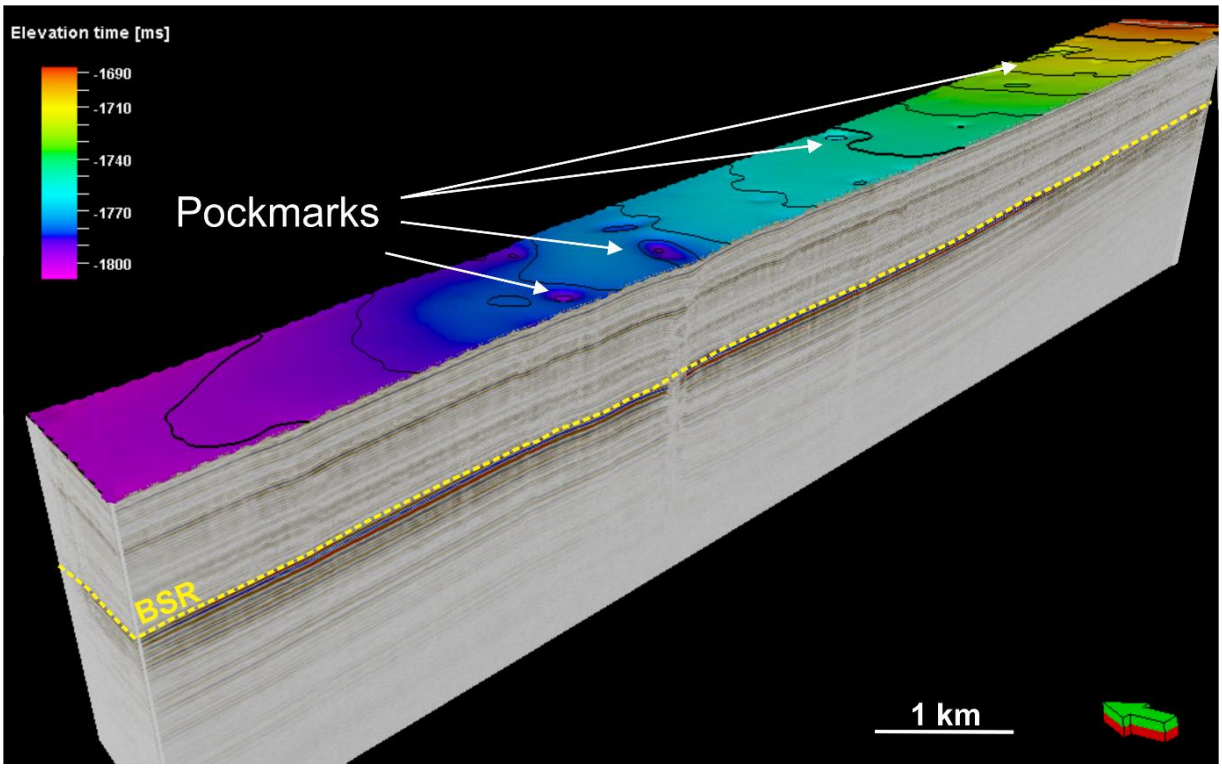

Figure 4-1: Overview of the 3D seismic data volume vestnesa.3D.2007. A time-structure map displays the topography of the seafloor. The BSR mimics the shape of the seafloor at ~200 ms (TWT) bsf. Several pockmarks of varying size are observed featuring the seafloor.

Vestnesa.3D.2007 dataset is located at the northern part of the Vestnesa Ridge, where the crest turns in westward direction, covering an area of ~ 27 km^2 (figure 1-4). The 3D seismic volume is oriented in a W-NW to SE direction, with a topography gently dipping ~ 1° from southeast towards western direction (figure 4-1). The seafloor is situated between 1200-1300 m of water depth (Petersen *et al.*, 2010). Several circular to elliptical shaped depressions of varying size appear as distinct features on the seafloor and are interpreted as pockmarks. Pockmarks on Vestnesa Ridge was first described by Vogt et al. (1994, 1999) and their formation is commonly linked to fluids escaping through the seabed (Judd and Hovland, 2007; Løseth *et al.*, 2009), indicating that Vestnesa Ridge represent an area of recent fluid flow activity.

4.1.1 Seismic character of the BSR

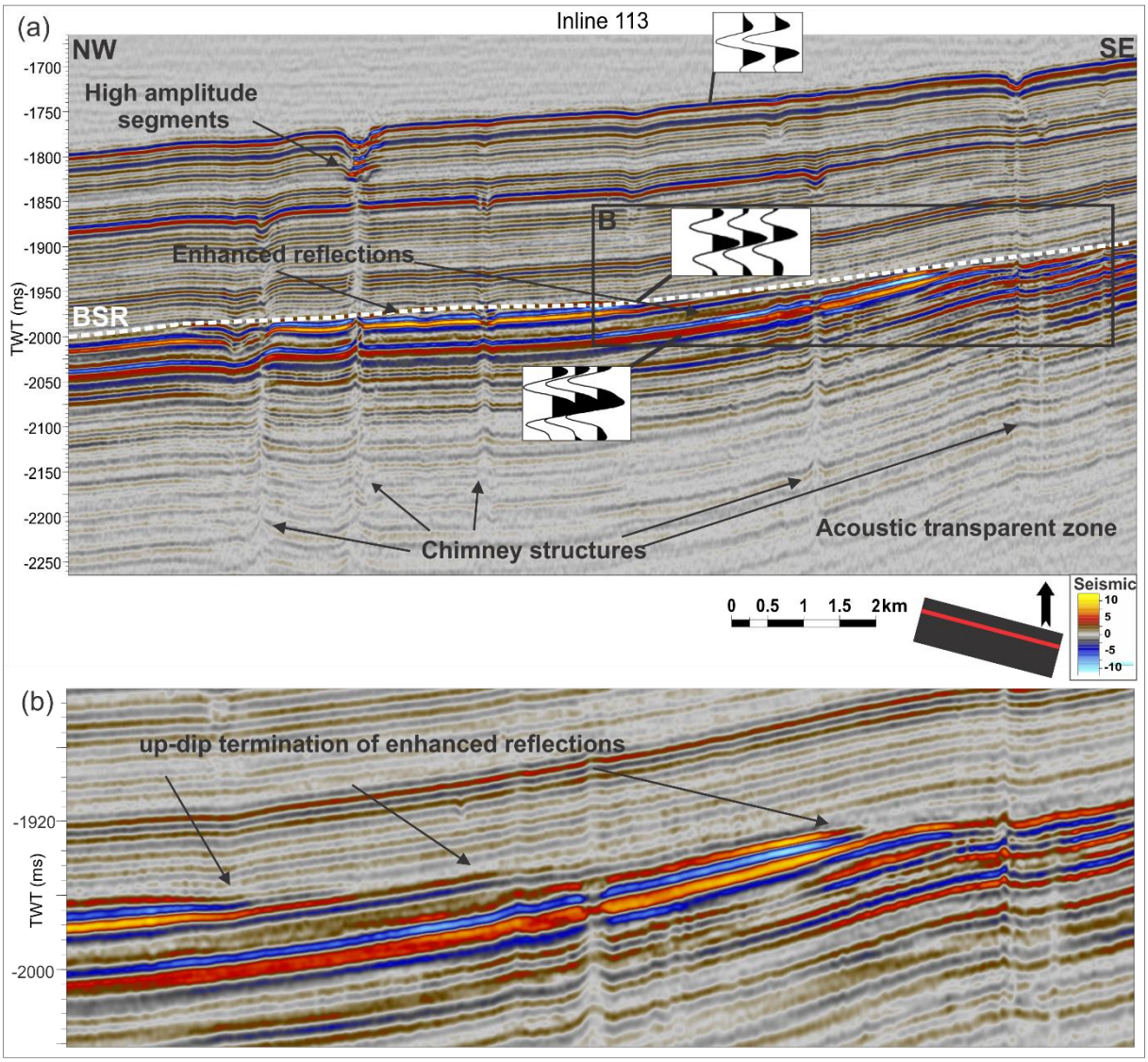

Figure 4-2: (a) A seismic profile of inline 113, visualizing the seismic characteristics typically associated with presence of gas hydrates: A BSR cross-cut sedimentary strata with reversed polarity compared to that of the seafloor as illustrated by the wiggle trace. Enhanced reflections and polarity reversal of a layer below the BSR is as well observed. Several acoustic chimney structures appear as striking features within the dataset. (b) A close-up of the BSRs cross-cutting behavior.

Throughout the 3D seismic volume, seismic reflections of high amplitude appear as a distinct feature embedded in well-stratified sediments (figure 4-1 and 4-2). It mimics the general morphology of the seafloor and by doing so, it cross-cut bedding-plane reflections at a relatively low angle. Such signature in seismic reflection data is interpreted to represent a bottom-simulating reflector (BSR), commonly used to infer the presence of gas hydrate in marine sediments (e.g. Shipley *et al.*, 1979; Yuan *et al.*, 1998; Petersen *et al.*, 2010; Bünz *et al.*, 2012). However, viewing the 3D dataset as a whole the BSR does not appear as a continuous reflector, but rather defined as the upper termination of separate high-amplitude reflections. The BSR are found at ~200 ms (TWT) below the seabed and coincides with the

theoretically predicted base of methane hydrate stability limit for this area (Vanneste *et al.*, 2005[b]). The observed high-amplitude BSR is thought to represent seismic response of the transition from hydrated sediments to free gas situated below, hereby marking the base of the hydrate stability zone (BGHSZ).

In inline direction the BSR's cross-cutting behavior is especially clear towards the southeastern part of the survey (figure 4-2 b), which also represent the topographical high. The cross-cutting signature makes the BSR readily apparent and show that the BSR does not represent a lithological boundary (Hornbach *et al.*, 2003). Other well-known BSR characteristics are as well observed; its polarity-reversed reflection pattern compared to the seafloor as illustrated by the wiggle trace in figure 4-2a, indicative of reduced seismic velocity across the interface. Moreover, enhanced reflections of high amplitudes are observed below the BSR. These seismic expressions are both indicators of free gas situated below the BGHSZ (Petersen *et al.*, 2010).

Amplitude values of the BSR are generally high compared to overlying strata, but varies laterally throughout the dataset. Another observation is that the BSR are not consistently the strongest reflection and reflections below the BSR are often observed with higher amplitude values (figure 4-2 b). A section of densely spaced thin layers define the strata above the BSR. These are, however, not represented in the same amount below the BSR, where reflections are fewer, thicker and of higher amplitudes.

4.1.2 Frequency distribution

To assist the interpretation of the BSR, instantaneous frequency attribute was generated for the 3D seismic volume to analyze attenuation of the seismic signal. Additionally, the frequency spectrum at different stratigraphic levels are generated to investigate the seismic signal and to display the frequency distribution in more detail.

Instantaneous frequency analysis reveal a noticeable decrease in dominant frequencies across the boundary of the BSR (figure 4-3). A ~100 ms (TWT) thick zone below the BSR is observed with the lowest frequencies. The zone of low frequencies follows the shape of the BSR, especially clear in the SE part where the BSR evolve into its cross-cutting behavior. The zone of reduced frequencies are observed to correlate with the BSR level and the enhanced reflections below (figure 4-2), indicating high attenuation of the seismic energy across this boundary. Enhanced reflections with low frequency content are often associated with accumulation of free gas (Taylor *et al.*, 2000). This particular zone are interpreted to represent the free gas zone (FGZ), where gas migrates and accumulates below the BGHSZ.

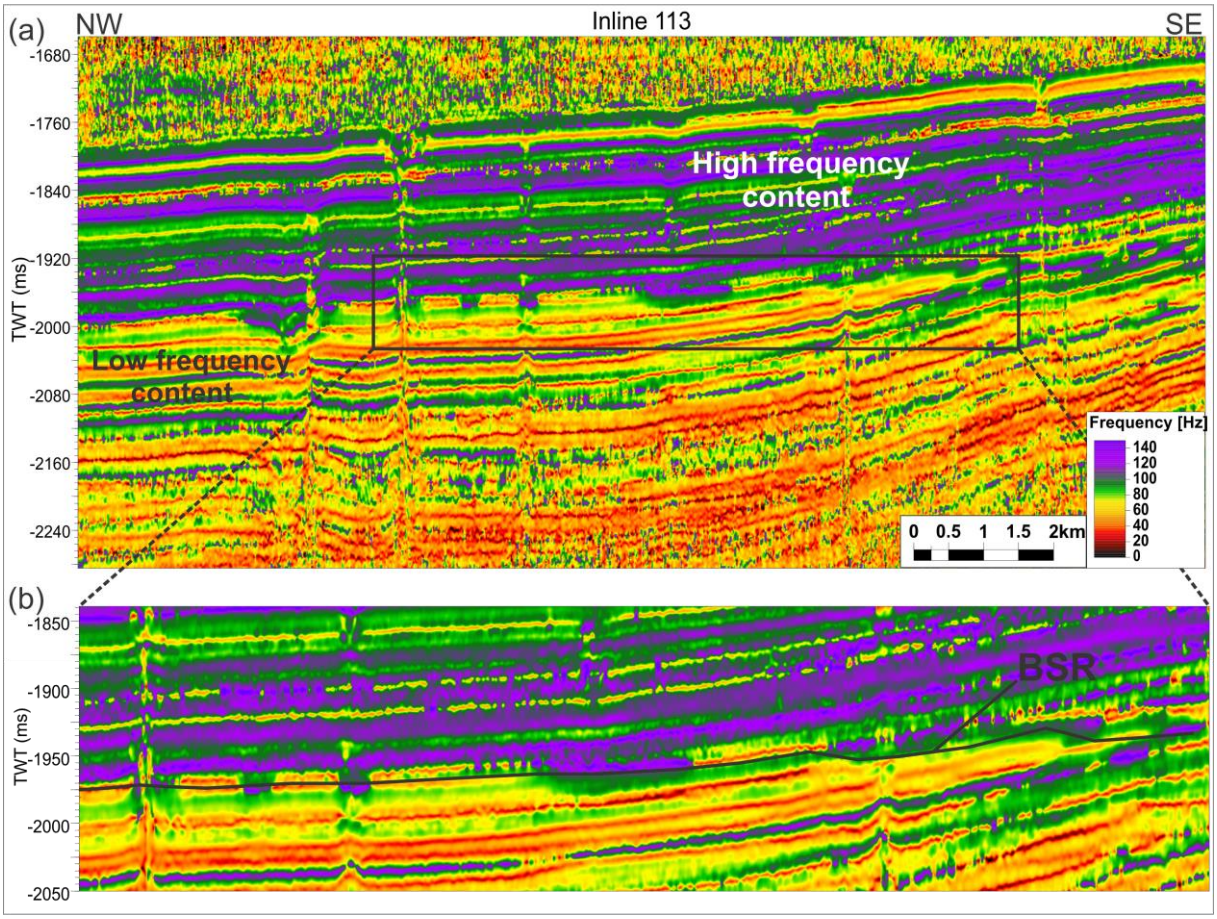

Figure 4-3: Instantaneous frequency section of inline 113 (same location as for figure 4-2). (a) A conspicuously drop in frequency is recognized below the BSR. Elevated frequencies are as well observed above the BSR, especially in the SE part of the profile. (b) Shows lateral variations in frequency-content along the BSR boundary. Black line indicate the interpreted BSR and visualizes where it shifts between layers due to its crosscutting behavior.

Attenuation of higher frequencies are as well observed along vertical paths below the previously described pockmarks. Additionally, lateral variations in frequency content occur along the boundary represented by the BSR. Patches of high frequency content are especially observed where the BSR truncates and shifts between high-amplitude reflections (figure 4-3 b).

Figure 4-4 displays a frequency spectrum tool-plot from the gas hydrate stability zone (GHSZ) (blue box) and below the BGHSZ (green box), within the free gas zone. This allows a comparison of frequency content from different areas of interest. The frequency spectrum uses a Fast Fourier transform to convert from time to frequency. A seismic section show locations of the defined zones from which the frequency spectrum tool is generated from (figure 4-4 a).

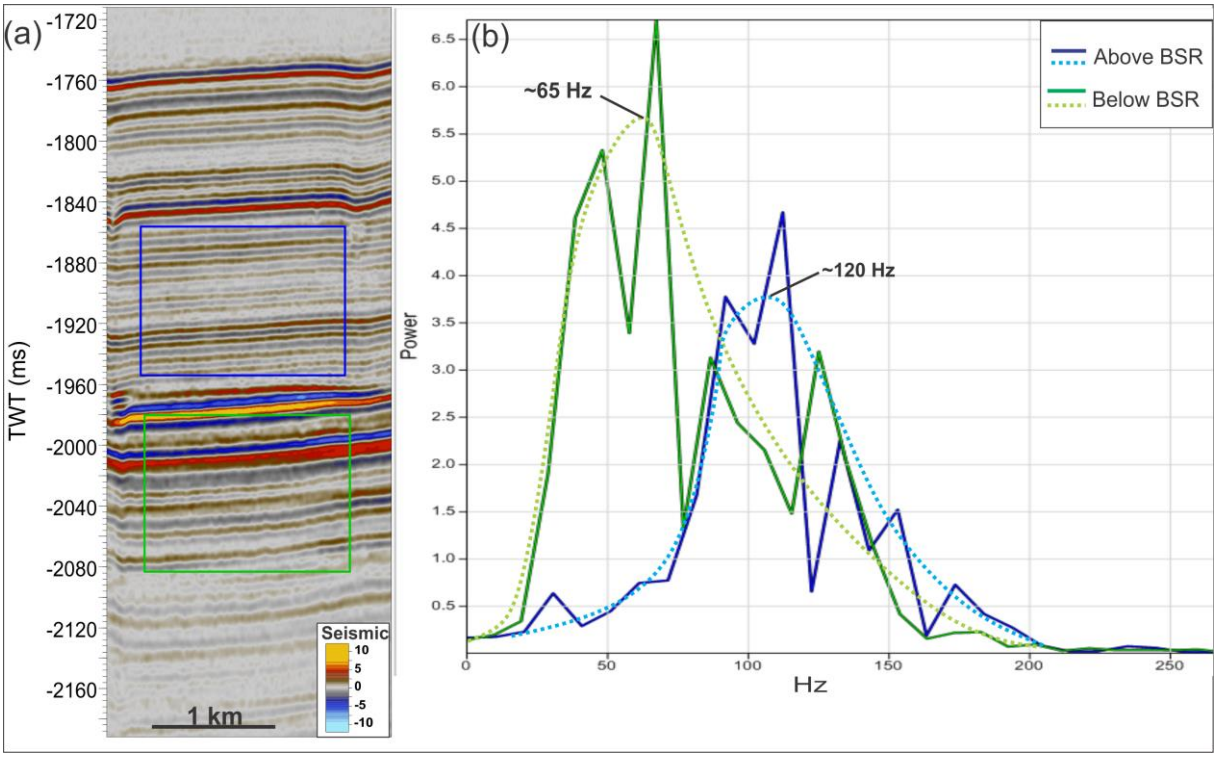

Figure 4-4: (a) A seismic section from inline 113. Boxes indicate areas of frequency analysis. Blue and green boxes indicate area above and below the BSR, respectively. (b) A 1D display of the acquired frequency spectrums. Frequency (Hz) distribution versus amplitude strength (Power). Dominant frequencies above and below BSR are ~120 and ~65 Hz, respectively.

Within the GHSZ, the dominant frequency show approximately 120 Hz (blue box) (figure 4-4 b). Dominant frequency below the BSR are ~ 65 Hz (green box), showing that frequency values is almost reduced by half when entering the free gas zone. Such frequency analysis were tested at several locations above and below the BSR throughout the seismic volume, where the dominant frequency below the BSR showed approximately half the values of the frequency values above the BSR. Hence, the frequency spectrum displayed in figure 4-4 are regarded as representative for the area. Such drastic reduction of frequency content are highly indicative of a zone acting as a low-pass filter on the seismic signals.

4.1.3 BSR appearance around chimneys

Columnar zones of seismic blanking distinctively pierce through the well-stratified sediments as well as the BSR (figure 4-2, 4-5). These near-vertical structures are seen to disturb the seismic image to even larger depths than 2100 ms (TWT). They are observed both to terminate within the subsurface strata and at the seafloor, where the latter coincides with pockmarks at the seafloor (figure 4-5).

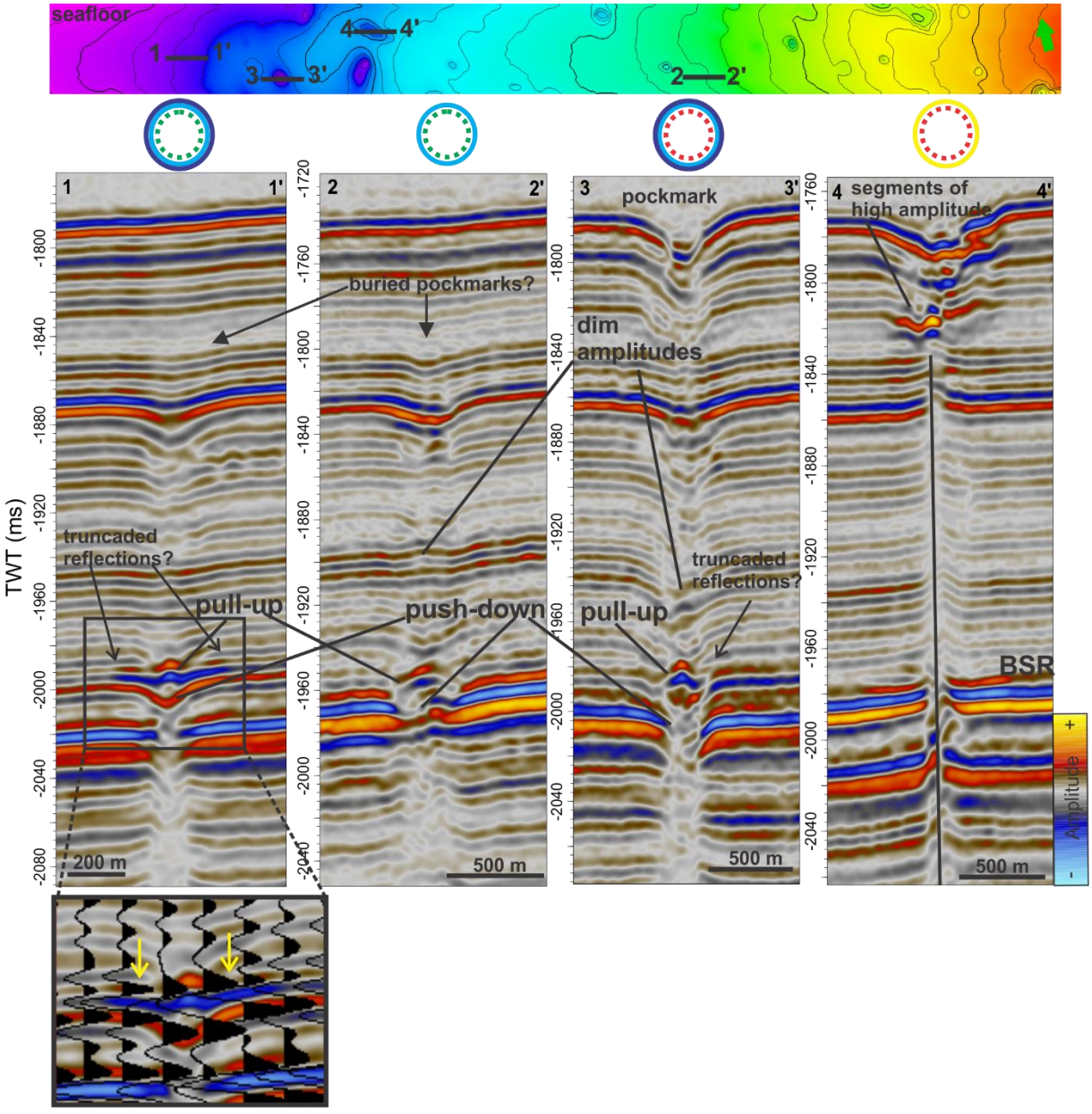

Figure 4-5: Displays the behavior of the BSR around different chimney structures present within the dataset. Time-structure map of the seafloor illustrate the location of the investigated chimneys. The different chimneys are denoted by colored circles indicating which category they are characterized by. For the color coded circles above each chimney, the reader is referred to figure 4-6. The inset show a wiggle trace of the observed truncated reflections, indicated by yellow arrows.

These acoustic vertical zones are interpreted as chimneys that relate to fluid flow through the subsurface (e.g. Bünz *et al.*, 2003; Cartwright *et al.*, 2007; Petersen *et al.*, 2010). They are commonly seen to coincide with pockmarks on the seafloor, representing vents for focused gas and/or fluid flow (Judd and Hovland, 2007; Hustoft *et al.*, 2009; Løseth *et al.*, 2009).

In near proximity to the chimneys, the BSR appear in general with a relatively high continuity and only loses its seafloor-mimicking character within the interior of chimneys. The BSR is in general seen to cross the chimneys, but the reflection is often represented by a pull-up effect (figure 4-5). Where faults and fractures occur at BSR level, reflections deflect upwards against a narrow wipe-out zone. Numerous chimney structures are observed throughout the study area and investigated to see if there exist any similarities due to BSR behavior and the general seismic characterization. The observed structures are categorized into 3 types based on their similar seismic expressions (figure 4-6). Within these 3 types, a main division is done by chimneys terminating at seafloor represented by pockmarks (red dotted circle) and those terminating at stratigraphic levels below the seafloor (green dotted circle) (figure 4-6).

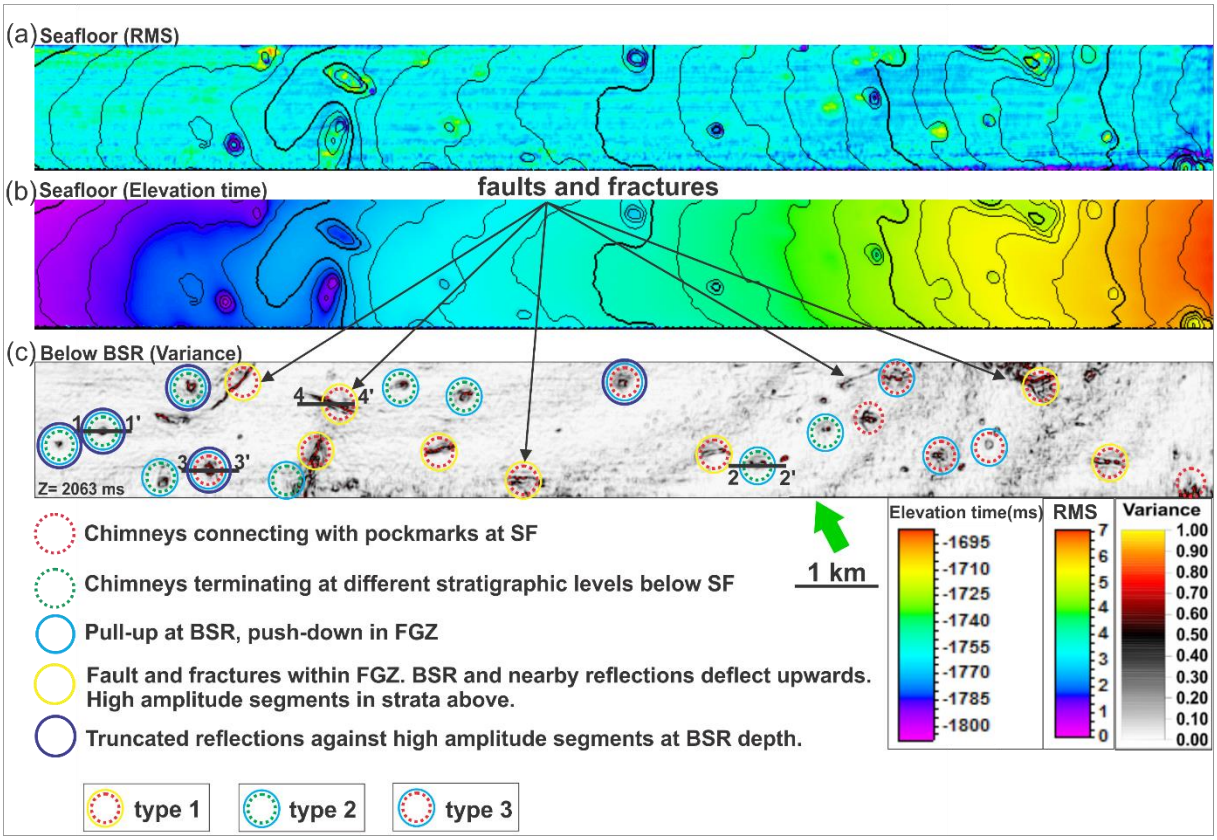

Figure 4-6: (a) Seafloor expressed in root-means-square (RMS) amplitude map, where the search window covers the seafloor (SF) reflection. Bright amplitudes are shown in warm colors. (b) Time-structure map of the seafloor. Contour lines forming circles show locations of pockmarks. (c) Variance time-slice at depth 2063 ms (TWT) (below BSR). High variance values indicate strong lateral amplitude discontinuities and are seen to form both elongated structures and circular anomalies.

Type 1: Variance maps displays the occurrence of strong lateral amplitude discontinuities. Elongated structures are interpreted to represent faults and fractures, where fractures represent the smallest lineations (figure 4-6 c). These structures are as well identified in seismic profiles by cutting reflections through the FGZ, BSR and larger faults stretches even further into the GHSZ. The BSR appear with continuity and high amplitude values close to the faulting zone (figure 4-5; chimney 4). The seismic image within the FGZ and BSR are dominated by a narrow wipe-out zone where adjacent reflections deflect upwards against the near-vertical zone. Such up-bending of seismic reflections are as well dominating in the GHSZ, except where high amplitude segments are observed in overlying strata. Another observation is that all the chimneys evolving from fault structures crop out at pockmarks on the seafloor. RMS amplitude map shows that these seafloor depressions are characterized by both high and low amplitude values (figure 4-6 a). It is difficult to recognize possible push-down effects within the FGZ, as they show more of a sharp up-bending pattern (figure 4-5: chimney 4). Minor down-bending effects within the FGZ are however observed at some locations, but hard to discriminate if these are just the result of the faulting pattern.

Type 2: Represents chimneys that terminate at depths below the seafloor. From the variance map they are detected by a circular pattern of high variance values. Even if no seafloor depressions are observed above these chimneys, some are associated with a circular pattern of higher amplitude values on RMS amplitude map (figure 4-6). Within the FGZ, the enhanced reflections vary from being traceable with dimmed amplitudes to be largely degraded by masking effects. The BSR is expressed by a pull-up effect, and push-down effects are observed within the FGZ. Some chimneys are observed with a high amplitude segment at BSR depth (figure 4-5; chimney 1 and 3), where particular reflections appear to truncate against this amplitude anomaly (figure 4-5; wiggle trace). In figure 4-6, these chimneys are marked with a dark blue circle in addition to the color-code for type 2 chimneys. Within the GHSZ reflections are characterized by dimmed amplitudes and are dominated by a down- or up-bending effect with respect to the surroundings.

Type 3: Represents chimneys that terminate at seafloor where they coincide with pockmarks. They show similar seismic expressions as type 2, but with a higher degree of acoustic disturbance (figure 4-5; chimney 3). From the RMS amplitude map these are observed with both high and low amplitude values within pockmarks (figure 4-6 a). Chimneys that have truncated reflections against a high amplitude segment at the depth of the BSR are marked with a dark blue circle (figure 4-5; chimney 3).

4.1.4 Seismic characterization of the free gas zone (FGZ)

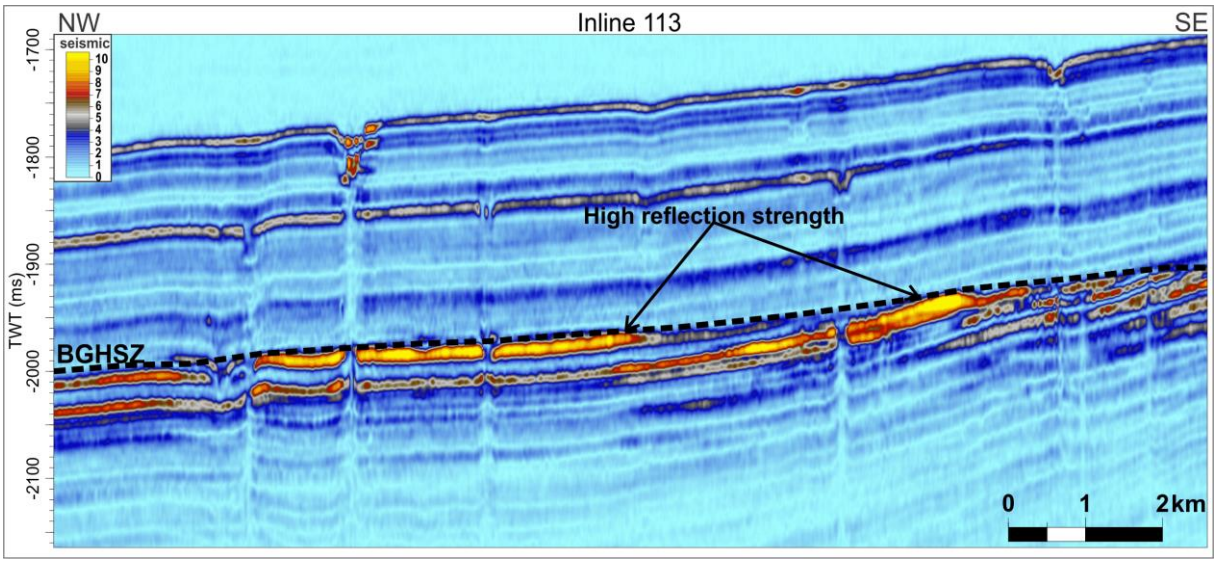

Figure 4-7: Reflection strength section for inline 113 with same location as figure 4-2. High and low amplitude values are displayed in warm and cold colors, respectively. Loss of amplitude are seen just above the BSR and below enhanced reflections. Enhanced reflections show increased reflection strength towards the BSR boundary.

The free gas zone (FGZ) is defined as the zone directly beneath the base of the gas hydrate stability zone (BGHSZ) where migrating gas may accumulate due to permeability barriers from hydrate-bearing sediments above. The dynamic and evolution the FGZ are not well constrained (Plaza-Faverola *et al.*, 2012) and lack a systematic description (Hornbach *et al.*, 2004).

The reflection strength attribute of inline 113 shows the enhanced reflections below the BSR and their terminating behavior towards the BGHSZ (figure 4-7). Estimations of subsurface sediment velocities was acquired from Ocean bottom seismometer (OBS) (Petersen *et al.*, 2010) and showed an abrupt velocity decrease from 1800 m/s above the BSR to a 7 m thick zone of 1250 m/s, followed by a 15 m thick layer holding 1400 m/s. Such low-velocity layers strongly suggest the occurrence of free gas situated below the BSR. Even low concentrations would cause a drastic reduction in compressional wave velocity and hence cause a strong decrease in acoustic impedance (Domenico, 1976). Throughout the dataset, the zone of enhanced reflections has a varying thickness of up to ~100 ms (TWT).

Lateral variations in reflection strength are seen to vary from low to high and reflections that crosscut overlying strata is observed to hold the highest values (figure 4-7). Viewed separately, the enhanced reflections show increased reflection strength towards the BSR boundary. The highest amplitude values in the uppermost reflector are observed to overlie lower amplitude values at the reflector below. Similarly, where the upper high-amplitude reflector fades out towards the BGHSZ, the reflector beneath start showing increased values (figure 4-7).

Two sub-volumes of the seismic dataset are used to further investigate amplitude variations along the enhanced reflections (figure 4-8 and 4-9). RMS amplitude maps are generated by using a time window that encloses the particular horizon of interest. The enhanced reflections within the FGZ show a general trend of increased amplitude values towards the BSR boundary (figure 4-8, 4-9), which correlate with observations from the reflection strength attribute (figure 4-7). Horizons R2 (figure 4-8) and H1 (figure 4-9) could be traced all the way from the FGZ and into the GHSZ. They show high amplitude anomalies when in the FGZ and an abrupt loss of amplitude values when entering the GHSZ. The selected horizons follow the up-dipping trend of the overlying strata. As the SE region represent a topographic high, gas would preferably migrate towards elevated areas. The abrupt loss of high amplitude values may indicate that the physical properties within layers are chanced across the boundary represented by the BSR. Such observations indicate that gas hydrates act as a barrier for fluid migration and prevent further migration along these stratigraphic horizons.

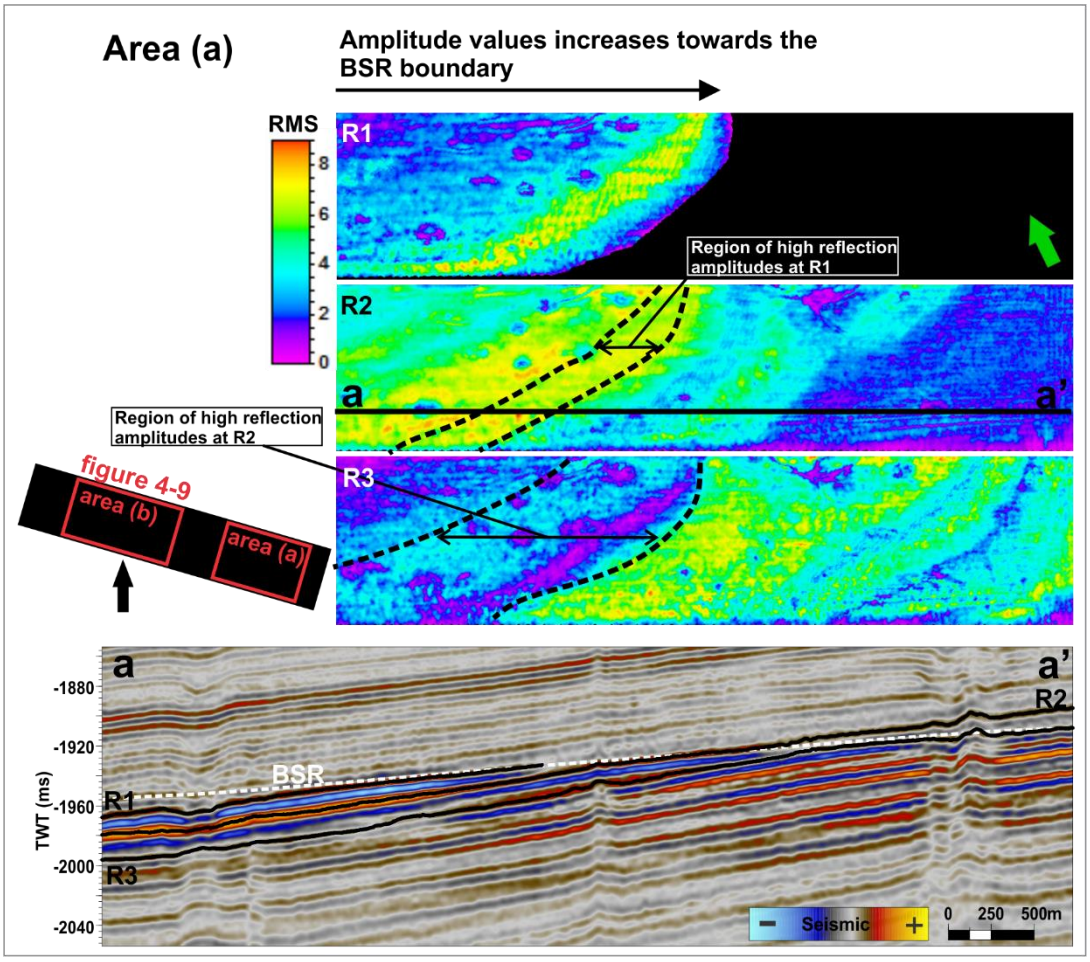

Figure 4-8: Seismic section displays the interpreted horizons (R1, R2, and R3) in relation to the cross-cutting BSR. RMS amplitude maps are generated from a time-window that encloses each horizon. Each horizon show increased amplitude values towards the BSR boundary. Horizon R2 can be traced into the GHSZ, which represent the region lowest amplitude values. Black stippled area at RMS maps represents the region of high reflection amplitudes of the overlying horizon.

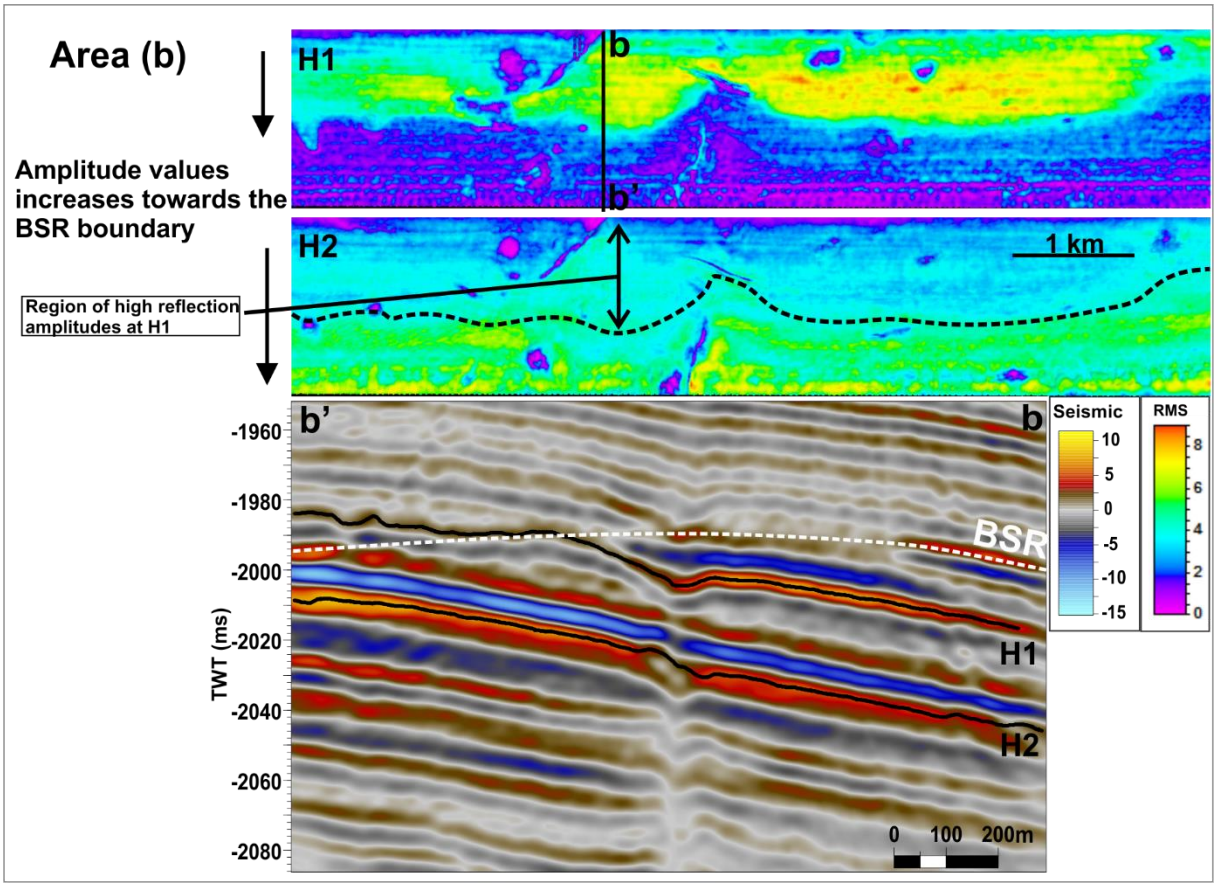

Figure 4-9: Seismic section displaying the interpreted horizons (H1, H2) in relation to the cross-cutting BSR. RMS amplitude maps generated from a timewidow that encloses each horizon. Low amplitudes values are observed at locations of chimneys (circular pattern) and in relation to fault-related structures. Black stippled area at RMS maps represents the region of high reflection amplitudes of the overlying horizon.

Striking observations are the lateral amplitude anomalies forming a conspicuously pattern along these horizons. From figure 4-8, horizon R3 are observed with lower amplitude values where the overlying horizon R2 exhibit the highest amplitude values. The same pattern is observed for horizons at area (b) (figure 4-9). However, horizon R1 within area (a) does not seem to affect the underlying horizon R2 and deviate from the amplitude pattern observed elsewhere. As mentioned earlier gas tend to migrate to topographic highs which could explain why each horizon hold the highest amplitude values at the shallowest part. However, there could be several reasons for the observed amplitude pattern. For instant, reflection amplitude can be affected by the tuning thickness of layers, which can produce both negative and positive interference (Widess, 1973). The different reasons that could explain such peculiar amplitude pattern will be viewed more closely in the discussion chapter (Ch. 5.6).

4.2 Vestnesa.3D.2013

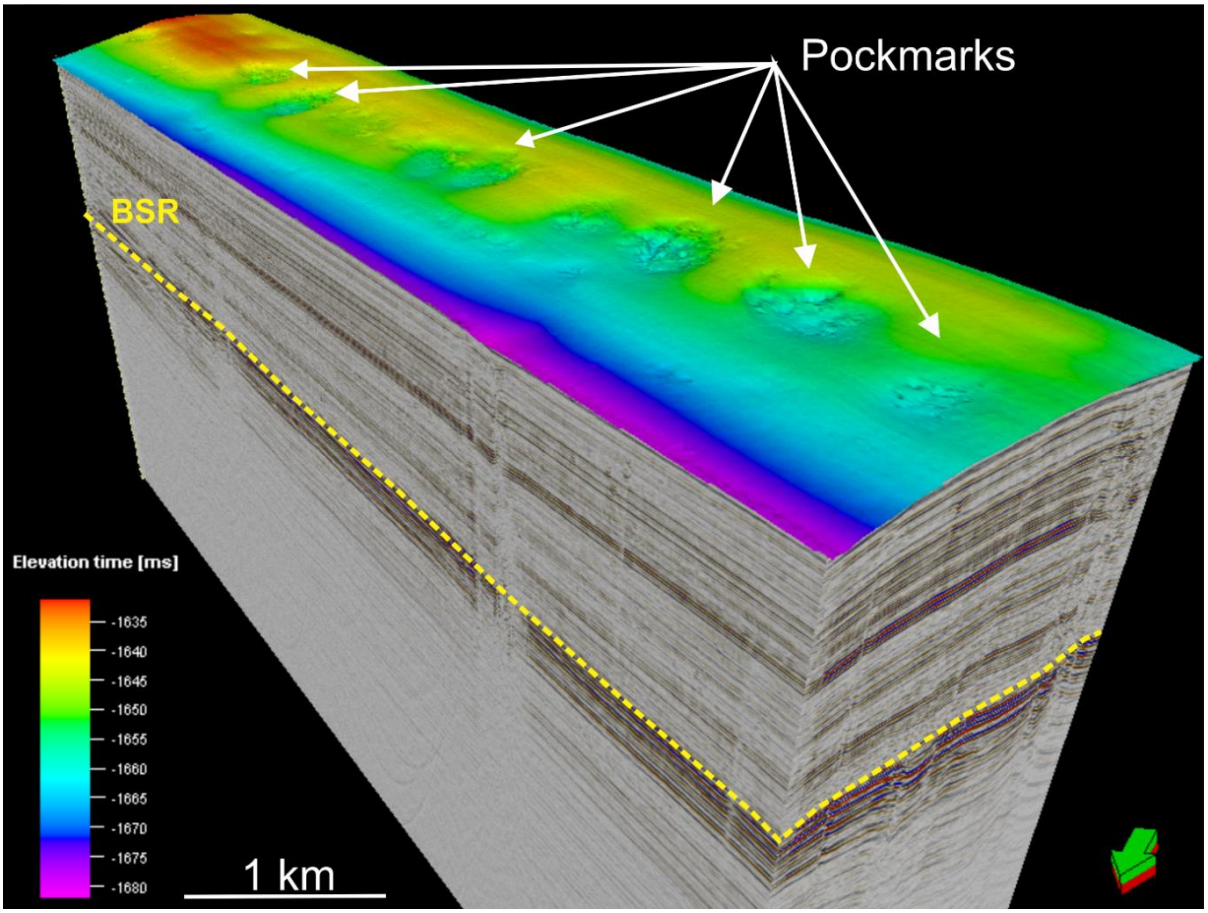

Figure 4-10: Overview of the 3D seismic data volume vestnesa.3D.2013. A time-structure map displays the topography of the seafloor. The BSR is located at ~200-250 ms (TWT) bsf. The morphology of the seafloor is characterized by several distinct pockmarks situated along the crest axis. They show a more pronounced and rough appearance than what is observed for pockmarks at the western end of Vestnesa Ridge (figure4-1).

The dataset Vestnesa.3D.2013 is situated on the eastern segment of Vestnesa ridge and covers an area of ~ 12 km^2. The 3D seismic volume is orientated in SE-NW direction and its location relative to Vestnesa.3D.2007 can be viewed in figure 1-4. The seafloor surface is marked by several pockmarks of various sizes that align along the crest axis and measures up to 700 m in diameter and depths up to 10 m (Bünz *et al.*, 2012) (figure 4-10). During cruises with R/V Helmer Hanssen in 2010 and 2012, single-beam echo sounding system detected acoustic flares rising from the seafloor, indicating gas bubbles emanating from the seafloor and into the water column. These flare occurrences were seen to coincide with pockmarks on the seafloor, hence evidential of an area of active fluid flow (Bünz *et al.*, 2012; Smith *et al.*, 2014). Pockmarks observed at the western segment of Vestnesa Ridge (figure 4-1) are of more variable size and have a smoother morphology. Moreover, they are not restricted to the crest axis, but rather appear with a more scattered distribution. Here, pockmarks are distributed in a distinct pattern along the crest and exhibit more rough and similar morphology (Bünz *et al.*, 2012).

4.2.1 Seismic character of the BSR

The seismic reflection data reveal a prominent and widespread BSR situated between ~200-250 ms (TWT) bsf. The high-amplitude BSR is characterized by reversed polarity relative to the seafloor reflection and with enhanced amplitude anomalies situated below (figure 4-11). The BSR covers the whole study area, but its appearance is quite irregular and vigorously disrupted by acoustical transparent zones that pierce through the stratigraphy. Seismically disturbed wipe-out zones stretch from depths below the BSR, up through the stratigraphy until they terminate at the seafloor. These acoustic features are interpreted as chimneys, representing pathways of focused fluid-flow (Bünz *et al.*, 2012) and are observed to connect with the previously described pockmarks. These chimney structures highly impacts the seismic characteristic and distribution of the BSR, which only mimics the seafloor topography in few places.

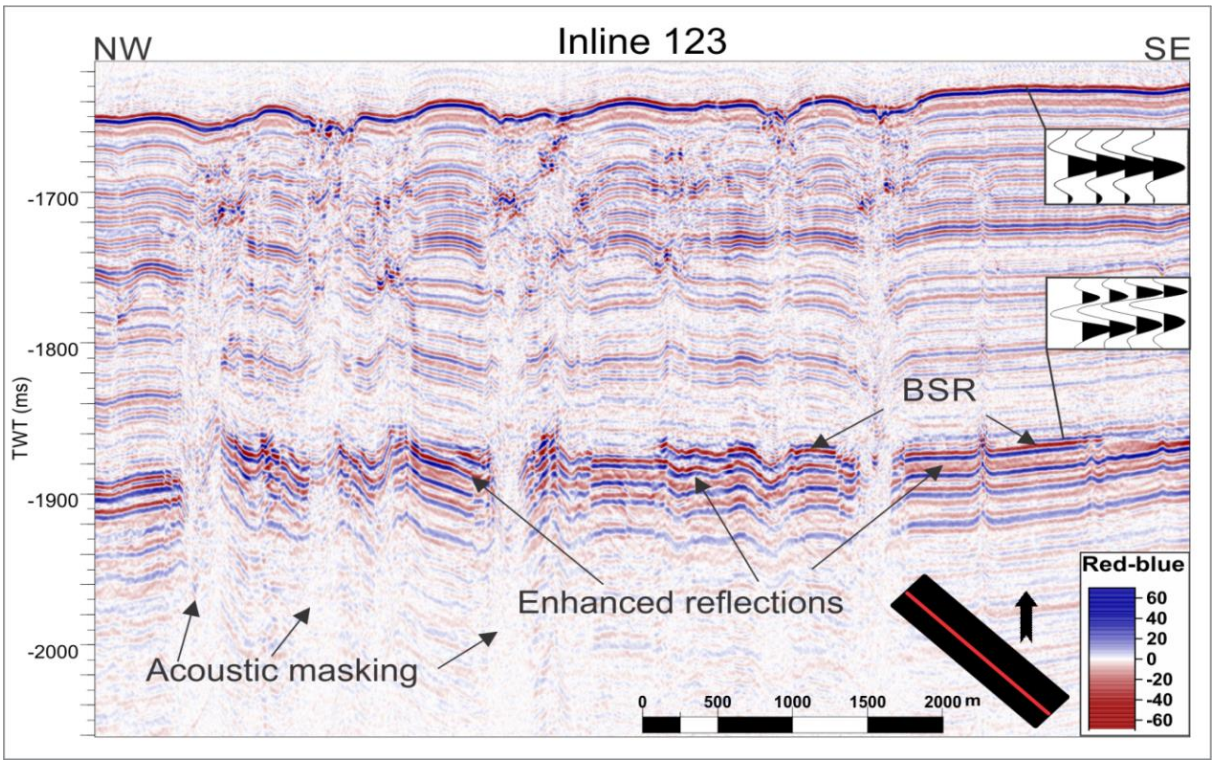

Figure 4-11: The BSR appears as a distinct amplitude anomaly throughout the seismic section except where chimney structures pierce through sedimentary strata. They are seen terminating at the seafloor, leaving the seafloor with a rough morphology. These semi-vertical chimneys represent columnar zones of acoustic masking. The BSR have a reversed polarity to that of the seafloor.

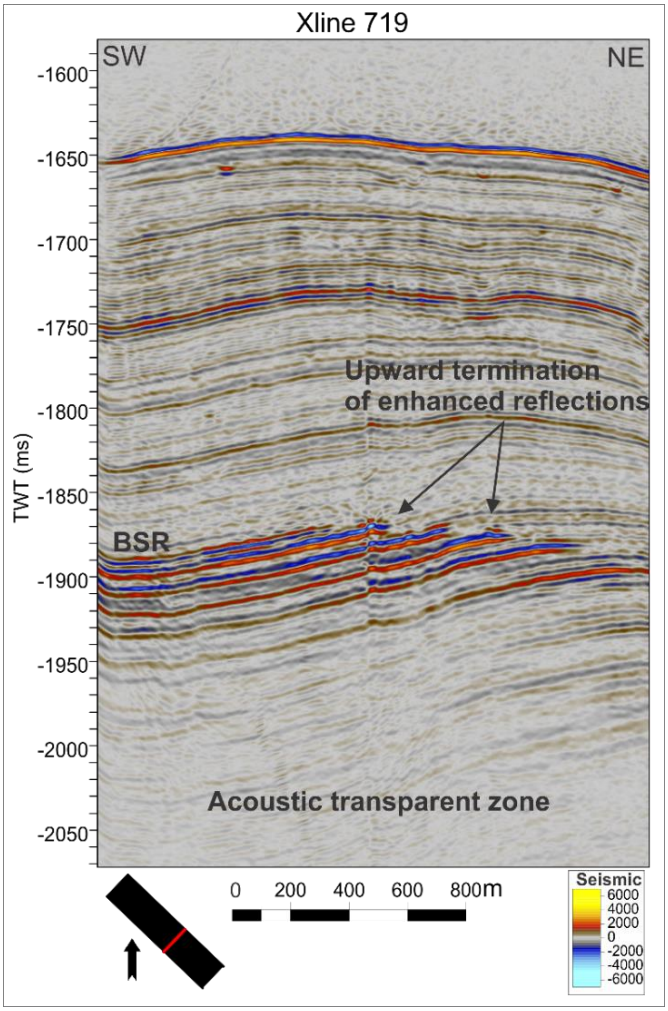

Figure 4-12: Seismic profile of cross line 719. The BSR is readily apparent where it cross-cuts bedding plane reflections.

The BSR is readily distinguishable in the cross-line direction where it cross-cuts sedimentary strata below the crest of the ridge (figure 4-12). The BSR is represented by an envelope of enhanced reflections that terminate against the dominant strata as it follows the anticlinal shape of the seafloor. Enhanced reflections of high amplitude values below the BSR indicate presence of free gas within the FGZ. The observed acoustic transparency below enhanced reflections are attributed to absorption and attenuation of the seismic energy due to gas-charged sediments (Hustoft *et al.*, 2007).

4.2.2 Frequency distribution

The instantaneous frequency attribute displays a marked reduction of frequency content below the BSR as well as high frequencies of overlying strata (figure 4-13). Distribution of the lowermost frequencies relate to the enhanced reflections (figure 4-11) and appear as a somewhat continuous zone below the BSR. However, chimneys are observed to cause vertical disturbance from the FGZ to the seafloor, holding preferably low frequencies. The rapid reduction of frequencies suggest high attenuation across the boundary, indicative of free gas accumulations below the BGHSZ (Taylor *et al.*, 2000). Cross-line 719 is taken from an area of no chimney occurrence and the low-frequency zone is observed to follow the shape of the BSR (figure 4-13 b). Patches of high frequency content is observed where the BSR truncates against dominant strata and shifts between reflectors, suggesting lateral variations in frequency content across this boundary. The frequency tool-plot show a drop of high-frequency components across the BSR (figure 4-14). Analysis obtained from a sub-section of inline 123 reveal a loss in dominant frequencies from ~145 Hz (blue box) within the GHSZ to ~80 Hz (green box) at the FGZ.

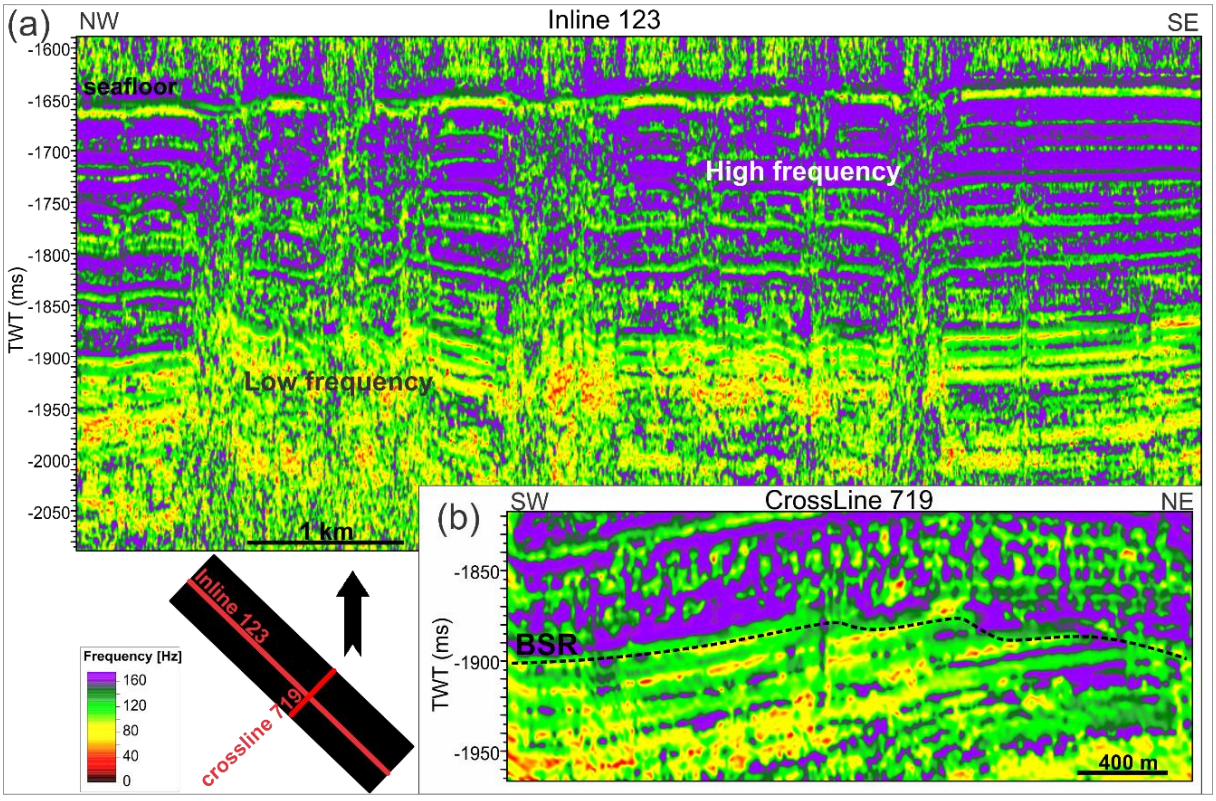

Figure 4-13: (a) Instantaneous frequency profile from inline 123, displays attenuation of frequency content across the BSR. The region between the seafloor and BSR exhibit the highest frequencies, whereas a low frequency zone is observed beneath the BSR. (b) A zoomed-in instantaneous frequency profile of cross-line 719. Black stippled line indicate the interpreted BSR and visualizes where it shifts between layers due to its crosscutting behavior.

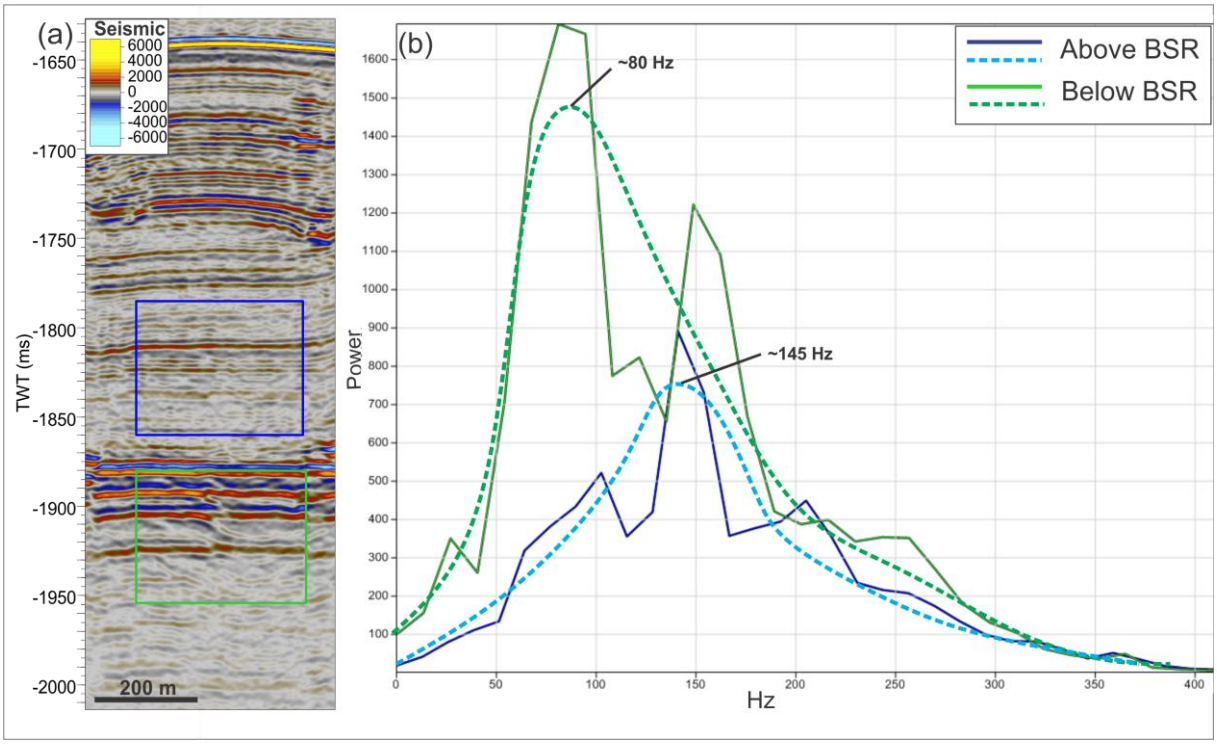

Figure 4-14: (a) A seismic section from inline 123. Boxes indicate areas of frequency analysis. Blue and green boxes indicate area above and below the BSR, respectively. (b) A 1D display of the acquired frequency spectrums. Frequency (Hz) distribution versus amplitude strength. Dominant frequencies above and below BSR are ~145 and ~80 Hz, respectively.

4.2.3 BSR appearance around chimneys

Chimneys on western and eastern segment of Vestnesa Ridge show remarkable differences in the seismic data. In contrast to the near-vertical geometry of the chimneys on the western segment, these chimneys are associated with a broader and more crocked geometry. Moreover, chimneys on the eastern segment represent more degraded zones and show little preservation of reflection continuity within its interior (figure 4-15 and 4-16). Their rooting-zones are hard to detect as the seismic is largely disturbed. However, they are seen to feature the seismic to depths below the enhanced reflections. The true depth extent of the chimneys can be difficult to establish, because strong attenuation in the upper part of the chimney produces an acoustic shadow zone beneath (Westbrook *et al.*, 2008b). Seismic reflections are mostly distorted and of low reflection amplitude. Both up- and down-bending effects characterize its semi-vertical path towards the seafloor. High-amplitude segments are observed within shallow strata, overlying almost completely masked seismic reflections (figure 4-15 and 4-16). Such seismic characteristics strongly support the occurrence of gas leakage through these semi-vertical chimneys and seafloor, as detected hydro-acoustically by Bünz et al. (2012) and Smith et al. (2014). From variance map faults and fractures appear with a curvilinear and interconnected pattern, and show close relation to the distribution of chimneys (figure 4-15 a) (Plaza-Faverola *et al.*, 2015).

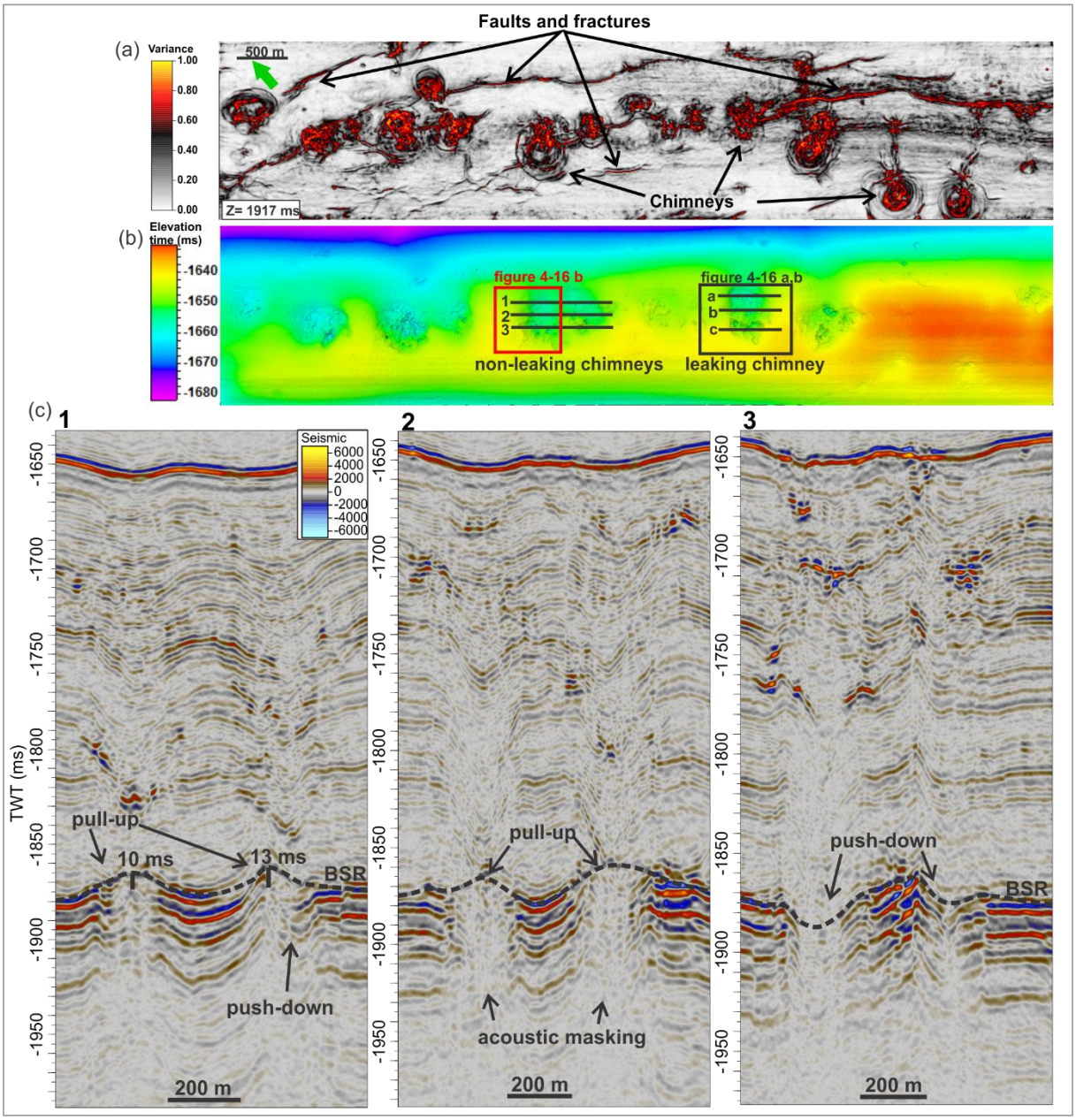

Figure 4-15: (a) Variance time-slice at depth 1917 ms (TWT) (below BSR). (b) Time-structure map of the seafloor, displaying pockmarks and location of the investigated non-leaking and leaking chimney. (c) Seismic sections taken successively through the non-leaking chimney. For detailed view of seepage locations along the crest, the reader is referred to Smith et al. (2014).

In general, the BSR and underlying enhanced reflections are not traceable within the chimneys interior and the original stratification is wiped out. However, the surrounding reflections tend to deflect up or down towards the columnar acoustic wipe-out zone. In spite of this, the BSR is traceable at the border of the chimneys, but recognized as either a pull-up of push-down effect (figure 4-15 c and 4-16 a). Both chimneys show pull-up effect at the onset of chimneys, and push-down effect towards the end. For clarification, the onsets of chimneys are here taken to represent the first seismic section from each chimney (indicated by; 1 in fig-4-15 and *a* in fig-16), and as follows, the ending of chimney by the last seismic section (indicated by; 3 and c).

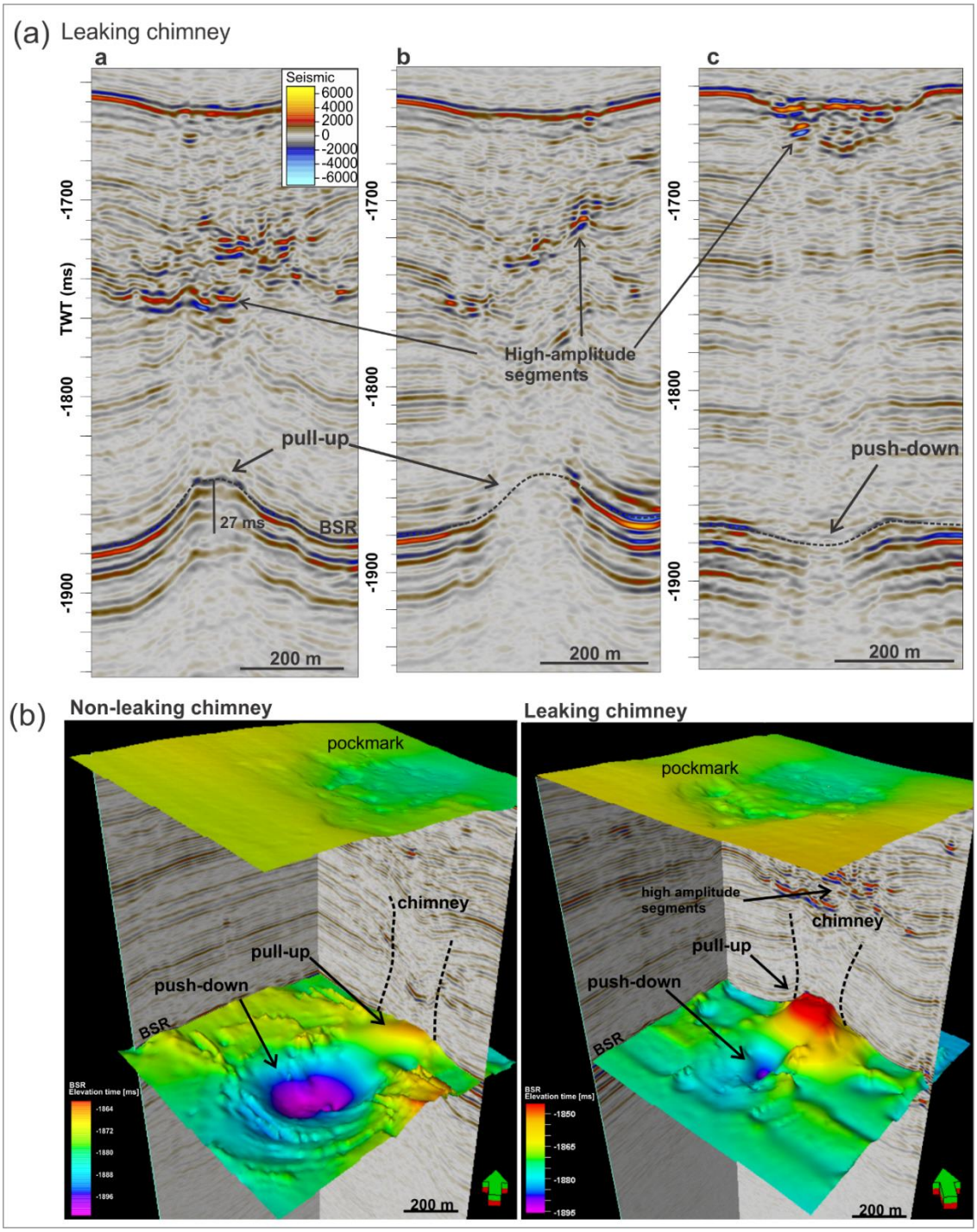

Figure 4-16: (a) Seismic sections taken successively through the leaking chimney. Location as indicated in figure 4-15 b. (b) 3D-view of cropped volumes enclosing the non-leaking chimney and leaking chimney, respectively. The figure show time-structure maps of the seafloor and associated pockmark, as well as the BSR surface at chimney locations. Showing the different BSR appearance between a non-leaking chimney and a leaking chimney.

Bünz et al. (2012) reported that pull-up features were completely absent at the eastern segment of Vestnesa Ridge, which by this research is suggested to be incorrect. To examine the nature of the observed pull-up/push-down effects, the BSR is mapped out from a non-leaking chimney and a leaking chimney (figure 4-16 b).

Non-leaking chimney: At the onset of the chimney the BSR is represented by a pull-up effect, whereas push-down features are observed within the FGZ (figure 4-15, 4-16 b). Occurrence of high-amplitude segments is not observed forming any particular pattern, but rather appear with a more scattered distribution between the seafloor and the BSR. At the end of the chimney, the BSR is represented by a push-down effect of significant magnitude compared to the leaking-chimney. Here, high-amplitude segments appear brighter and of higher amplitude compared to the onset of the chimney. The seafloor pockmark is of smooth morphology and characterized by low RMS-amplitude values (figure 4-17).

Leaking chimney: At the onset of the chimney the BSR and underlying enhanced reflections are represented by a pull-up effect. As visualized in figure 4-16, the pull-up feature is of significant magnitude compared to the non-leaking chimney in figure 4-15c. Another observation is the significant concentration of shallower high-amplitude segments overlying the BSR pull-up feature. At the end of the chimney, the BSR is represented by a push-down effect and high-amplitude segments are not observed at the same stratigraphic region. Here, high-amplitude segments are rather observed accumulating close to the seafloor. The region of push-down at BSR level is observed to coincide with rough morphology at the seafloor (figure 4-15 and 4-17). From the RMS amplitude map, this particular area is as well observed with a cluster of higher amplitude values (figure 4-17). These observations may indicate local variations within the wide chimney structures and are further discussed in chapter 5.3.2.

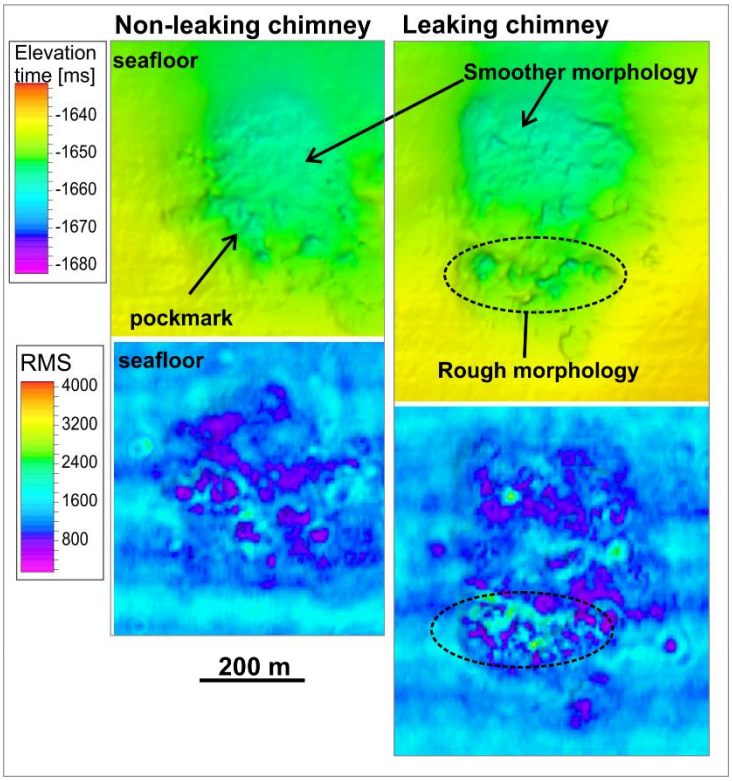

Figure 4-17: Time-structure map of non-leaking and leaking chimney, displaying the morphology within the respective pockmarks. RMS amplitude map of the seafloor pockmarks, where the search window encloses the seafloor reflection. The area of rough morphology (leaking pockmark) are observed to hold a cluster of higher amplitude values.

4.2.4 Seismic characterization of the free gas zone (FGZ)

The FGZ of the eastern segment of Vestnesa Ridge is largely disrupted by the close intervals of the wide and chaotic acoustic character of chimneys. Investigating lateral amplitude distribution along enhanced reflections within the FGZ proved difficult due to largely disturbed seismic and consequently low reflection-continuity over a satisfying area. Hereby, amplitude investigation as carried out for Vestnesa.3D.2007 (figure 4-8, 4-9) and Hydratech (figure 4-25) is not conducted for this dataset.

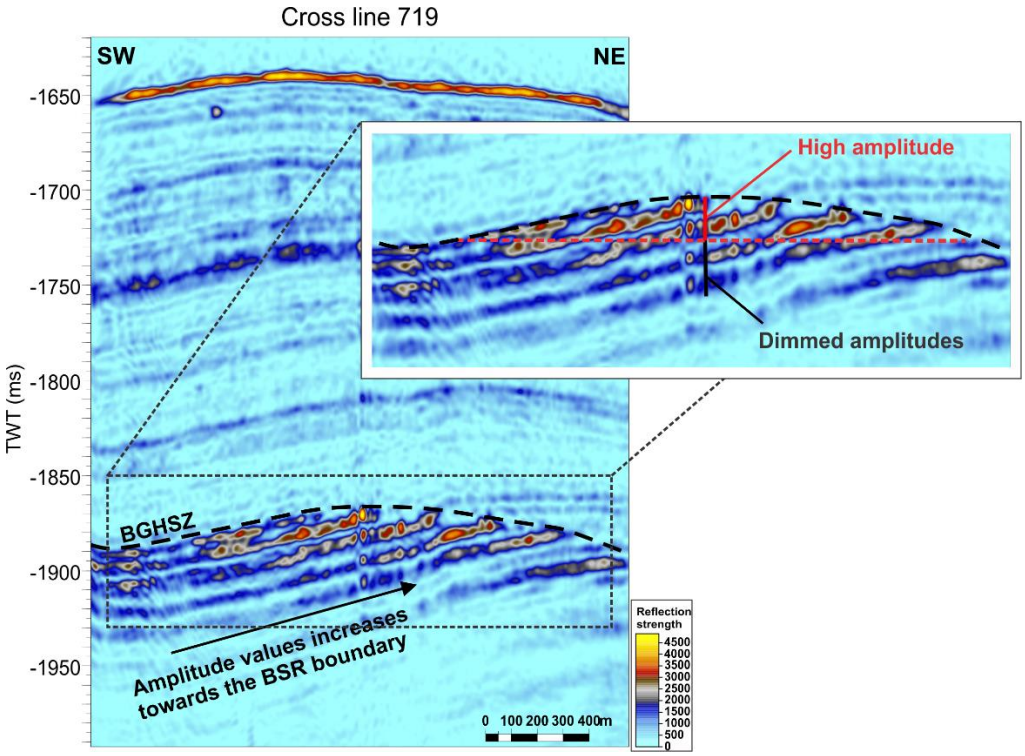

Figure 4-18: Reflection strength profile of cross line 719. Amplitudes are observed with increasing values towards the BSR boundary. Loss of reflection strength is significant below the enhanced reflections. A zoomed in view displays that the strongest amplitudes seem topographically controlled.

The reflection strength profile visualizes the distribution of the enhanced reflections and their cross-cutting effect on dipping sedimentary reflections (figure 4-18). As for the western segment, the enhanced reflections are interpreted to represent low-velocity free gas accumulating beneath hydrate-bearing sediments. Continuity and reflection strength vary laterally as well as in vertical extent. Enhanced reflections appear at its thickest below the anticlinal crest and observed thinning towards the flanks. The thickness of the zone of enhanced reflections varies, but measurements suggests an average of 100 ms (TWT). Underlying reflections appear with a dimming effect with respect to the strong reflection amplitude of overlying reflections.

A minimum amplitude map is generated to detect the lateral spread and concentration of the supposedly free gas accumulating below the BGHSZ (figure 4-19b). Distribution of large negative amplitude values show a tendency similar to the topographic shape of the BSR (figure 4-19a) and the Vestnesa Ridge crest (figure 4-15b), indicating gas accumulation controlled by the dominant topography. This can also be viewed from figure 4-18, where the strongest amplitudes values appear bounded by the anticlinal shape of the BSR.

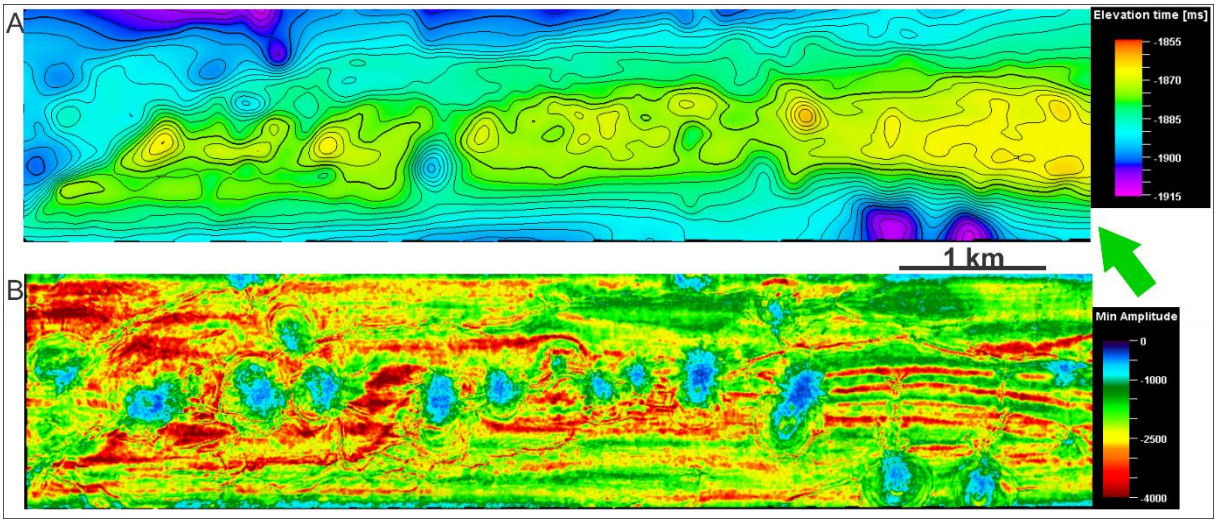

Figure 4-19: (a) Time-structure map of the BSR displaying the similar anticlinal shape as the seafloor (figure 4-15 b). (b) Minimum amplitude attribute generated from a volume 70 ms (TWT) below the BSR horizon illustrates the distribution of the largest negative amplitude values. The observed lineations of large negative amplitudes represents areas where the BSR shifts between reflections.

4.3 Hydratech.3D

The previous two datasets revealed remarkable seismic differences even though located at the same ridge. The following dataset Hydratech.3D has its location north to the northern flank of the Storegga Slide complex on the mid-Norwegian margin (figure 1-5). The seismic character of the BSR and the supposedly FGZ leaves a quite different footprint in the seismic data (figure 4-20), than what observed for Vestnesa Ridge.

4.3.1 Seismic character of the BSR

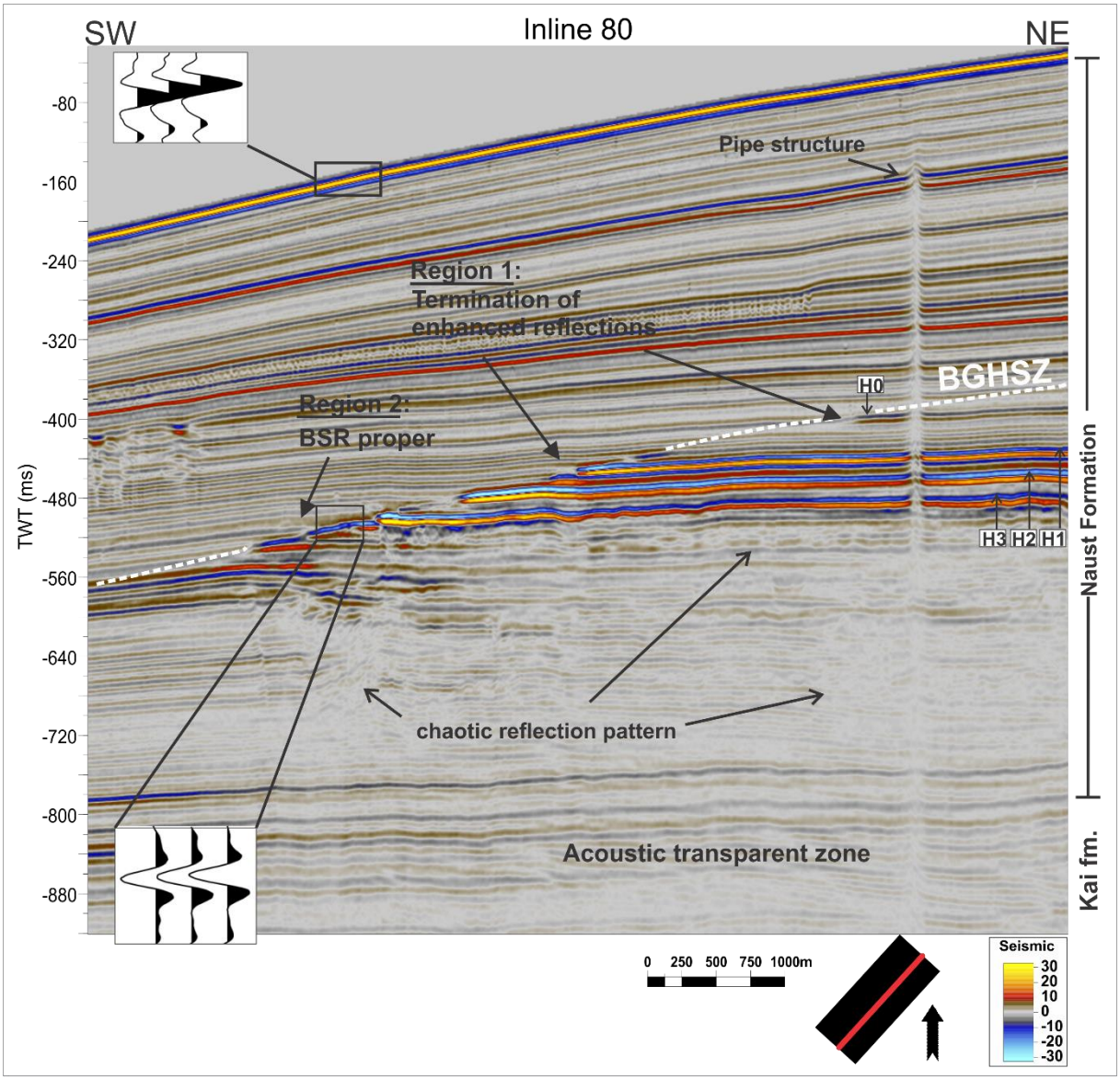

Figure 4-20: Seismic section displaying characteristics of the BSR. The BSR have opposite polarity to that of seafloor reflection (wiggle trace). The BSR is situated approximately at a depth 350ms below seafloor where it cross-cuts stratigraphic horizons as well as mimicking the seafloor, representing the base of gas hydrate stability zone (BGHSZ). BSR appearance is categorized into two regions due to its seismic signature. Three horizons are marked in the figure (H0, H1, H2 and H3), which will be referred to in this chapter.

The BSR do not occur as a continuous amplitude anomaly throughout the dataset, but rather appear restricted to certain regions within the study area. Within the Naust Formation the BSR appearance can be divided into two regions: 1) characterized as the down-dip terminations of enhanced reflections and 2) as a continuous reflection, herein termed as "BSR proper" after Bünz et al. (2004) (figure 4-20). Both regions are easily identified as their appearance cuts obliquely through the dipping strata and mimics the general seafloor topography. From wiggle trace the BSR is recognized by a reversed polarity with respect to the seafloor reflection. The discontinuous BSR is situated around 350 ms (TWT) (~300 mbsf) below the seafloor, and lies at the predicted base of gas hydrate stability zone (BGHSZ) (Mienert *et al.*, 2001; Bünz *et al.*, 2003).

Region 1: An envelope of down-slope terminations of enhanced reflections forms the BSR boundary (figure 4-20). The anomalously high amplitude horizons are interpreted to represent the acoustic expression of gas-charged sediments. Furthermore, the abrupt termination of enhanced reflections strongly suggest the presence of gas hydrate - efficiently sealing the BGHSZ. The uppermost horizon (H0) exhibit lower amplitude values than the envelope of high amplitude reflections below. Such amplitude variations indicate that particular strata hold favorable properties for gas accumulation and migration. Supporting observations are the absence of high amplitude reflections between H0 and H1. The NE part of the profile represent the topographic high, where it orients slight down-dip towards SE. An interesting observation is that the highest amplitude values of horizons H1, H2 and H3 occur towards the BSR boundary and the topographic low. As gas tend to migrate towards regions of lower pressure, one would expect strongest amplitudes at the shallowest area.

The lowermost high-amplitude reflection (figure 4-20; H3) appears more undulating than overlying reflections. Horizon H1 appears to separate a sequence of more wavy and discontinuous reflection configuration with a well-stratified and undisturbed reflection pattern above. Such pattern may indicate a change in sediments across this interface. This sequence is largely affected by acoustic transparency, making interpretations more difficult. The loss of seismic visibility of this region can be related to the overlying enhanced reflection, causing attenuation of the seismic energy (Hustoft *et al.*, 2007).

Region 2: Downslope from region 1, the BSR is recognized as a continuous reflection of highly variable amplitude values. It appears as a single reflection, where enhanced reflections below is rather absent compared to region 1. Some seismic stratification are however observed, but appears with low reflectivity. Below and to the right of this region it encounters the wavy to discontinuous reflection pattern as described above (below H1).

4.3.2 Frequency distribution

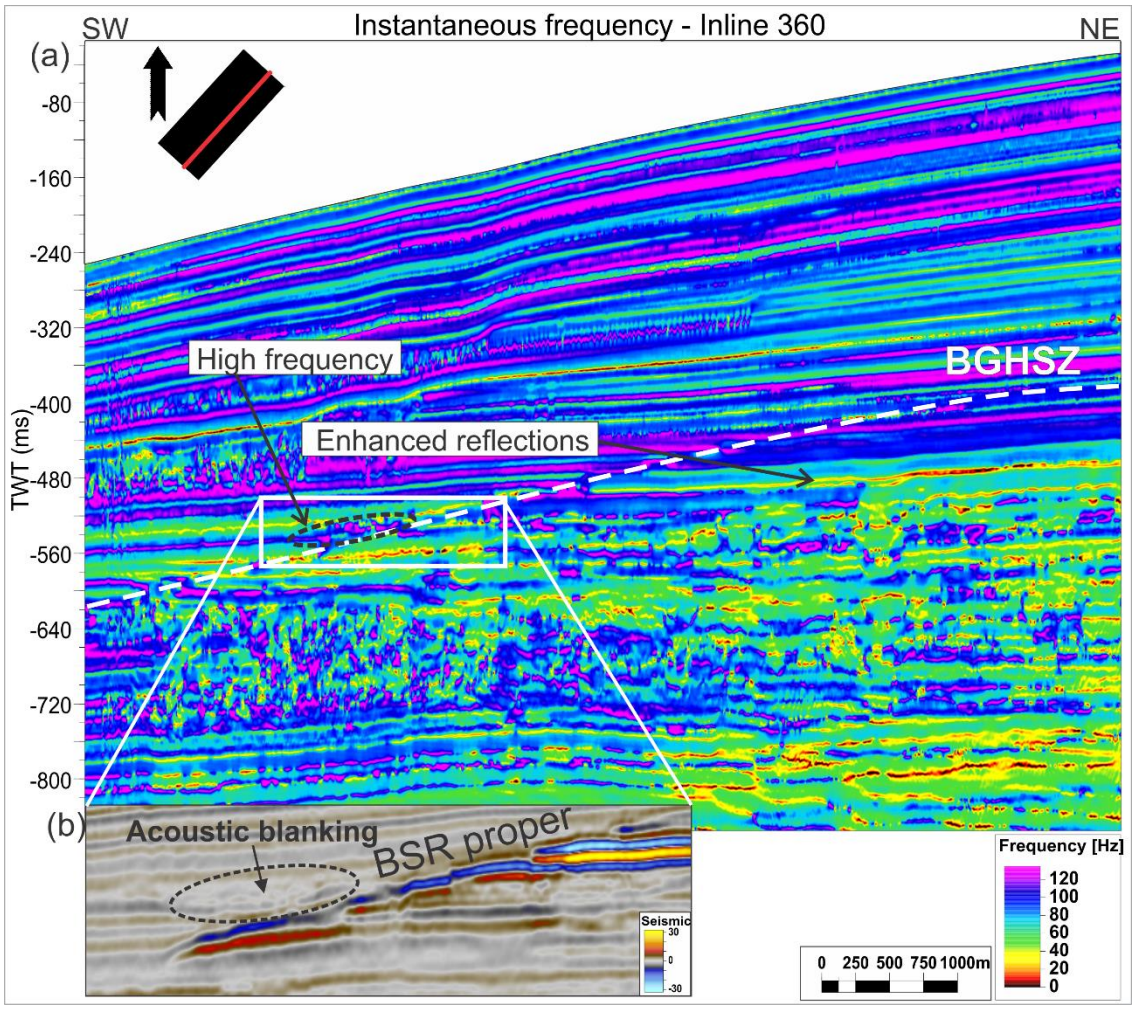

Figure 4-21: (a) Instantaneous frequency attribute showing a general trend of high frequencies above BGHSZ and a drop of dominant frequency components below. (b) The encircled area shows a region of amplitude blanking right above the BSR proper. In (a), this zone appears with high frequency content surrounded by lower frequencies.

Similar to Vestnesa Ridge, a general trend of high frequency content is observed in the sequence above the BGHSZ, whereas lower frequencies dominate the region below (figure 4-21). However, the pattern of low frequency content is not following the BGHSZ as distinct and obviously as observed for the Vestnesa Ridge. Low frequency regions are found below the BSR proper and the envelope of enhanced reflections (region 1). Additionally, a distinct zone of low frequencies are located NE, at depths below 760 ms (TWT). These low-frequency shadows are interpreted to infer the presence of free gas.

For region 1, the instantaneous frequency profile show lowest frequency content towards the topographic high, and not towards the BSR boundary where the strongest amplitude values were observed (figure 4-20). Strong reflection amplitudes are often associated with highest concentration of gas (Tucholke *et al.*, 1977; Bünz *et al.*, 2003). As free gas efficiently attenuates high-frequency components, one would expect the lowest frequency values to occur at this location.

A cluster of high frequency content is observed directly above the BSR proper. This zone stands out of the surrounding frequency content, as well as exhibiting acoustic blanking in the seismic section (figure 4-21 b). As it occur at similar stratigraphic levels – and with similar seismic characteristics as the zone below horizon H3, it might be a continuation of this zone.

The frequency tool plot (figure 4-22) displays a drop of high frequency components across the BSR. Analysis obtained from a sub-section of inline 113 reveal a loss in dominant frequencies from ~120 Hz (blue box) within the GHSZ to ~65 Hz (green box) below the BSR, supporting observations from the instantaneous frequency profile. The region within the GHSZ (blue box) show highest amplitude strength, as enhanced reflections are absent below the BSR.

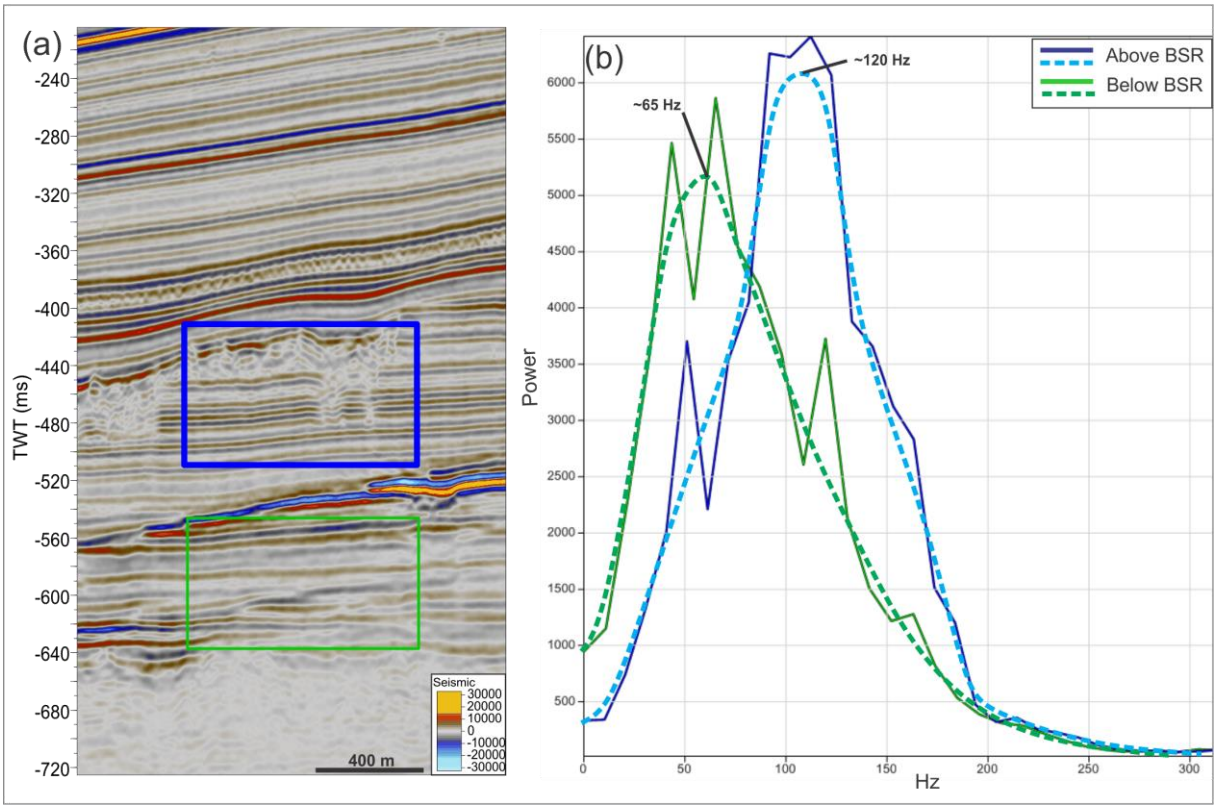

Figure 4-22: (a) A seismic section from inline 113. Boxes indicate where frequency analyses have been carried out. Blue and green boxes indicate area above and below the BSR, respectively. (b) A 1D display of the acquired frequency spectrums. Frequency (Hz) distribution versus amplitude strength (Power). Dominant frequencies above and below BSR are ~120 and ~65 Hz, respectively.

4.3.3 Pipe structures

A cluster of narrow vertical wipe-out zones (labeled 1-5) are observed at the upper slope area (figure 4-23 and 4-25). They do not intersect the BSR in the same way as the chimneys at Vestnesa Ridge, but pierce the enhanced reflections of region 1 and further into the GHSZ. Their seismic expression are characterized by dimmed amplitudes and up-bending reflections within the interior. These are interpreted to be fluid-escape features and termed pipe structures as they are much smaller in extent than the chimneys structures observed at the western and eastern segment of Vestnesa Ridge. They terminate at the same stratigraphic level within the subsurface (figure 4-23) and consequently leave no pockmarks at the seafloor.

These acoustic pipe structures are clearly observed to the base of the enhanced reflections of region 1. However, the seismic signal below pipe structure nr 1 and 2 show a zone of acoustic masking evolving to deeper levels. If the rooting zone of these pipe structures connect with deeper levels or if the masked signature represent disturbance of the seismic signal is difficult to detect as the seismic is largely acoustically transparent.

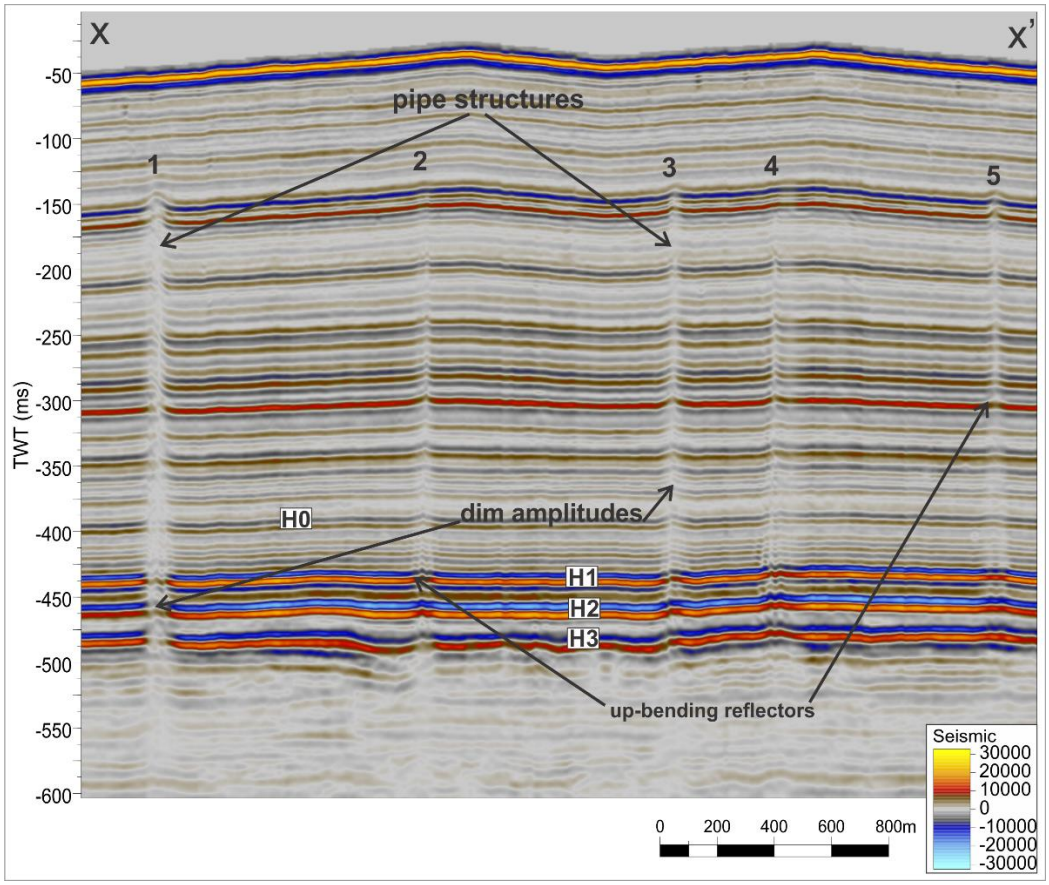

Figure 4-23: (a) a random seismic line taken through five pipe structures (labeled 1-5) observed within the dataset. Location of the line is as shown in figure 4-25, where they are observed to appear in a cluster at the upper slope area. They are recognized as vertical acoustic wipe-out zones piercing through strata, but terminating at the same depth within the subsurface. No pockmark-occurrence above these structures.

4.3.4 Seismic characterization of the free gas zone (FGZ)

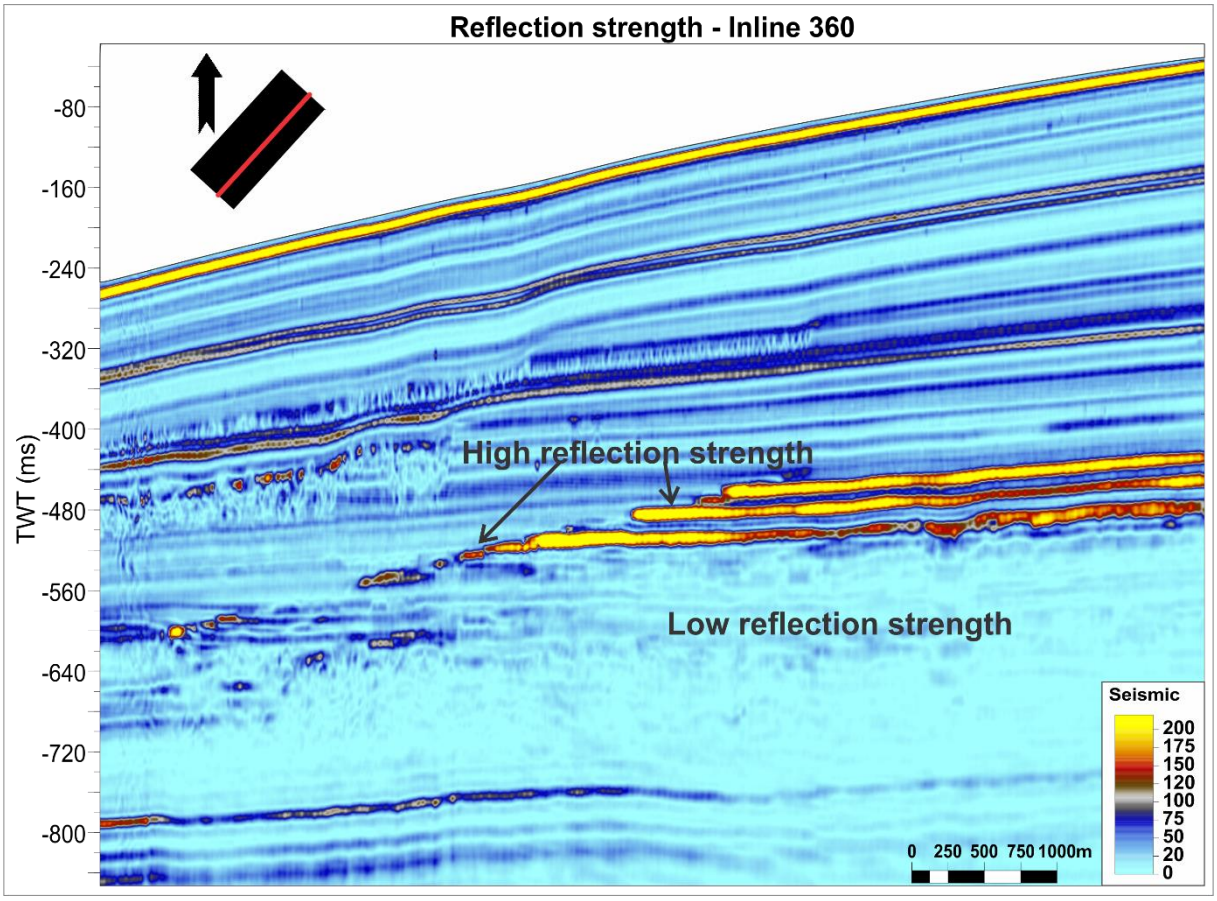

Figure 4-24: Reflection strength attribute visualize the termination of enhanced reflections. The BSR proper does not appear continuous as seen in the seismic section (figure 4-20), but rather as discontinuous spots of high reflection strength.

A free gas zone distributed in a more or less uniformly pattern below the BSR (as observed for Vestnesa Ridge) is not observed for the slope setting within Hydratech.3D. In contrast, the free gas distribution seem rather stratigraphically controlled, where enhanced reflections are restricted to certain strata (figure 4-24). The enhanced reflections of region 1 show high reflection strength, where the strongest values are observed towards the BSR boundary. As follows, the ~ 65 ms (TWT) thick region 1 is interpreted to represent the most favorably setting for gas accumulation. Horizon H0 exhibit reflection strength values of the lower part of the scale, but its terminating signature is still detectible.

The BSR proper does not appear as continuous as seen in the seismic section (figure 4-1) and rather consist of discontinuous patches of higher reflection strength. This observation could indicate lateral changes of low-impedance layers below, as lateral variations in bed thickness might change interference of the reflections and hereby cause lateral changes in the reflection strength (Miller *et al.*, 1991; Satyavani *et al.*, 2008).

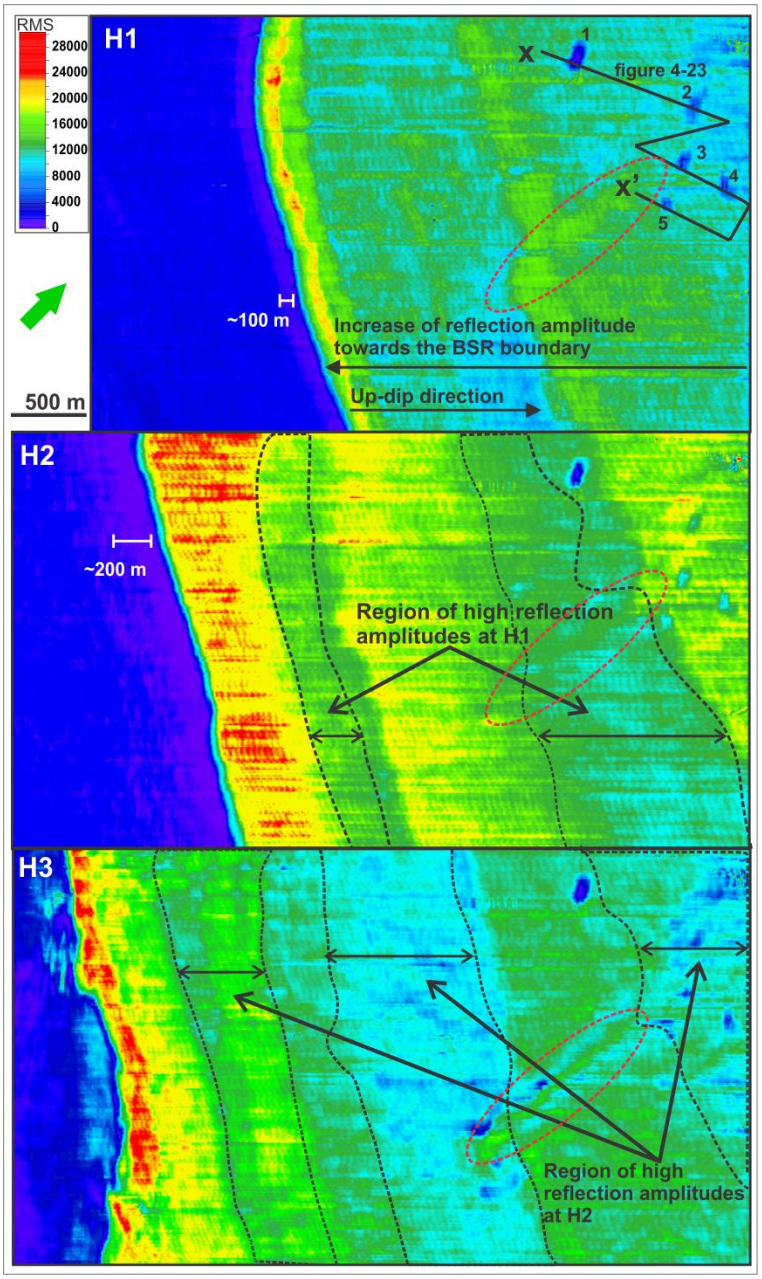

Figure 4-25: RMS-amplitude maps generated from a time window that encloses each of the interpreted horizons H1 (top), H2 and H3 (bottom) with location as indicated in figure 4-20. The random line X-X' represents the seismic cross-section of the pipe structures (1-5) in figure 4-23. Black stippled regions at each horizon (H2, H3) represent the area of high reflection amplitudes at the overlying horizon. The red dotted ellipsoid marks the location of an elongated negative relief (as discovered and described by Hustoft *et al.*, 2007). The SW-NE oriented stripes that appear on amplitude maps are attributed to acquisition artefacts.

RMS amplitude maps are generated to investigate lateral amplitude variations along the high amplitude reflections of region 1 (figure 4-25; horizons H1, H2 and H3). All three horizons show a general trend of increased reflection amplitudes towards the BSR boundary (opposite of up-dip direction), where H2 stands out by holding the largest amplitudes values throughout the horizon. The high amplitude values abruptly ends when entering the GHSZ and the lowest amplitude values are observed as a zone just

outside the BSR boundary. Comparing horizon H1 and H2, the zone appear to laterally increase with depth. Horizon H3 could not be traced continuously through the transition from the FGZ to the GHSZ, thus the amplitude variations outside the BSR boundary are disturbed and differs from H1 and H2. Other observations are the conspicuous patterns of lateral variations along each horizon. As seen from figure 4-25 (stippled area), regions holding the strongest amplitudes at horizon H1 resemble the shape of the low amplitude regions of horizon H2. Similarly, this pattern is observed between horizon H2 and H3. Such lateral amplitude variations are similar to those described for Vestnesa.3D.2007 (figure 4-8 and 4-9), only here, the strongest amplitudes are not observed in up-dip direction.

Hustoft et al. (2007) was the first to describe an elongated negative relief at the base of the enhanced reflections, overlying a zone of hydraulic fractured sediments. At the base of the Naust Formation, a similar shaped antiform structure are situated beneath the network of fractured sediments. The paper further suggested that it represents a conduit for gaseous fluids, allowing upward fluid migration from the base of the Naust formation to shallower strata of higher porosity and permeability. From figure 4-25 (red dotted ellipsoid), the elongated negative relief is detectable by its high reflection amplitudes within all three horizons, which further supports that free gas occur at higher concentrations along this feature.

5. Discussion

The previous result chapter presented seismic characteristics from three different areas, two datasets from the Vestnesa Ridge (Vestnesa.3D.2007, Vestnesa.3D.2013) and one north to the northern Storegga sidewall on the mid-Norwegian margin (Hydratech.3D). The BSR appearance and the underlying free gas zone (FGZ) showed remarkable differences in these different geological settings. This chapter discusses the amplitude anomalies and geological controls of the BSR appearance, as well as the distribution and geometry of the free gas zone (FGZ). The BSR behavior in relation to chimney structures are investigated, and possible scenarios are presented.

5.1 Seismic indicators of gas hydrate and free gas

Geophysical evidence of a prominent BSR at Vestnesa Ridge and north to the northern flank of the Storegga slide escarpment infer that gas hydrates are ubiquitous within these regions. Although BSRs on seismic reflection profiles act as a gas hydrate indicator on continental margins worldwide (e.g. Markl *et al.*, 1970; Yuan *et al.*, 1998; Posewang and Mienert, 1999; Lee et al., 2005), hydrates have been recovered at sites without signs of BSR (Holbrook *et al.*, 1996). Despite the fact that partially hydrated sediments may cause increase in acoustic velocity, recent work addresses the strong impedance contrast to mainly result from the low-velocity free gas trapped beneath the hydrate stability zone (Holbrook, 2000; Wood and Ruppel, 2000; Tinivella *et al.*, 2002).

As the BSR is associated with the base of the hydrate stability zone (BHSZ), its distribution and sub-bottom depth varies between the study areas as it depend on pressure (water depth), bottom water temperature and the ambient geothermal gradient for the particular regions. Other parameters that control the stability of gas hydrates are gas composition, pore water salinity and local geology (Bünz *et al.*, 2003; references therein).

High-resolution 3D reflection data from the three areas share common BSR characteristics; enhanced reflections terminating abruptly at the BGHSZ, thus forming the characteristic cross-cutting behavior while mimicking the seafloor morphology at sub-bottom depth (figure 4-2, 4-11, 4-20). Its reversed polarity relative to the seafloor manifests that the BSR can be linked to a gas hydrated system and not as a result from the similar BSR behavior arising from an Opal-A/opal phase boundary. A diagenesis-related BSR would exhibit same polarity as the seafloor reflection (Davies and Cartwright, 2002; Lee *et al.*, 2003).

Seismic blanking within the hydrate stability zone are frequently used as a supplementary hydrate indicator at several gas hydrate provinces (Shipley *et al.*, 1979; Dillon *et al.*, 1993; Wood and Ruppel, 2000). The reduction of seismic amplitudes are linked to reduced impedance contrast caused by hydrate-

cemented sediments (Dillon et al., 1993). Although Petersen et al. (2010) reported an interval of blanking directly above the BSR at Vestnesa.3D.2007, such blanking phenomena are not included in the result chapter, as I could not observe appreciably geophysical evidence for this within any of the datasets. For clarification, this statement only cover blanking zones as an interval above the BSR, and do not include vertical blanking zones linked to acoustic chimneys and faults. Holbrook et al. (1996) and Holbrook et al. (2002) addresses the complexities by associating seismic blanking to hydrate concentrations, as a uniform sedimentary section overlying highly reflective gas layers may produce similar low reflectivity zones.

Velocity analysis from Vestnesa Ridge (Petersen *et al.*, 2010) (figure 5-1 b) presented a 20 m thick zone with P-wave velocities of 1800 m/s just above the BSR. Below the BSR, a 7 m thick interval occurred with velocities between 1250 m/s, but all together a 35 m thick zone of low-velocities were revealed from the velocity profile (Petersen *et al.*, 2010). Similar analysis for the Hydratech.3D area (figure 5-1 a) was carried out by Bünz et al. (2005) and reported an up to 50 m thick zone with interval velocities of 1800-1900 m/s above the BSR. Directly below the BSR, a 90 m thick zone showed P-wave velocities ranging from 1400 m/s to 1600 m/s. Such velocity analysis are commonly used to infer and estimate gas hydrate occurrence (e.g. Hoolbrook et al., 1996; Bünz and Mienert, 2004; Petersen *et al.*, 2007) and strongly suggest that significant amounts of gas hydrate and free gas are present within the study areas of this thesis.

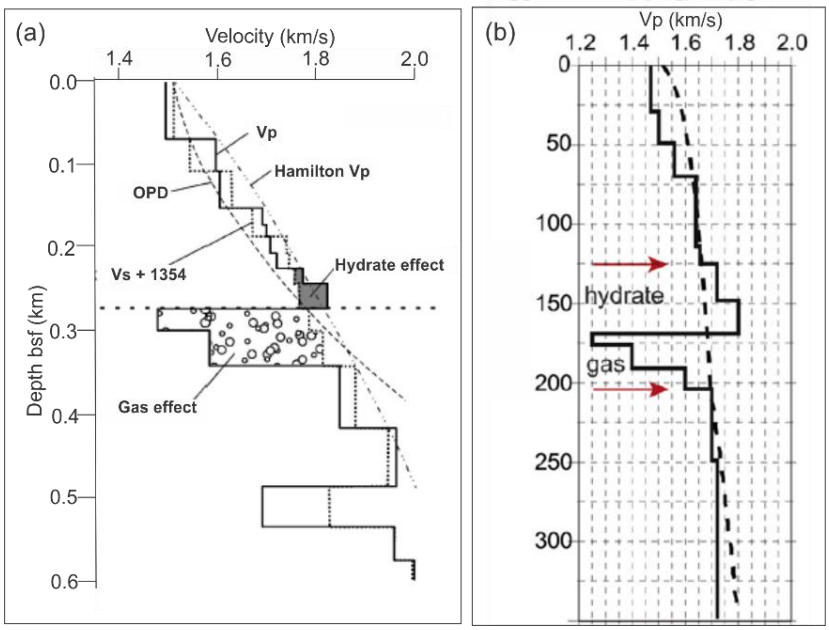

Figure 5-1: (a) P-wave velocity profile (figure from Bünz *et al.*, 2005) from the Hydratech area. (b) P-wave velocity profile from Vestnesa Ridge (more precisely Vestnesa.3D.2007). Dashed line represent a reference curve from hydrate- and gas free sediment (figure from Petersen *et al.*, 2010; and references therein).

5.2 Frequency distribution

The low-frequency shadows observed from instantaneous frequency plots (figure 4-3, 4-13, 4-21) support the above mentioned velocity studies and makes it reasonable to interpret that free gas accumulates below the BGHSZ. It is an effective and widely used method to detect gas-rich zones (Berndt et al., 2004; Hustoft *et al.*, 2007; Satyavani *et al.*, 2008; Geletti and Busetti, 2011), as gas effectively absorbs high frequency component of the seismic energy due to internal friction and hereby causing a shift towards lower frequencies below (Taner *et al.*, 1979; Taylor *et al.*, 2000). Addressing high instantaneous frequencies to regions of gas hydrate occurrence serve more difficult, as hydrate-free sediments would show high frequency values as well. High instantaneous frequencies were observed to vary laterally where the BSR truncates and shifts between reflectors (figure 4-3b, 4-13b). If layers thin to a quarter period of the dominant seismic energy, the thinning is revealed by an anomalous increase in instantaneous frequency (Robertson and Nogami, 1984). At the transition between the FGZ and GHSZ, thin gas layers may pinch-out laterally and cause frequency tuning and hereby result in the observed concentrated high frequency zones.

Moreover, the frequency tool plot manifests that high frequency components are attenuated across the BSR boundary (figure 4-4, 4-14, 4-22). From the frequency tool plots, Vestnesa.3D.2007 and Hydratec.3D show a similar shift in frequency content of 55 Hz from ~120 to ~65 Hz. Vestnesa.3D.2013 show a larger shift of ~65 Hz from the GHSZ (~145 Hz) to the FGZ (~80 Hz). Acquisition and processing of Hydratech.3D and Vestnesa.3D.2007 provided a dominant frequency of ~80 Hz, whereas Vestnesa.3.D.2013 was acquired with higher acquisition frequencies. It is possible that the high frequencies of Vestnesa.3D.2013 induces a larger drop in frequency content. Vanneste et al. (2001) carried out a comparative study of seismic datasets acquired with different frequency sources, and observed that the BGHSZ acted more efficiently as a low-pass filter for higher acquisition frequencies.

5.3 Pull-up and push-down effects associated with chimneys

As presented in the result chapter, pull-up and push-down effects of the BSR are frequently associated with chimney structures. However, the extent and distribution of these effects and features show remarkable differences when comparing each dataset. In the following sections, schematic models will be presented to illustrate possible scenarios for the observed BSR and general seismic expressions.

Pull-up and push-down effects are commonly explained as either a structural and/or as velocity effect (Petersen *et al.,* 2010; Plaza-Faverola *et al.,* 2010). Downward deflection of reflections can be related to an overlying low-velocity gas-zone, where the seismic wave uses longer travel-time compared to surrounding sediments (Barth *et al.,* 2009). Pull-up is the opposite effect where material of high sound-velocities (i.e. authigenic carbonate, gas hydrate) will cause the seismic wave to reach the surface seismic receivers faster than surrounding strata (Hustoft *et al.,* 2007¸ Paull *et al.,* 2008). Structural effects may correspond to mud diapirism (Hustoft et al., 2007) or sediment deformation by vigorous flow of gas rich fluids (Petersen *et al.,* 2010).

5.3.1 Vestnesa.3D.2007

The western end of Vestnesa Ridge show evidence of numerous chimney structures indicative of focused fluid flow activity. However, no acoustic gas seepage activity has been detected from this part of the ridge (Bünz *et al.,* 2012). Despite the variable internal structure of the chimneys, the BSR is generally represented by what resembles a pull-up effect overlying push-down effects within the FGZ (figure 4-5, 4-6). Such pattern suggest hydrate accumulation above the BSR, whereas the seismic blanking, combined with low frequencies within the FGZ makes it reasonable to associate push-down with the presence of free gas below the BSR. This interpretation is schematic illustrated in figure 5-2. The quite large zone of enhanced reflections indicate that significant amount of gas are accumulating below the ridge and close to the chimneys. However, as no venting activity has been detected from this part of the ridge, it strongly suggest that these fluid-pathways have become impermeable, thus possible clogged by gas hydrates. Between the BSR and the seafloor both push-down and pull-up effects occur along the chimneys interior, making interpretation of its material more difficult. However, one cannot rule out contribution from deformational processes.

Where faults and fractures cut through the FGZ and into the GHSZ, the BSR and reflectors deflect upwards against the narrow wipe-out zone. As this pattern is observed within the FGZ as well as the GHSZ it is suggested to be the result of the faulting pattern, rather than a velocity effect due to high-velocity gas hydrate (figure 5-2 b). The upward migration of warm fluids may as well locally push up the BSR (Vanneste *et al.,* 2005b; Madrussani *et al.,* 2010). Pockmarks underlain by high amplitude reflections strongly suggest upward directed fluid flux through faults, which may lead to hydrate or

possibly gas accumulation at these shallow stratigraphic levels. The enhanced reflections close to the fault structure, suggest that faults act as permeable conduits and supply the FGZ with gas laden fluids.

Some chimneys differs slightly from others by appearing with truncated reflectors against a quite distinct high amplitude segment at BSR level (figure 4-5; chimney 1 and 3). Plaza-Faverola et al. (2011) reported similar truncations towards dome-like features of the chimneys, where a possible explanation were preservation of paleo-carbonate domes. For details regarding the burial-process, the reader is referred to Plaza-Faverola et al. (2011). By such, these features may represent buried authigenic carbonate. However, Hustoft et al. (2009) points out that structures on Vestnesa Ridge most likely have formed recently, which makes it unlikely that burial of carbonate deposits have reached these depths. Hence, the high amplitude segments are more likely to originate from gas hydrate or free gas (Petersen et al., 2010). Precipitated carbonates might however occur within the sulfate reducing zone few meters from the seafloor (figure 5-2b). The high RMS-amplitudes within pockmarks (figure 4-6 a) may be explained by formation of authigenic carbonates, gas hydrates and/ or free gas (if enclosed by gas hydrates) (Petersen et al., 2010).

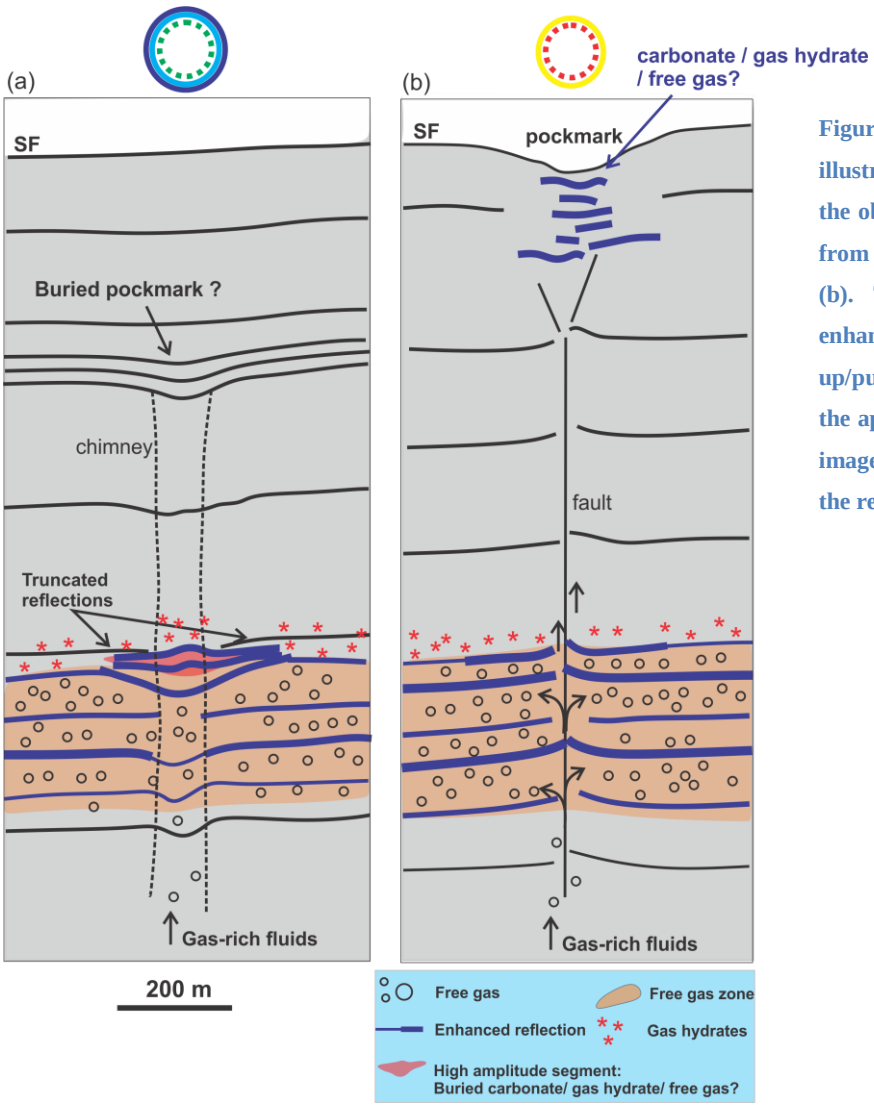

Figure 5-2: A schematic model illustrating possible scenarios for the observed seismic characteristics from figure 4-5; chimney 1 (a) and 4 (b). The sketched horizons, the enhanced reflections and the pull-up/push-down features represent the appearance as seen in reflection images. For the color-coded circles the reader is referred to figure 4-6.

5.3.2 Vestnesa.3D.2013

During cruises in 2010 and 2012, the eastern segment of the Vestnesa Ridge proved to be a highly active gas-seepage site. Gas flares were recorded to rise from pockmarks, reaching heights of 990 m (Smith *et al.*, 2014). In contrast to the western segment chimneys, the BSR appearance within chimneys at the eastern segment revealed large internal variations. Despite the BSR being completely wiped-out within the center of chimneys, the onset and end of chimneys revealed significant pull-up and push-down effects, respectively (figure 4-15, 4-16). Other striking observations are the different magnitude of these effects between the leaking (largest pull-up) and non-leaking chimney (largest push-down) (figure 4-16 b).

As formation of gas hydrates and/or authigenic carbonate may clog and efficiently seal possible migration pathways (Hovland, 2002), the large push-down effect observed from the non-leaking chimney (figure 4-15c and 4-16b) may indicate that significant gas concentrations are trapped within the strata between the BSR and the seafloor. How gas is able to bypass the GHSZ is still unclear and will not be discussed here, however, possible mechanisms are presented in Bünz et al. (2012) and Smith et al. (2014). The fact that gas hydrate and methane-derived carbonates has been recovered from both piston- and gravity core within a pockmark site (Smith et al., 2014), makes them a suitable candidate for the suggested sealing-effect.

The large pull-up effect within the leaking chimney may be attributed to significant concentrations of gas hydrates (figure 4-16a). Depending on the concentration, hydrate can either enhance or suppress seismic reflectance (Holbrook *et al.*, 2002). High hydrate saturation may have velocities significantly greater than the surrounding sediment, thus generating enhanced reflectance (Holbrook *et al.*, 2002). As follows, the discontinuous high amplitude segments observed within a ~100 ms (TWT) thick zone above the pull-up feature (figure 4-16 a) might represent significant gas hydrate accumulations (as illustrated in figure 5-3a).

The morphology within the leaking pockmark resembles the smooth morphology of the non-leaking pockmark, with exception of a defined region of a noticeably rougher expression (figure 4-17). This region also revealed a cluster of higher RMS-amplitudes (figure 4-17; black dotted circle). Below this specific region the BSR is represented by a push-down effect, and reflectors in general show a down-bending tendency towards the acoustic wipe-out zone. Here, high amplitude reflections are concentrated within 50 ms (TWT) directly below the seafloor. The bright reflections could represent the occurrence of gas, which consequently would absorb the energy, thus leaving less seismic energy to record strata below (as no bright spots are seen in the underlying strata).

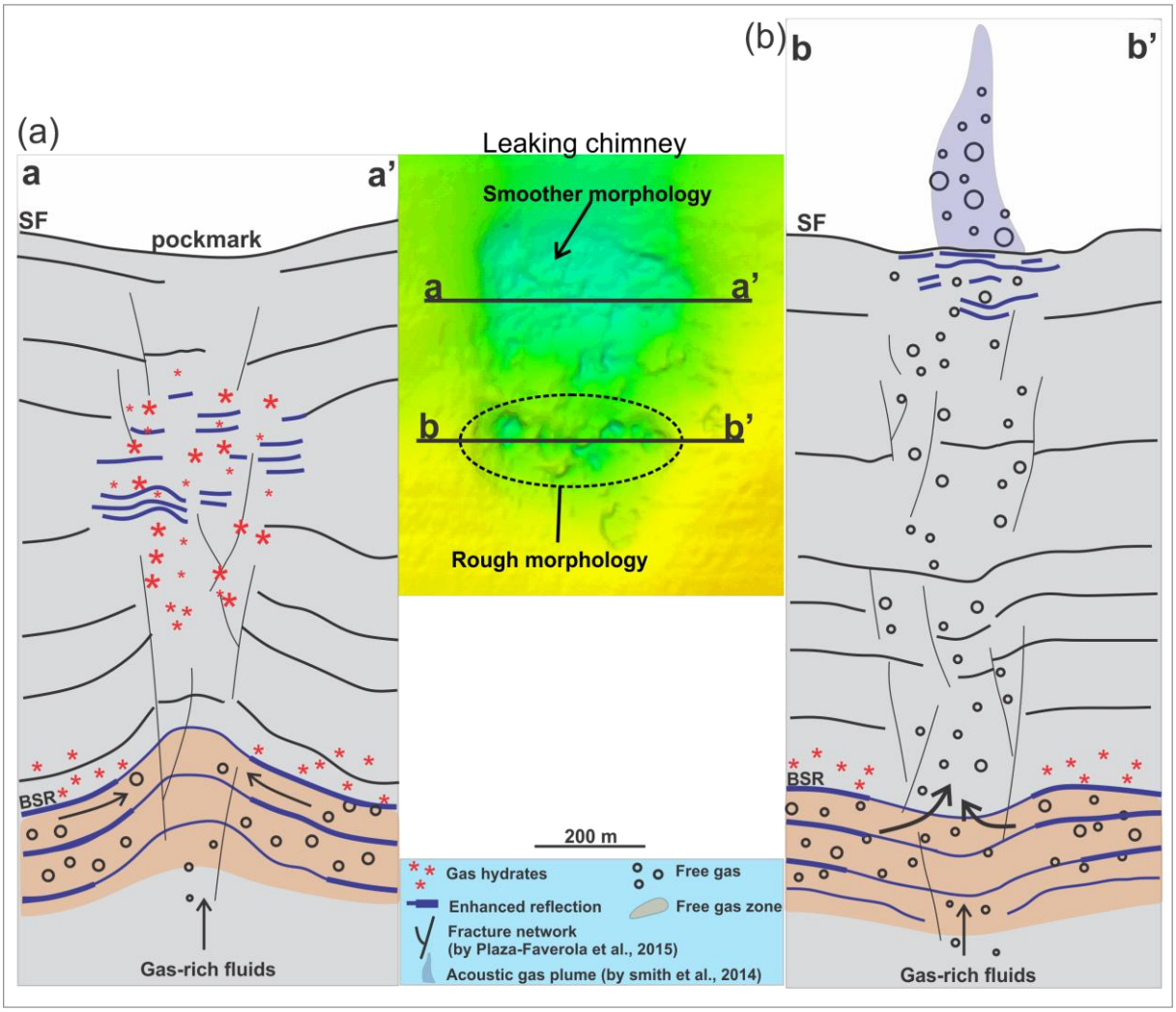

Figure 5-3: A schematic illustration possible scenarios explaining the observed seismic characteristics of the leaking chimney (as seen in figure 4-16) (a) Profile aa' as indicated from the time-structure, describes the seismic characteristics beneath the smoother part of the pockmark morphology. (b) Profile bb': describes the seismic characteristics below the rough pockmark morphology. The sketched horizons and the pull-up/push-down features represent the appearance as seen in reflection images.

The above mentioned characteristics and the internal BSR variations, makes it tempting to suggest that this particular region represents a local pathway for the hydro-acoustically detected gas seepage (as visualized in figure 5-3 b). Due to the self-sealing effect of carbonate cementation and gas hydrates (Hovland, 2002), the smoother part of the leaking pockmark might be partly sealed by cemented carbonate or gas hydrates (as interpreted for the non-leaking chimneys), forcing upward migration of gas to relocate at more permeable areas within this structure. This would only be somewhat speculative and would require ground-truthing analysis (i.e. sampling from the specific location) to draw any conclusions.

Backscatter data could be supplementary research, as variations in backscatter strength provide indications of changes in pockmark-material (i.e. detect authigenic carbonate/gas hydrate) (Holbrook et al., 2002; Naudts et al., 2006; and references therein). However, the highly disrupted seismic from this area makes it reasonable to suggest that the observed effects are partially related to sediment deformation due to a vigorous flow of fluids. Additionally, the shifted and up-warped BSR might be the result warm fluids ascending from depths below, causing a displacement of the BGHSZ as has previously been suggested by Bünz et al. (2012) and for the Nyegga area on the mid-Norwegian margin (Hovland and Svendsen, 2006).

Since both non-leaking and leaking pockmarks occur at this part of the ridge, it allows comparisons of the seismic characteristics of the chimneys in relation to the different BSR appearances. For a greater understanding and to see if any systematic similarities occur, these structures should be investigated more comprehensively.

5.3.3 Hydratech.3D

The pipe structures observed within the Hydratech.3D-dataset do not show the complex structure of those observed on the Vestnesa Ridge. They do not pierce the BSR, but can be traced through the enhanced reflections of region 1 and appear as buried pull-up features terminating at the same stratigraphic level (figure 4-20, 4-23). They appear with similar seismic expressions, where reflectors bend upwards within the pipes interior. Based on the previous interpretations and the absence of push-down effects, such pull-up effects may indicate that these structures are filled with high-velocity material, i.e. gas hydrates, authigenic carbonates. However, without any ground-truthing research, one cannot rule out sediment deformation caused by the upward moving fluids at early stages of the pipe formation (Plaza-Faverola *et al.*, 2011).

Outside the scope of this dataset, numerous seafloor pockmarks and pipe structures have been reported (Berndt *et al.*, 2003). Here, sediment samples from pockmarks and pipes indicated a material infill of cemented methane-derived authigenic carbonates, which both reduces sediment permeability as well as increasing seismic velocities (Paull *et al.*, 2008). The similar seismic expression leads to infer that the observed pipe structures has previously acted as fluid pathways for overpressured sediments, but at present day represent ancestral structures containing high-velocity material.

5.4 Reflection amplitude variation of the BSR

Several authors has shown that BSR characteristics and continuity differs between high- and low-resolution data (Spence *et al.*, 1995; Vanneste *et al.*, 2001; Dewangan *et al.*, 2007). On low-frequency data (conventional seismic data) the BSRs are represented as a continuous high-amplitude reflection. Whereas, high-resolution data expresses the BSR as the termination of separate enhanced reflections of more variably reflection amplitudes. The latter is consistent with observations in this thesis (figure 4-2, 4-12 and 4-20). The different BSR appearance are described to result from the differences in frequency-controlled horizontal and vertical resolution (Vanneste *et al.*, 2001), as explained more thoroughly in the previous section 2.6.

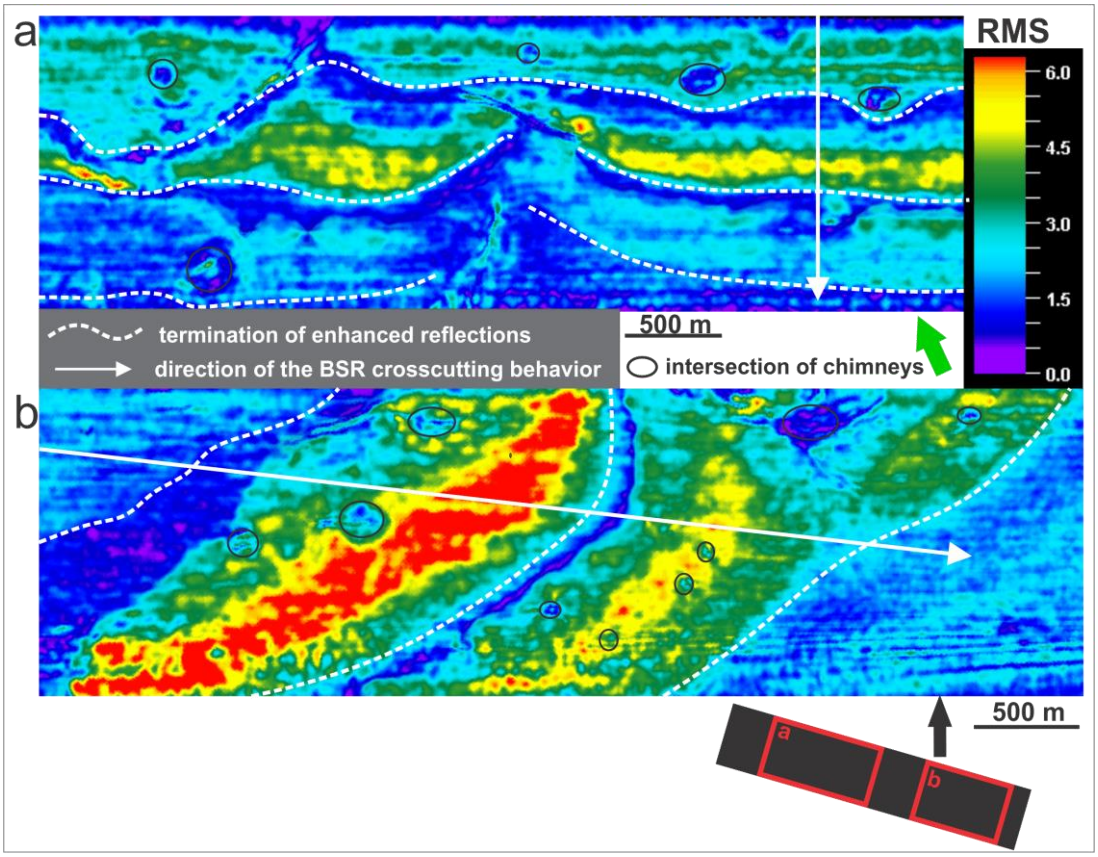

Figure 5-4: Displaying zoomed in view of the RMS amplitude distribution of the BSR at Vestnesa.3D.2007. Due to the cross cutting behavior of the BSR, it appear as curvilinear zones of alternating RMS-amplitudes. Particular reflection-terminations appear with higher amplitude values (red/yellow). As indicated by white arrows, the BSR is formed by termination of enhanced reflections in both inline and cross line direction.

As the BSRs are formed by the upper boundary of enhanced reflections terminating at the base of the GHSZ it strongly infers that sediment properties change across this boundary, thus indicating an efficient seal of low-permeability gas hydrates. Observations from all three datasets reveal that the BSRs are not consistently the strongest reflection (figure 4-2, 4-20, 5-6 c). An amplitude extraction of the BSR at Vestnesa.3D.2007 are shown in figure 5-4 to exemplify the amplitude variation observed within the three datasets. The figure visualizes that particular terminating horizons hold stronger amplitude values than other, thus indicating a relationship between the properties of the individual layers and the observed amplitude strength of the BSR. Several authors relate amplitude alternations to the presence or absence of free gas trapped beneath the BSR and the thickness of the layer (Miller *et al.,* 1991; Bangs *et al.,* 1993; Vanneste *et al.,* 2005b; Le *et al.,* 2014). Chapman (2002) suggested that a gradational transition between the hydrate and underlying gas represent would result in weaker BSR amplitudes.

At Vestnesa Ridge, the high amplitude horizons at BSR level, also appear with high amplitude values within the FGZ (figure 4-2, 4-12). Such observations strongly indicate that particular layers exhibit higher gas concentrations and thus suggesting alternating beds of higher and lower porosity and permeability. Similar for Hydratech.3D, the enhanced reflections of region 1 (figure 4-20) have previously been interpreted as the most favorable section for gas accumulation. As the BSR proper (region 2) appear with weaker reflection amplitudes, it would equally suggest a lower gas concentration immediately beneath the BSR reflection. The absence of enhanced reflections below the BSR proper would support this explanation. The BSR proper is observed as a continuous reflection in seismic reflection data, but appear as rather discontinuous patches of high reflectivity in the reflections strength attribute (figure 4-24). Due to these observations, it was suggested by Bünz and Mienert (2004) that the continuous reflection results from the tuning effect. By only using seismic data to relate high reflection amplitudes to elevated gas and/or hydrate concentrations are a complex matter and should be constrained by core data and well logs.

A study by Davies et al. (2014) reported intricate patterns of high- and low reflection amplitude trails along a continuous BSR, offshore of Mauritania. These pattern deflected around chimney intersections and were proposed as earlier (possibly already converted to hydrate) and active flows (gas flow). Investigating if similar patterns occurred within the datasets proved difficult, as regions of continuous BSRs are highly limited.

5.5 Accumulation and migration within the FGZ

Enhanced reflections directly below the BSR are common features on seismic records from gas hydrate provinces (Shipley *et al.*, 1979; Bouriak *et al.*, 2000; Vanneste *et al.*, 2001). It is a generally agreement that these high amplitude reflections represents the presence of free gas and the occurrence of free gas beneath BSRs has on several sites been confirmed by drilling (Bangs *et al.*, 1993; Holbrook *et al.*, 1996). The seismic data from Vestnesa Ridge and at Hydratech.3D reveal significant differences in FGZ geometry (figure 4-18, 4-24), indicating that the distribution of the FGZ at each site is affected by different controlling factors.

5.5.1 Vestnesa Ridge (Vestnesa.3D.2007 and Vestnesa.3D.2013)

The anticlinal shape of Vestnesa Ridge are a controlling factor for the observed FGZ. Observations from figure 4-18 and 4-19, show that the strongest amplitudes are concentrated directly below the crest. As illustrated in figure 5-5, porous and permeable layers are suggested as migration pathways for the free gas, which together with water forms an impermeable seal of gas hydrates at the BGHZS. The relationship between the up-dipping strata and the location of the BGHSZ allow gas to migrate along strata and accumulate at the topographic high, below the boundary represented by the BSR. Subsequently, these porous sediment-layers are also suggested to hold the most favorable properties for gas hydrate formation. This depicts the formation of the BSRs crosscutting behavior and how gas accumulation and distribution on Vestnesa Ridge are largely morphologically controlled. This is supported by previous research from the Vestnesa Ridge (Bünz *et al.*, 2012).

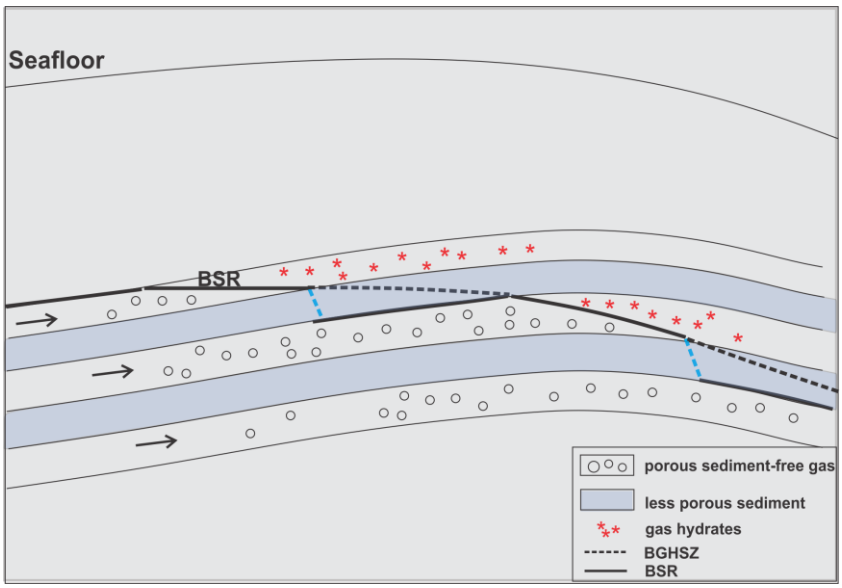

Figure 5-5: Schematic illustration demonstrating how the anticlinal topography and the up-dip of layers control the geometry of the FGZ, allowing free gas to migrate and accumulate at higher concentrations below the crest area.

The thickness of the FGZ show an average of 100 ms (TWT) for both the eastern and western segment of the ridge. Enhanced reflections occur in close relation to faults (figure 4-5, 5-6) and especially fault-bounded sediments appear with strong amplitude reflectors. Figure 5-6 also show that the BSR is not necessarily the strongest reflection and that particular high amplitude horizons within the FGZ appear more favorable for gas accumulation. This makes it compelling to suggest that faults acts as highly permeable conduits within the FGZ and thus contribute to the gas distribution within the FGZ. A previous study from the West Svalbard margin related the thickness of the FGZ to be a fault-induced compartmentalization of the gas reservoir (Madrussani *et al.*, 2010). This is consistent with the observations from this study, although some faults appear with more sealing-effect in some directions (figure 5-6 b; fault 1 separate strata with higher and lower reflection strength).

Petersen et al. (2010) suggested that the base of the GHSZ might be significantly deformed by the vigorous flow of fluids, some of which might result from the hydrothermal circulation in this setting near the mid-oceanic ridge. Supporting observations are the seismic indications of both buried pockmarks/chimneys and truncations of reflectors (figure 4-5), which may indicate several active periods of fluid flow (Plaza-Faverola *et al.*, 2011).

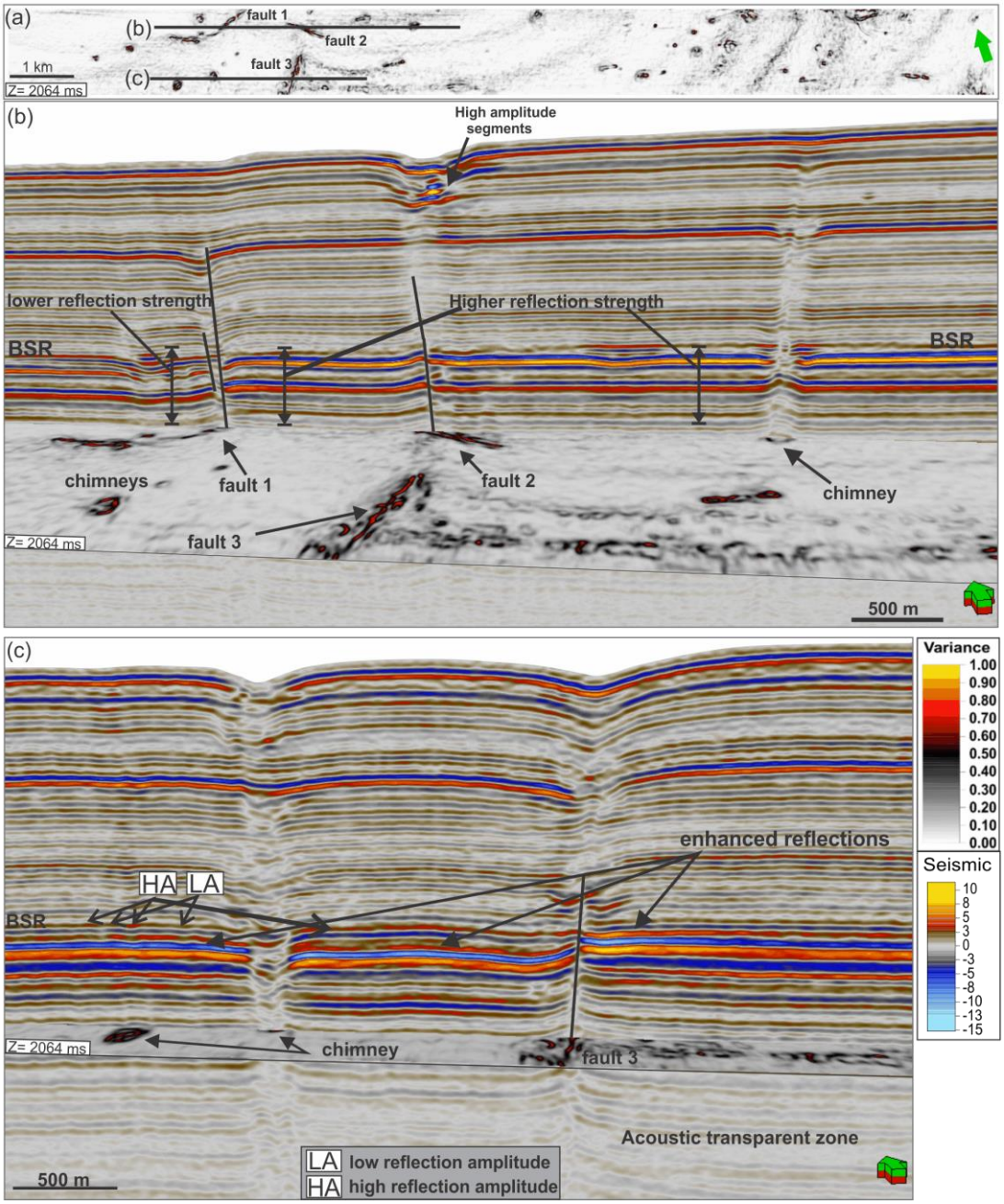

Figure 5-6: A figure from Vestnesa.3D.2007, illustrating enhanced reflections in relation to faults. (a) A variance attribute time-slice at 2064 (TWT) where faults appear as lineations of high variance values. (b) displays the high amplitude reflections in vicinity to faults. However, fault 1 separate a section of lower reflection strength with a section of higher reflection strength. (c) Displays the alternating BSR amplitude variations, as well as high reflection amplitude of specific layers within the FGZ.

5.5.2 Hydratech.3D

For Vestnesa Ridge it was shown how gas accumulation would naturally migrate and accumulate beneath the topographical high and thus forming a rather uniform FGZ directly below the BGHSZ. For the slope setting within the Hydratech-dataset, the situation is quite the opposite. As illustrated in figure 5-7, the BSR has a steeper apparent dip than the slight up-dipping dominant strata, and thus, due to buoyancy forces, gas would migrate away from the BGHSZ. This particular setting is not favorable for natural gas accumulation below the BGHSZ and consequently influences the BSR appearance, as well as the formation and geometry of the FGZ. This is consistent with the seismic observations; where the BSR and FGZ is rather limited and confined to two regions (figure 4-20). BSRs expressed as down-dip termination of enhanced reflections are much less regularly seen in gas hydrate provinces (Vanneste *et al.*, 2001).

As the enhanced reflections are largely restricted to region 1, it suggest a distinct stratigraphic and lithological control on the accumulation of free gas. For gas to be able to exist in significant amounts in down-dip direction, a possible explanation is that lateral gas migration is inhibited by being stratigraphically sealed in further up-dip direction, thus allowing gas to accumulate at high concentrations within region 2. However, this is only speculative, as the dataset do not cover the upper slope settings.

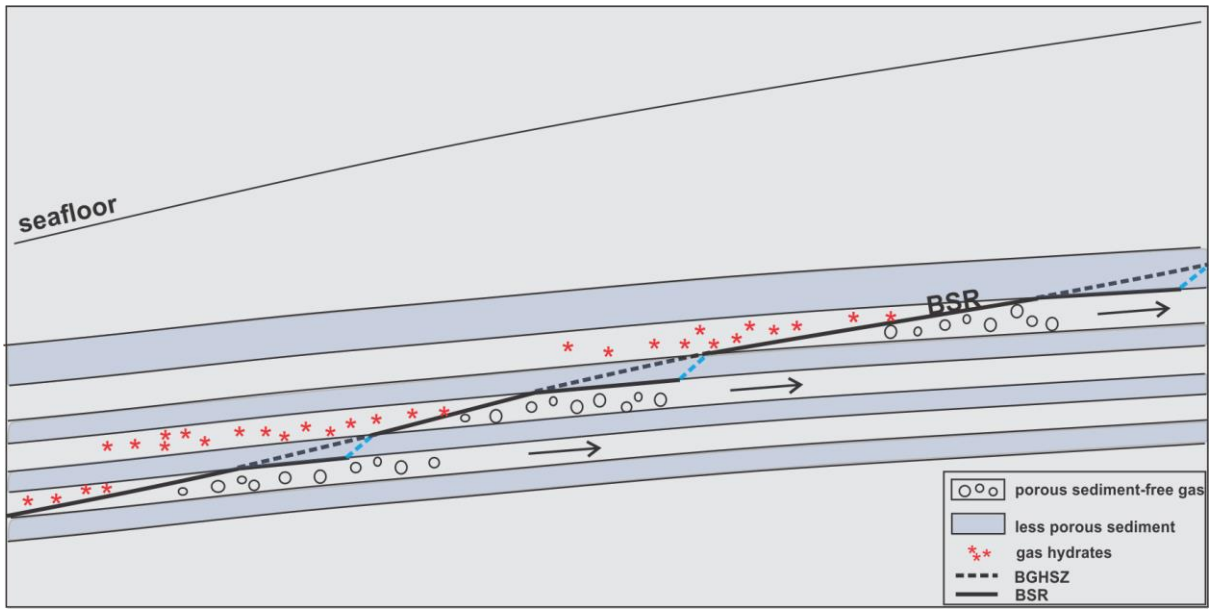

Figure 5-7: Schematic illustration demonstrating how the dip of the dominant strata related to the steeper inclined BSR influences the geometry of the FGZ. Free gas would migrate away from the BGHSZ.

P-wave velocity analysis from Bünz and Mienert (2004) revealed a particular region with the most preferable host sediments for gas accumulation and gas hydrate formation. This region correspond to the horizon H2 in this thesis. From figure 4-25 it can be seen that horizon H2 appear with generally higher amplitude values than the overlying and under lying horizons, which may indicate that gas occur in higher concentrations. As region 1, and particularly H2 appear as the preferred location for gas accumulation, it is also suggested to hold the most suitable geological properties for gas hydrate formation across the BGHSZ.

No faulting activity was detected to cross the BSR and the GHSZ. However, previous studies have described an extensive polygonal fault system within the Kai Formation, directly below the BSR area (Berndt *et al.*, 2003; Hustoft *et al.*, 2007) and suggested it as a fluid pathway for the gas hydrate system (Bünz and Mienert, 2004). The antiform structure, as described by Hustoft et al. (2007), were suggested as vertical pathway for gaseous fluids towards the BSR area. Supporting observations are the elongated shape of high amplitude values at all three horizons within region 1 (figure 4-25) and which indicate that free gas occur at higher concentrations along this feature.

5.6 Lateral variations of reflection amplitude

Common for all three datasets, is that the dominant strata is represented as densely spaced reflections. These are, however, not represented in the same way below the BSR, where reflections are fewer, thicker and of higher amplitudes (figure 4-2 b, 4-12 and 4-20). Analysis of high-amplitude anomalies in seismic data are a common method to detect hydrocarbon accumulations, as even low gas concentrations would cause a drastic reduction in compressional wave velocity and thus a strong decrease in acoustic impedance (Domenico, 1976). As mentioned previously, several authors relate gas saturation to higher amplitudes and weak reflections to the absent of gas. Another factor that may contribute to varying amplitudes are the tuning effect, which may cause both suppression and exaggeration of reflection amplitudes (Widess, 1973). Consequently, relating varying amplitude strength to gas concentration may be somewhat misleading, especially within areas of thin-bedded strata.

Tuning effect is a phenomena that occur when a down-going wave is reflected from multiple closely spaced interfaces. If the up-going reflections overlap, the reflected seismic energy will interfere and alter the amplitude response of the true geology (Hamlyn, 2014; illustrated in figure 5-8). Interference can either be constructive or destructive, leaving reflection amplitude proportionally larger or smaller than their corresponding reflection coefficients, respectively (Miller *et al.*, 1991).

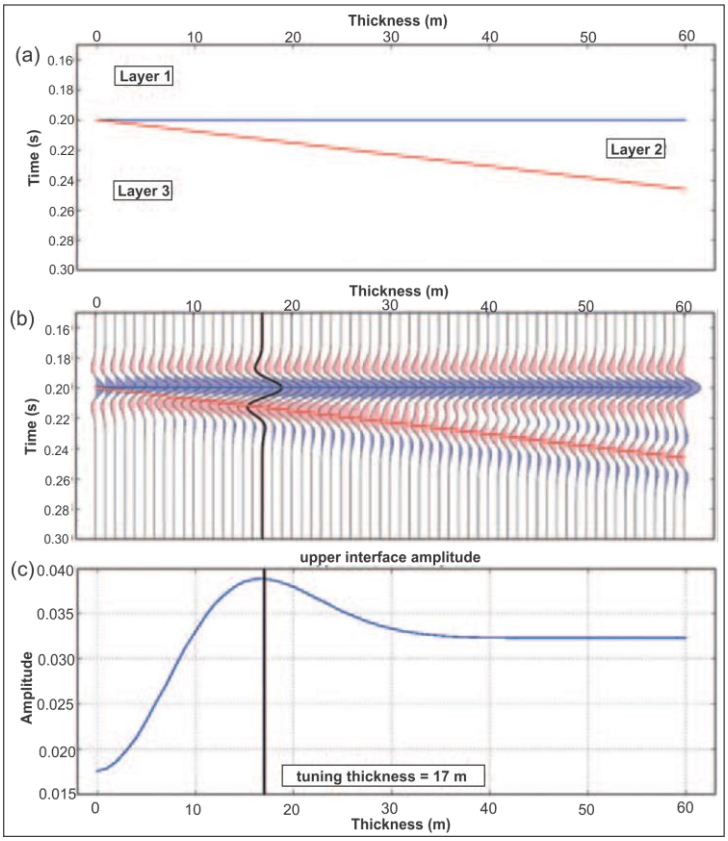

Figure 5-8: Demonstrating the tuning effect: amplitude values as a function of thickness. (a) A three-layer wedge model. (b) Zero-offset synthetic seismogram displayed in normal polarity. (c) Amplitude of the synthetic extracted along the top of layer 2. From Hamlyn (2014).

Figure 5-8 is taken from a study by Hamlyn (2014), where the constructive and destructive interference is examined by using a 30 Hz Ricker wavelet. As seen from the figure, for a thickness larger than 40 m no interference occur between the top and bottom reflections and the separate reflections appear with constant amplitude values. For thicknesses less than 40 m the wavelets starts to constructively interfere, hence producing an amplitude increase. The tuning thickness is 17 m and represents where wavelets undergo maximum interference. Below 17 m wavelets are influenced by destructive interference and result in reduced amplitude values. Figure 5-8 is only used to explain the tuning effect, and do not represent the tuning thickness for the areas within this thesis.

As hydratech.3D and Vestnesa.3D.2007 have similar shifts in frequency shifts, the tuning thickness for the FGZ at Vestnesa.3D.2007 and Vestnesa.3D.2013 is calculated by using equation 5 in figure 5-9. The frequency input to the equation is taken from their respective frequency spectrums in figure 4-4 and 4-14. An average is made of the low P-wave velocities 1250 m/s, 1400 m/s and 1600 obtained from the velocity profile in Petersen et al. (2010). The tuning thickness for Vestnesa.3D.2007 and Vestnesa.3D.2013 is ~ 7.8 m and ~6.3 m and equals ¼ of the wavelength of the seismic signal for the respective areas.

(5) $$Z = \frac{V}{2.8\, f_{max}}$$

Z = tuning thickness of a bed (m)

V = interval velocity of the target (m/s)

fmax = maximun frequency (Hz = s^{-1})

	Vestnesa.3D.2007	Vestnesa.3D.2013
fmax	65 Hz	80 Hz
V	$\frac{(1250+1400+1600)\text{m/s}}{3}$ = 1416.67 m/s	1416.67 m/s
Z	**~ 7,8 m**	**~ 6,3 m**

Figure 5-9: The tuning thickness expressed by equation (5) (from Schlumberger, 2015). Dominant frequencies for Vestnesa.3D.2007 and Vestnesa.3D.2013 are taken from their respective frequency spectrums in the result chapter. Within the FGZ, the tuning thickness for Vestnesa.3D.2007 and Vestnesa.3D.2013 are ~7.8 m and ~6.3 m, respectively.

In the result chapter, RMS-amplitude maps from selected high-amplitude reflectors revealed a conspicuously lateral amplitude pattern (figure 4-8, 4-9 and 4-25). High-amplitude regions along horizons was observed to resemble the low-amplitude regions of the underlying horizon. For Vestnesa Ridge, this could be related to the fact that gas migrate and accumulate at local highs, hereby reducing the reflection energy and consequently cause a dimming effect of amplitudes below. However, this explanation does not fit for the setting at Hydratech.3D, as the highest amplitude values occur at the

topographic low of the horizons. As these peculiar amplitude anomalies seem to fit together like pieces of a jigsaw puzzle, the observed amplitude variation are interpreted to be somewhat affected by constructive and destructive interference between gas-filled sediments of variable thickness. The observed amplitude variations of the BSR and the enhanced reflections within the FGZ are most likely a combination of varying gas saturation and tuning effect.

6. Conclusions

- High-resolution 3D seismic data reveal geophysical evidence of a prominent BSR at Vestnesa Ridge and north to the northern flank of the Storegga slide escarpment, which infer that gas hydrates are ubiquitous within these regions. Seismic characteristics of enhanced reflections terminating at the BGHSZ, zones of acoustic masking and low frequency shadows suggest the occurrence of hydrate-bearing sediments overlying significant amount of free gas within pore space of sediments.

- Pull-up and push-down effects of the BSR are frequently associated with chimney structures. Within the chimneys on the western segment of Vestnesa Ridge the BSR appearance is generally represented by a pull-up effect overlying a push-down effect in the FGZ. These are interpreted as velocity effects due to free gas trapped beneath hydrate bearing-sediments. Similar for the Hydratech-dataset, pull-up features within the pipe structures are suggested to represent the occurrence of gas hydrates and/or cemented carbonate. Although the chimneys and pipes are considered to contain high-velocity material, these structures are also suggested to be partly affected by sediment deformation due to the chimney formation.

- The broader and more crocked chimneys on the eastern segment of Vestnesa ridge show internal variations of BSR appearance. The observations of both pull-up and push-down effect at BSR level are suggested to represent internal variations of chimney material. Within the leaking chimney, the pull-up effect are attributed to significant amount of gas hydrate accumulations, whereas the pull-down effect in combination with a rough seafloor morphology are interpreted as a local pathway for the hydro-acoustically detected gas seepage. The large push-down effect within the non-leaking chimney are thought to represent significant concentrations of gas, prevented from leaking due to the self-sealing effect of gas hydrates and/or carbonate accumulations within the pockmark. Although the velocity effects are interpreted as indications of chimney material, it is most likely a combination of several reasons i.e. deformational processes, warm fluids ascending from larger depths.

- As the BSR is formed by the termination of individual gas-charged horizons, the alternating high and low amplitude values are suggested to result from varying free gas saturations trapped in beds of alternating sediment properties. As each investigated horizon show highest amplitude values against the BSR boundary, the strong amplitude values are suggested to be partly affected by interference from thin gas-charged beds that pinch out against the GHSZ.

- At Vestnesa Ridge, the largest concentration of high amplitude reflections occur directly beneath the structural high. The geometry of the FGZ suggest that gas migration and accumulation are morphological controlled. The more complex FGZ geometry at the slope setting north to the Storegga slide setting, suggest that gas migration and accumulation are restricted preferable strata and that the FGZ below the BGHSZ are largely controlled by the local geology.

- Within the FGZ, conspicuously amplitude patterns are observed along high-amplitude horizons. Especially striking are the alternating low and high amplitudes observed from the Hydratech-dataset. This makes it compelling to propose that constructive and destructive interference are affecting the peculiar amplitude anomalies, or at least a combination of varying gas saturation and tuning effect. This research is based solely on interpretation of high-resolution 3D seismic data, and should be supported by additional methods.

7. References

Andreassen, K. (2009) Marine Geophysics - Lecture Notes for GEO-3123. *University of Tromsø ,2013*.

Andreassen, K., P. E. Hart & A. Grantz (1995) Seismic studies of a bottom simulating reflection related to gas hydrate beneath the continental margin of the Beaufort Sea. *Journal of Geophysical Research: Solid Earth,* 100**,** 12659-12673.

Archer, D., B. Buffett & V. Brovkin (2009) Ocean methane hydrates as a slow tipping point in the global carbon cycle. *Proceedings of the National Academy of Sciences,* 106**,** 20596-20601.

Bahk, J.-J., I.-K. Um & M. Holland (2011) Core lithologies and their constraints on gas-hydrate occurrence in the East Sea, offshore Korea: Results from the site UBGH1-9. *Marine and Petroleum Geology,* 28**,** 1943-1952.

Bangs, N. L. B., M. J. Hornbach & C. Berndt (2011) The mechanics of intermittent methane venting at South Hydrate Ridge inferred from 4D seismic surveying. *Earth and Planetary Science Letters,* 310**,** 105-112.

Bangs, N. L. B., D. S. Sawyer & X. Golovchenko (1993) Free gas at the base of the gas hydrate zone in the vicinity of the Chile triple junction. *Geology,* 21**,** 905-908.

Barth, G. A., D. W. Scholl & J. R. Childs (2009) Bering sea velocity-amplitude anomalies: Exploring the distribution of natural gas and gas-hydrate indicators. *In: T. Collett, A. Johnson, C. Knapp, and R. Boswell, eds., Natural gas hydrates-Energy resource potential and associated geological hazards: AAPG, Memoir 89***,** 324-349.

Berndt, C., S. Bünz, T. Clayton, J. Mienert & M. Saunders (2004) Seismic character of bottom simulating reflectors: examples from the mid-Norwegian margin. *Marine and Petroleum Geology,* 21**,** 723-733.

Berndt, C., S. Bünz & J. Mienert (2003) Polygonal fault systems on the mid-Norwegian margin: a long-term source for fluid flow. *Geological Society, London, Special Publications,* 216**,** 283-290.

Bondevik, S., J. Mangerud, S. Dawson, A. Dawson & Ø. Lohne (2003) Record-breaking height for 8000-year-old tsunami in the North Atlantic. *Eos, Transactions American Geophysical Union,* 84**,** 289-293.

Bouriak, S., M. Vanneste & A. Saoutkine (2000) Inferred gas hydrates and clay diapirs near the Storegga Slide on the southern edge of the Vøring Plateau, offshore Norway. *Marine Geology,* 163**,** 125-148.

Brown, A. R. 1999. Interpretation of Three-Dimensional Seismic Data: The American Association of Petroleum Geologists Memoir, v. 42., p. 512.

Bryn, P., K. Berg, C. F. Forsberg, A. Solheim & T. J. Kvalstad (2005) Explaining the Storegga Slide. *Marine and Petroleum Geology,* 22**,** 11-19.

Bugge, T. (1983) Submarine slides on the Norwegian continental margin, with special emphasis on the Storegga area. *Continental Shelf Institute Publication.,* 110:152 pp.

Bugge, T., S. Befring, R. Belderson, T. Eidvin, E. Jansen, N. Kenyon, H. Holtedahl & H. Sejrup (1987) A giant three-stage submarine slide off Norway. *Geo-Marine Letters,* 7**,** 191-198.

Bulat, J. (2005) Some considerations on the interpretation of seabed images based on commercial 3D seismic in the Faroe-Shetland Channel. *Basin Research,* 17**,** 21-42.

Bünz, S. & J. Mienert (2004) Acoustic imaging of gas hydrate and free gas at the Storegga Slide. *Journal of Geophysical Research: Solid Earth (1978–2012),* 109.

Bünz, S., J. Mienert & C. Berndt (2003) Geological controls on the Storegga gas-hydrate system of the mid-Norwegian continental margin. *Earth and Planetary Science Letters,* 209**,** 291-307.

Bünz, S., J. Mienert, C. J. Petersen & S. Hustoft (2009) Comparative analysis of methane-seepage structures on the Vestnesa Ridge and in the Nyegga area on the Norwegian-Barents-Svalbard Margin-a model for their formation. *EGU General Assembly Conference Abstracts,* vol.11.

Bünz, S., J. Mienert, M. Vanneste & K. Andreassen (2005) Gas hydrates at the Storegga Slide: Constraints from an analysis of multicomponent, wide-angle seismic data. *GEOPHYSICS,* 70**,** B19-B34.

Bünz, S., J. Petersen, S. Hustoft & J. Mienart (2008) Environmentally-sensitive gas hydrates on the W-Svalbard margin at the gateway to the Arctic Ocean: Proceedings of the 6th international Conference on Gas hydrates, Vancouver, British Colombia, Canada, July 6-10, 6 p.

Bünz, S., S. Polyanov, S. Vadakkepuliyambatta, C. Consolaro & J. Mienert (2012) Active gas venting through hydrate-bearing sediments on the Vestnesa Ridge, offshore W-Svalbard. *Marine Geology,* 332–334**,** 189-197.

Cartwright, J., M. Huuse & A. Aplin (2007) Seal bypass systems. *AAPG Bulletin,* 91**,** 1141-1166.

Chand, S. & T. A. Minshull (2003) Seismic constraints on the effects of gas hydrate on sediment physical properties and fluid flow: a review. *Geofluids,* 3**,** 275-289.

Chapman, N. R., J. F. Gettrust, R. Walia, D. Hannay, G. D. Spence, W. T. Wood & R. D. Hyndman (2002) High-resolution, deep-towed, multichannel seismic survey of deep-sea gas hydrates off western Canada. *Geophysics,* 67**,** 1038-1047.

Collett, T. S. (2002) Energy resources potential of natural gas hydrates. *AAPG Bulletin,* Vol. 86. No. 11**,** pp. 1971-1992.

Dai, J., H. Xu, F. Snyder & N. Dutta (2004) Detection and estimation of gas hydrates using rock physics and seismic inversion: Examples from the northern deepwater Gulf of Mexico. *The Leading Edge,* 23**,** 60-66.

Davies, R. J. & J. Cartwright (2002) A fossilized Opal A to Opal C/T transformation on the northeast Atlantic margin: support for a significantly elevated Palaeogeothermal gradient during the Neogene? *Basin Research,* 14**,** 467-486.

Davies, R. J. & A. L. Clarke (2010) Methane recycling between hydrate and critically pressured stratigraphic traps, offshore Mauritania. *Geology,* 38**,** 963-966.

Davies, R. J., J. Yang, R. Hobbs & A. Li (2014) Probable patterns of gas flow and hydrate accretion at the base of the hydrate stability zone. *Geology*.

Denham, L. R. & R. E. Sheriff (1981) What is horizontal resolution? *Indonesian Petroleum Association, 10th annual convention proceedings.***,** p. 119-134.

Dewangan, P., T. Ramprasad & M. V. Ramana (2007) Finite difference modelling of scattered hydrates and its implications in gas-hydrates and its implications in gas-hydrate exploration. *CURRENT SCIENCE,* vol. 93**,** p. 1287-1290.

Dillon, W. P., J. Grow & C. K. Paull (1980) Unconventional gas hydrate seals my trap gas off southeast U.S. *Oil Gas J.,* vol. 78**,** pp. 124-130.

Domenico, S. N. (1976) Effect of brine-gas mixture on velocity in an unconsolidated sand reservoir. *Geophysics,* Vol. 41**,** 882-894.

Dvorkin, J. & A. Nur (1996) Elasticity of high-porosity sandstones: Theory for two North Sea data sets. *GEOPHYSICS,* 61**,** 1363-1370.

Ecker, C., J. Dvorkin & A. Nur (1998) Sediments with gas hydrates: Internal structure from seismic AVO. *GEOPHYSICS,* 63**,** 1659-1669.

Ecker, C. & D. Lumley. 2001. Seismic AVO analysis of methane hydrate structures. In *SEG Technical Program Expanded Abstracts 1994*, 1100-1103.

Eiken, O. & K. Hinz (1993) Contourites in the Fram Strait. *Sedimentary Geology,* 82**,** 15-32.

Engen, Ø., J. I. Faleide & T. K. Dyreng (2008) Opening of the Fram Strait gateway: A review of plate tectonic constraints. *Tectonophysics,* 450**,** 51-69.

Faleide, J., F. Tsikalas, A. Breivik, R. Mjelde, O. Ritzmann, O. Engen, J. Wilson & O. Eldholm (2008) Structure and evolution of the continental margin off Norway and the Barents Sea. *Episodes, 31(1),* 82.

Fink, C. & G. D. Spence (1999) Hydrate distribution off Vancouver Island from multi-frequency single-channel seismic reflection data. *Journal of Geophysical Research,* vol.104**,** 2909-2022.

Foucher, J.-P., H. Nouzé & P. Henry (2002) Observation and tentative interpretation of a double BSR on the Nankai slope. *Marine Geology,* 187**,** 161-175.

Geletti, R. & M. Busetti (2011) A double bottom simulating reflector in the western Ross Sea, Antarctica. *Journal of Geophysical Research: Solid Earth,* 116**,** B04101.

Grozic, J. L. H. 2010. Interplay Between Gas Hydrates and Submarine Slope Failure. In *Submarine Mass Movements and Their Consequences,* eds. D. Mosher, R. C. Shipp, L. Moscardelli, J. Chaytor, C. P. Baxter, H. Lee & R. Urgeles, 11-30. Springer Netherlands.

Haacke, R. R., G. K. Westbrook & R. D. Hyndman (2007) Gas hydrate, fluid flow and free gas: Formation of the bottom-simulating reflector. *Earth and Planetary Science Letters,* Vol. 261**,** 407-420.

Haflidason, H., R. Lien, H. P. Sejrup, C. F. Forsberg & P. Bryn (2005) The dating and morphometry of the Storegga Slide. *Marine and Petroleum Geology,* 22**,** 123-136.

Hamlyn, W. (2014) Thin beds, tuning, and AVO. *The Leading Edge,* 33**,** 1394-1396.

Hjelstuen, B. O., H. Petter Sejrup, H. Haflidason, A. Nygård, S. Ceramicola & P. Bryn (2005) Late Cenozoic glacial history and evolution of the Storegga Slide area and adjacent slide flank regions, Norwegian continental margin. *Marine and Petroleum Geology,* 22**,** 57-69.

Holbrook, W. S. 2001. Seismic Studies of the Blake Ridge: Implications for Hydrate Distribution, Methane Expulsion, and Free Gas Dynamics. In *Natural Gas Hydrates: Occurrence, Distribution, and Detection*, 235-256. American Geophysical Union.

Holbrook, W. S., A. R. Gorman, M. Hornbach, K. L. Hackwith, J. Nealon, D. Lizarralde & I. A. Pecher (2002) Seismic detection of marine methane hydrate. *The Leading Edge,* 21**,** 686-689.

Holbrook, W. S., H. Hoskins, W. T. Wood, R. A. Stephen & D. Lizarralde (1996) Methane Hydrate and Free Gas on the Blake Ridge from Vertical Seismic Profiling. *Science,* 273**,** 1840-1843.

Hornbach, M., W. Holbrook, A. Gorman, K. Hackwith, D. Lizarralde & I. Pecher (2003) Direct seismic detection of methane hydrate on the Blake Ridge. *GEOPHYSICS,* 68**,** 92-100.

Hornbach, M. J., D. M. Saffer & W. Steven Holbrook (2004) Critically pressured free-gas reservoirs below gas-hydrate provinces. *Nature,* 427**,** 142-144.

Hovland, M. (2002) On the self-sealing nature of marine seeps. *Continental Shelf Research,* 22**,** 2387-2394.

Hovland, M. & H. Svensen (2006) Submarine pingoes: Indicators of shallow gas hydrates in a pockmark at Nyegga, Norwegian Sea. *Marine Geology,* 228**,** 15-23.

Howe, J. A., T. M. Shimmield, R. E. X. Harland & N. Eyles (2008) Late Quaternary contourites and glaciomarine sedimentation in the Fram Strait. *Sedimentology,* 55**,** 179-200.

Hustoft, S., S. Bünz, J. Mienert & S. Chand (2009) Gas hydrate reservoir and active methane-venting province in sediments on <20 Ma young oceanic crust in the Fram Strait, offshore NW-Svalbard. *Earth and Planetary Science Letters,* 284**,** 12-24.

Hustoft, S., J. Mienert, S. Bünz & H. Nouzé (2007) High-resolution 3D-seismic data indicate focussed fluid migration pathways above polygonal fault systems of the mid-Norwegian margin. *Marine Geology,* 245**,** 89-106.

Hyndman, R. D. & E. E. Davis (1992) A mechanism for the formation of methane hydrate and seafloor bottom-simulating reflectors by vertical fluid expulsion. *Journal of Geophysical Research: Solid Earth,* 97**,** 7025-7041.

Hyndman, R. D. & G. D. Spence (1992) A seismic study of methane hydrate marine bottom simulating reflectors. *Journal of Geophysical Research,* 97**,** 6683-6698.

Judd, A. G. & M. Hovland. 2007. *Seabed fluid flow: The impact og geology, biology and the marine environment.* Cambridge: Cambridge University Press. 475 p.

Jung, W.-Y. & P. R. Vogt (2004) Effects of bottom water warming and sea level rise on Holocene hydrate dissociation and mass wasting along the Norwegian-Barents Continental Margin. *Journal of Geophysical Research: Solid Earth,* 109**,** B06104.

Kennett, J., K. Cannariato, I. Hendy & R. Behl (2003) Methane Hydrates in Quarternary Climate Change: The Clathrate Gun Hypothesis. *American Geophysical Union,* Vol. 54.

Kvenvolden, K. A. (1993[a]) Gas hydrates - Geological perspective and global change. *Reviews of Geophysics,* 31**,** 173-187.

Kvenvolden, K. A. (1998) A primer on the geological occurrence of gas hydrate. *Geological Society, London, Special Publications,* 137**,** 9-30.

Kvenvolden, K. A. (1999) Potential effects of gas hydrate on human welfare. *Proceedings of the National Academy of Sciences,* 96**,** 3420-3426.
Kvenvolden, K. A. (2000) Gas Hydrate and Humans. *Annals of the New York Academy of Sciences,* 912**,** 17-22.
Kvenvolden, K. A. & L. A. Barnard (1983) Gas hydrates of the Blake Outer ridge, Site 533, Deep Sea Drilling Project Leg 76: Initial reports of of the deep sea drilling project. 76**,** 353-365.
Laird, A. P. & C. K. Morley (2011) Development of gas hydrates in a deep-water anticline based on attribute analysis from three-dimensional seismic data. *Geosphere,* 7**,** 240-259.
Le, A. N., M. Huuse, J. Redfern, R. L. Gawthorpe & D. Irving (2014) Seismic characterization of a Bottom Simulating Reflection (BSR) and plumbing system of the Cameroon margin, offshore West Africa. *Marine and Petroleum Geology*.
Lee, G. H., H.-J. Kim, H.-T. Jou & H.-M. Cho (2003) Opal-A/opal-CT phase boundary inferred from bottom-simulating reflectors in the southern South Korea Plateau, East Sea (Sea of Japan). *Geophysical Research Letters,* 30**,** 2238.
Lee, J., Y. Baek, B. Ryu, M. Riedel & R. Hyndman (2005) A seismic survey to detect natural gas hydrate in the East Sea of Korea. *Marine Geophysical Researches,* 26**,** 51-59.
Lerche, I. & E. Bagirov (1998) Guide to gas hydrate stability in various geological settings. *Marine and Petroleum Geology,* 15**,** 427-437.
Locat, J. & H. J. Lee (2002) Submarine landslides: advances and challenges. *Canadian Geotechnical Journal,* 39**,** 193-212.
Løseth, H., M. Gading & L. Wensaas (2009) Hydrocarbon leakage interpreted on seismic data. *Marine and Petroleum Geology,* 26**,** 1304-1319.
MacDonald, G. (1990) Role of methane clathrates in past and future climates. *Climatic Change,* 16**,** 247-281.
MacKay, M. E., R. D. Jarrard, G. K. Westbrook & R. D. Hyndman (1994) Origin of bottonm-simulating reflectors: geophysical evidence from the cascadia accretionary prism. *Geology,* 22**,** 459-462.
Madrussani, G., G. Rossi & A. Camerlenghi (2010) Gas hydrates, free gas distribution and fault pattern on the west Svalbard continental margin. *Geophysical Journal International,* 180**,** 666-684.
Makogon, Y. F. (2010) Natural gas hydrates – A promising source of energy. *Journal of Natural Gas Science and Engineering,* 2**,** 49-59.
Maslin, M., M. Owen, R. Betts, S. Day, T. Dunkley Jones & A. Ridgwell (2010) Gas hydrates: past and future geohazard? *Philosophical Transactions of the Royal Society A: Mathematical, Physical and Engineering Sciences,* 368**,** 2369-2393.
Maslin, M., M. Owen, S. Day & D. Long (2004) Linking continental-slope failures and climate change: Testing the clathrate gun hypothesis. *Geology,* 32**,** 53-56.
McIver, R. D. (1982) Role of Naturally occurring gas hydrates in sediment transport. *AAPG Bull.,* Vol. 66, No. 6**,** p. 789-792.
Mienert, J., K. Andreassen & S. Bünz. 2003. Gas Hydrates at Storegga Slide. In *European Margin Sediment Dynamics,* eds. J. Mienert & P. Weaver, 107-110. Springer Berlin Heidelberg.
Mienert, J., J. Posewang & M. Baumann (1998) Gas hydrates along the northeastern Atlantic margin: possible hydrate-bound margin instabilities and possible release of methane. *Geological Society, London, Special Publications,* 137**,** 275-291.
Mienert, J., J. Posewang & D. Lukas. 2001. Changes in the Hydrate Stability Zone on the Norwegian Margin and their Consequence for Methane and Carbon Releases Into the Oceanosphere. In *The Northern North Atlantic,* eds. P. Schäfer, W. Ritzrau, M. Schlüter & J. Thiede, 259-280. Springer Berlin Heidelberg.
Mienert, J., M. Vanneste, S. Bünz, K. Andreassen, H. Haflidason & H. P. Sejrup (2005) Ocean warming and gas hydrate stability on the mid-Norwegian margin at the Storegga Slide. *Marine and Petroleum Geology,* 22**,** 233-244.
Milkov, A. V. (2004) Global estimates of hydrate-bound gas in marine sediments: how much is really out there? *Earth-Science Reviews,* 66**,** 183-197.

Minshull, T. A., S. C. Singh & G. K. Westbrook (1994) Seismic velocity structure at a gas hydrate reflector, offshore western Colombia, from full waveform inversion. *Journal of Geophysical Research: Solid Earth,* 99**,** 4715-4734.

Naudts, L., J. Greinert, Y. Artemov, P. Staelens, J. Poort, P. Van Rensbergen & M. De Batist (2006) Geological and morphological setting of 2778 methane seeps in the Dnepr paleo-delta, northwestern Black Sea. *Marine Geology,* 227**,** 177-199.

Nimblett, J. N., R. C. Shipp & F. Strijbos. 2005. Gas Hydrate As A Drilling Hazard: Examples From Global Deepwater Settings. Offshore Technology Conference.

Nisbet, E. G. (1990) The end of the ice age. *Canadian Journal of Earth Sciences,* 27**,** 148-157.

Nixon, M. F. & J. L. H. Grozic (2006) A simple model for submarine slope stability analysis with gas hydrates. *Norwegian Journal of Geology,* Vol. 86**,** p. 309-316.

Nouzé, H., I. Contrucci, J.-P. Foucher, B. Marsset, Y. Thomas, E. Thereau, A. Normand, É. Le Drezen, S. Didailler, J.-P. Regnault, S. Le Conte, S. Guidart, W. Lekens, S. Dean & A. Throo (2004) Premiers résultats d'une étude géophysique sur le flanc nord des glissements de Storegga (Norvège). *Comptes Rendus Geoscience,* 336**,** 1181-1189.

P-Cable. 2015. http://www.pcable.com/.

Paull, C., W. Ussler, III, W. S. Holbrook, T. Hill, R. Keaten, J. Mienert, H. Haflidason, J. Johnson, W. Winters & T. Lorenson (2008) Origin of pockmarks and chimney structures on the flanks of the Storegga Slide, offshore Norway. *Geo-Marine Letters,* 28**,** 43-51.

Paull, C. K., W. Ussle & W. S. Borowski (1994) Sources of Biogenic Methane to Form Marine Gas Hydrates In Situ Production or Upward Migration?a. *Annals of the New York Academy of Sciences,* 715**,** 392-409.

Pecher, I. A., T. A. Minshull, S. C. Singh & R. v. Huene (1996) Velocity structure of a bottom simulating reflector offshore Peru: Results from full wave form inversion. *Earth and Planetary Science Letters,* 139**,** 459-469.

Petersen, C. J., S. Bünz, S. Hustoft, J. Mienert & D. Klaeschen (2010) High-resolution P-Cable 3D seismic imaging of gas chimney structures in gas hydrated sediments of an Arctic sediment drift. *Marine and Petroleum Geology,* 27**,** 1981-1994.

Petersen, C. J., C. Papenberg & D. Klaeschen (2007) Local seismic quantification of gas hydrates and BSR characterization from multi-frequency OBS data at northern Hydrate Ridge. *Earth and Planetary Science Letters,* 255**,** 414-431.

Planke, S., C. Berndt, J. Mienert & S. Bünz (2010) P-Cable: High-Resolution 3D Seismic Acquisition Technology.

Plaza-Faverola, A., S. Bünz, J. E. Johnson, S. Chand, J. Knies, J. Mienert & P. Franek (2015) Role of tectonic stress in seepage evolution along the gas hydrate charged Vestnesa Ridge, Fram Strait. *Geophysical Research Letters***,** 2014GL062474.

Plaza-Faverola, A., S. Bünz & J. Mienert (2011) Repeated fluid expulsion through sub-seabed chimneys offshore Norway in response to glacial cycles. *Earth and Planetary Science Letters,* 305**,** 297-308.

Plaza-Faverola, A., S. Bünz & J. Mienert (2012) The free gas zone beneath gas hydrate bearing sediments and its link to fluid flow: 3D seismic imaging offshore Mid-Norway. *Marine Geology,* 291-294**,** 211-226.

Plaza-Faverola, A., G. K. Westbrook, S. Ker, R. J. K. Exley, A. Gailler, T. A. Minshull & K. Broto (2010) Evidence from three-dimensional seismic tomography for a substantial accumulation of gas hydrate in a fluid-escape chimney in the Nyegga pockmark field, offshore Norway. *Journal of Geophysical Research: Solid Earth,* 115**,** B08104.

Posewang, J. & J. Mienert (1999a) The enigma of double BSRs: indicators for changes in the hydrate stability field? *Geo-Marine Letters,* 19**,** 157-163.

Posewang, J. & J. Mienert (1999b) High-resolution seismic studies of gas hydrates west of Svalbard. *Geo-Marine Letters,* 19**,** 150-156.

Riedel, M., T. Collett & M. J. Malone (2009) Gas hydrate drilling transect across northern Cascadia margin - IODP Expedition 311. *Geological Society, London, Special Publications,* 319**,** 11-19.

Robertsson, J. D. & H. H. Nogami (1984) Complex seismic trace analysis of thin beds. *GEOPHYSICS* 49**,** 344-352.
Rokoengen, K. (1996) Upper Cenozoic stratigraphy on the mid-Norwegian continental shelf. *Oceanographic Literature Review,* 43.
Ruppel, C. & D. Noserale (2012) Gas hydrates and climate warming- Why a methane catastrophe is unlikey. *Sound Waves, USGS.,* Vol. FY 2012.
Satyavani, N., K. Sain, M. Lall & B. J. P. Kumar (2008) Seismic attribute study for gas hydrates in the Andaman Offshore India. *Marine Geophysical Researches,* 29**,** 167-175.
Schlumberger (2011) Petrel 2010 -Interpreter's Guide to Seismic Attributes.
Schlumberger (2015) Tuning effect *http://www.glossary.oilfield.slb.com/en/Terms.aspx?LookIn=term%20name&filter=tuning%20effect*.
Shakhova, N., I. Semiletov, A. Salyuk, V. Yusupov, D. Kosmach & Ö. Gustafsson (2010) Extensive Methane Venting to the Atmosphere from Sediments of the East Siberian Arctic Shelf. *Science,* 327**,** 1246-1250.
Shipley, T. H., M. H. Houston, R. T. Buffler, F. J. Shaub, K. J. McMillen, J. W. Ladd & J. L. Worzel (1979) Seismic evidence for widespread possible gas hydrate horizons on continental slopes and rises. *AAPG Bull.,* Vol. 63**,** 2204-2213.
Singh, S. C., T. A. Minshull & G. D. Spence (1993) Velocity Structure of a Gas Hydrate Reflector. *Science,* 260**,** 204-207.
Sloan, E. D. (1998) Physical/chemical properties of gas hydrates and application to world margin stability and climatic change. *Geological Society, London, Special Publications,* 137**,** 31-50.
Sloan, E. D., C. A. Koh & A. K. Sum (2010) Gas Hydrate Stability and Sampling: The Future as Related to the Phase Diagram. *Energies,* 3**,** 1991-2000.
Smith, A. J., J. Mienert, S. Bünz & J. Greinert (2014) Thermogenic methane injection via bubble transport into the upper Arctic Ocean from the hydrate-charged Vestnesa Ridge, Svalbard. *Geochemistry, Geophysics, Geosystems,* 15**,** 1945-1959.
Spence, G. D., T. A. Minshull & C. Fink (1995) Seismic studies of methane gas hydrate, offshore Vancouver Island. *Proceedings of the Ocean Drilling Program, Scientific Results,* vol. 146**,** pp. 163-174.
Sultan, N., P. Cochonat, M. Canals, A. Cattaneo, B. Dennielou, H. Haflidason, J. S. Laberg, D. Long, J. Mienert, F. Trincardi, R. Urgeles, T. O. Vorren & C. Wilson (2004a) Triggering mechanisms of slope instability processes and sediment failures on continental margins: a geotechnical approach. *Marine Geology,* 213**,** 291-321.
Sultan, N., P. Cochonat, J. P. Foucher & J. Mienert (2004b) Effect of gas hydrates melting on seafloor slope instability. *Marine Geology,* 213**,** 379-401.
Taner, M. T., F. Koehler & R. E. Sheriff (1979) Complex seismic trace analysis. *Geophysics,* 44**,** 1041-1063.
Taylor, M. H., W. P. Dillon & I. A. Pecher (2000) Trapping and migration of methane associated with the gas hydrate stability zone at the Blake Ridge Diapir: new insights from seismic data. *Marine Geology,* 164**,** 79-89.
Thiede, J. & A. M. Myhre (1996) Introduction to the North Atlantic- Arctic Gateways: Plate tectonic - paleoceanographic history and significants. *In: Proceedings on the Ocean Drilling Program, Scientific Results***,** pp. 3-33.
Thomas, Y., B. Marsset, S. Didailler, J.-P. Regnault, S. Le Conte, D. Le Roux, P. Farcy, M. Magueur, P. Viollette, J. Herveou, J.-C. Guedes, B. Jegot, G. Gascon, C. Prud'homme, H. Nouze, E. Thereau, I. Contrucci & J.-P. Foucher (2004) Sismique marine haute résolution 3D : un nouvel outil de reconnaissance à destination de la communauté scientifique. *Comptes Rendus Geoscience,* 336**,** 579-585.
Tinivella, U., F. Accaino & A. Camerlenghi (2002) Gas hydrate and free gas distribution from inversion of seismic data on the South Shetland margin (Antarctica). *Marine Geophysical Researches,* 23**,** 109-123.

Tréhu, A. M., P. E. Long, M. E. Torres, G. Bohrmann, F. R. Rack, T. S. Collett, D. S. Goldberg, A. V. Milkov, M. Riedel, P. Schultheiss, N. L. Bangs, S. R. Barr, W. S. Borowski, G. E. Claypool, M. E. Delwiche, G. R. Dickens, E. Gracia, G. Guerin, M. Holland, J. E. Johnson, Y. J. Lee, C. S. Liu, X. Su, B. Teichert, H. Tomaru, M. Vanneste, M. Watanabe & J. L. Weinberger (2004) Three-dimensional distribution of gas hydrate beneath southern Hydrate Ridge: constraints from ODP Leg 204. *Earth and Planetary Science Letters,* 222**,** 845-862.

Tucholke, B. E., G. M. Bryan & J. I. Ewing (1977) Gas-hydrate horizons detected in seismic-profiler data from the western North Atlantic. *AAPG Bulletin,* 61**,** 698-707.

Vanneste, M., M. De Batist, A. Golmshtok, A. Kremlev & W. Versteeg (2001) Multi-frequency seismic study of gas hydrate-bearing sediments in Lake Baikal, Siberia. *Marine Geology,* 172**,** 1-21.

Vanneste, M., S. Guidard & J. Mienert. 2005a. Arctic gas hydrate provinces along the western Svalbard continental margin. In *Norwegian Petroleum Society Special Publications,* eds. J. P. N. E. E. Bjørn T.G Wandås & G. Felix, 271-284. Elsevier.

Vanneste, M., S. Guidard & J. Mienert (2005b) Bottom-simulating reflections and geothermal gradients across the western Svalbard margin. *Terra Nova,* 17**,** 510-516.

Vogt, P. R., K. Crane, E. Sundvor, B. O. Hjelstuen, J. Gardner, F. Bowles & G. Cherkashev (1999) Ground-Truthing 11- to 12-kHz side-scan sonar imagery in the Norwegian–Greenland Sea: Part II: Probable diapirs on the Bear Island fan slide valley margins and the Vøring Plateau. *Geo-Marine Letters,* 19**,** 111-130.

Vogt, P. R., K. Crane, E. Sundvor, M. D. Max & S. L. Pfirman (1994) Methane-generated(?) pockmarks on young, thickly sedimented oceanic crust in the Arctic. Vestnesa ridge, Fram strait. *Journal Name: Geology; (United States); Journal Volume: 22:3***,** Medium: X; Size: Pages: 255-258.

Werner, K., R. F. Spielhagen, D. Bauch, H. C. Hass, E. Kandiano & K. Zamelczyk (2011) Atlantic Water advection to the eastern Fram Strait — Multiproxy evidence for late Holocene variability. *Palaeogeography, Palaeoclimatology, Palaeoecology,* 308**,** 264-276.

Westbrook, G. K., S. Chand, G. Rossi, C. Long, S. Bünz, A. Camer lenghi, J. M. Carcione, S. Dean, J.-P. Foucher, E. Flueh, D. Gei, R. R. Haacke, G. Madrussani, J. Mienert, T. A. Minshull, H. Nouzé, S. Peacock, T. J. Reston, M. Vanneste & M. Zillmer (2008a) Estimation of gas hydrate concentration from multi-component seismic data at sites on the continental margins of NW Svalbard and the Storegga region of Norway. *Marine and Petroleum Geology,* Vol. 25**,** 744-758.

Westbrook, G. K., T. A. Minshull, H. Nouzé, R. Exley, A. Gailler, T. Jose, S. Ker & A. Plaza-Faverola (2008b) High-resolution 3D seismic investigations of hydrate-bearing fluid-escape chimneys in the Nyegga region of the Vøring plateau, Norway. *In: Proceedings of the 6th International Conference on Gas Hydrates (ICGH 2008) 6-8 July, Vancouver, British Columbia, Canada***,** pp. 12.

Westbrook, G. K., K. E. Thatcher, E. J. Rohling, A. M. Piotrowski, H. Pälike, A. H. Osborne, E. G. Nisbet, T. A. Minshull, M. Lanoisellé, R. H. James, V. Hühnerbach, D. Green, R. E. Fisher, A. J. Crocker, A. Chabert, C. Bolton, A. Beszczynska-Möller, C. Berndt & A. Aquilina (2009) Escape of methane gas from the seabed along the West Spitsbergen continental margin. *Geophysical Research Letters,* 36**,** L15608.

Widess, M. B. (1973) HOW THIN IS A THIN BED? *GEOPHYSICS,* 38**,** 1176-1180.

Wood, W. T., J. F. Gettrust, N. R. Chapman, G. D. Spence & R. D. Hyndman (2002) Decreased stability of methane hydrates in marine sediments owing to phase-boundary roughness. *Nature,* 420**,** p. 656-660.

Wood, W. T. & C. Ruppel (2000) Seismic and thermal investigations of the Blake Ridge gas hydrate area: a synthesis. *In: Paull, C.K. et al., (Eds.), Proceedings of the Ocean Drilling Program, Scientific Results,* vol.164**,** pp.253-264.

Yakushev, V. S. & T. S. Collett. 1992. Gas Hydrates In Arctic Regions: Risk To Drilling And Production. International Society of Offshore and Polar Engineers.

Yamano, M., S. Uyeda, Y. Aoki & T. H. Shipley (1982) Estimates of heat flow derived from gas hydrates. *Geology,* Vol.10**,** 339-343.

Yuan, T., K. S. Nahar, R. Chand, R. D. Hyndman, G. D. Spence & N. R. Chapman (1998) Marine gas hydrates: Seismic observations of bottom-simulating reflectors off the West Coast of Canada and the East Coast of India. *Geohorizons,* Vol.3.